

Charles University

Faculty of Science

Study program: Organic Chemistry



Ing. Erik Andris

Investigation of Non-Heme Iron-Oxo Intermediates in the Gas Phase

Výzkum oxo intermediátů železa nehemového typu v plynné fázi

Type of thesis

Doctoral thesis

Supervisor: Prof. Mgr. Jana Roithová, Ph. D.

Prague, 2018

Jn 19, 22

Prohlášení

Prohlašuji, že jsem tuto práci zpracoval samostatně a že jsem řádně citoval všechny použité informační prameny. Tato práce ani její podstatná část nebyla předložena k získání jiného nebo stejného akademického titulu. Při zpracování této práce byly použity následující publikace:

Kapitola 3:

- (1) Andris, E.; Jašík, J.; Gómez, L.; Costas, M.; Roithová, J. Spectroscopic Characterization and Reactivity of Triplet and Quintet Iron(IV) Oxo Complexes in the Gas Phase. *Angew. Chem. Int. Ed.* **2016**, *55*, 3637–3641.
- (2) Andris, E.; Navrátil, R.; Jašík, J.; Terencio, T.; Srnec, M.; Costas, M.; Roithová, J. Chasing the Evasive Fe=O Stretch and the Spin State of the Iron(IV)–Oxo Complexes by Photodissociation Spectroscopy. *J. Am. Chem. Soc.* **2017**, *139*, 2757–2765.

Kapitola 4:

- (3) Andris, E.; Navrátil, R.; Jašík, J.; Puri, M.; Costas, M.; Que, L., Jr.; Roithová, J. Trapping Iron(III)–Oxo Species at the Boundary of the “Oxo Wall”: Insights into the Nature of the Fe(III)–O Bond. *J. Am. Chem. Soc.* **2018**, *140*, 14391–14400.

Mé podíly příspěvků k těmto publikacím byly následovné:

- (1) V první publikaci jsem měřil IRPD spektra (30 %), zpracoval a vyhodnocoval data (50 %), dělal DFT výpočty (80 %), měřil reaktivitu v plynné fázi (100 %) a podílel se na psaní článku (20 %) a SI (100 %).
- (2) Ve druhé publikaci jsem měřil IRPD spektra (50 %), zpracoval a vyhodnocoval data (80 %), dělal DFT výpočty (90 %), měřil reaktivitu v plynné fázi (100 %) a podílel se na psaní článku (30 %) a SI (50 %).
- (3) Ve třetí publikaci jsem měřil IRPD a visPD spektra (40 %), zpracoval a vyhodnocoval data (50 %), dělal DFT výpočty (100 %), měřil reaktivitu v plynné fázi (100 %) a podílel se na psaní článku (30 %) a SI (50 %).

V Praze dne _____

Ing. Erik Andris

Potvrzuji správnost výše uvedených podílů příspěvků k publikacím.

V Nijmegen dne _____

Prof. Mgr. Jana Roithová, Ph. D.

Acknowledgement

This work has been made possible by the cooperation of many people. First I would like to thank my supervisor Jana Roithová for her guidance throughout my Ph. D. studies. Next I would like to thank all my coworkers, namely Rafael Navrátil, for fruitful collaboration. Third, I would like to thank Danuše Andrisová for her support of my scientific undertakings. My gratitude goes also to Marcel Lubben *et al.* (Ref. 46) for inventing the N4Py ligand.

Finally, I would like to thank Danuše Andrisová, Marek Bot, Mariarosa Anania and Jan Zelenka for their help with proof-reading.

The results contained in this thesis were produced in projects funded by the European Research Council (ERC StG No. 258299, ERC CoG No. 682275), the Czech Ministry of Education, Youth and Sports (LTAUSA17026), and the COST action ECOSTBio.

Abstract

I used helium-tagging infrared photodissociation spectroscopy of ions in the IR (IRPD) and vis (visPD) range in conjunction with gas-phase reactivity studies to study biomimetic terminal iron-oxo complexes. In first part of the work, I measured IRPD spectra of iron(IV)-oxo complexes of TMC, N4Py and PyTACN amine ligands in different charge states. Results show that the gas-phase Fe=O stretching frequencies are, on average, blue-shifted by 9 cm^{-1} with respect to the condensed phase. I prepared stereoisomers of $[(\text{PyTACN})\text{Fe}^{\text{IV}}(\text{O})(\text{X})]^+$ complexes ($\text{X} = \text{CF}_3\text{COO}, \text{NO}_3$) that were in quintet and triplet state using nitrate cleavage method and showed that the Fe=O frequency of these iron(IV)-oxo complexes is not affected by the spin state. Gas-phase reactivity shows that dicationic complexes react with 1,4-cyclohexadiene by hydride transfer and monocationic complexes engage in hydrogen atom transfer (HAT) from the methylene group and oxygen atom transfer to the C=C bond. Variation of the ligand *trans* to the Fe=O unit has the greatest influence on reactivity, whereas the spin state has a modest effect. In the second part of the work, I prepared and studied gas-phase iron(III)-oxo complexes with N4Py, TPA, TQA and TMC ligands. IRPD and visPD spectra in conjunction with DFT calculations allowed me to assign the spin state of the former two complexes as quartet and the latter two complexes as sextet. Whereas the Fe=O stretching frequencies in quartet complexes are essentially the same as in iron(IV)-oxo complexes, the frequencies in sextet complexes are red-shifted by $\sim 70\text{ cm}^{-1}$. Moreover, I showed that coordination of water molecule to the quartet complexes triggers a spin flip to sextet. Finally, I showed that iron(III)-oxo complexes do not engage in HAT with 1,4-cyclohexadiene, but they react in a net HAT with ethanethiol via proton transfer – electron transfer mechanism. In conclusion, this thesis demonstrates the applicability of gas-phase spectroscopy of ions to bioinorganic chemistry and sets the stage for the future work in this field.

Abstrakt v slovenskom jazyku

V tejto práci som študoval terminálne oxo komplexy železa za pomoci merania reaktivity v plynnej fáze a fotodisociačnej spektroskopie iónov s využitím héliového značenia v IČ (IRPD) a vis (visPD) oblasti. V prvej časti som zmeral IRPD spektrá oxoželezičitých komplexov s amínovými ligandmi TMC, N4Py a PyTACN v rôznych nábojových stavoch. Zistil som, že vlnočty valenčných Fe=O vibrácii sú, voči vlnočtom v roztoku, modro posunuté priemerne o 9 cm^{-1} . Taktiež som metódou štiepenia nitrátu pripravil stereoizoméry komplexov $[(\text{PyTACN})\text{Fe}^{\text{IV}}(\text{O})(\text{X})]^+$, kde X je CF_3COO alebo NO_3 , ktoré sa líšili spinovým stavom. Pozoroval som, že vlnočet Fe=O vibrácie nezávisí na spinovom stave komplexu. Výsledky merania reaktivity v plynnej fáze ukázali, že zatiaľ, čo dvakrát nabité komplexy abstrahujú z 1,4-cyklohexadiénu hydrid, raz nabité priamo abstrahujú vodík a prenášajú na alkén kyslík za tvorby epoxidu. Najväčší vplyv na reaktivitu mala zmena ligandu v *trans* polohe voči Fe=O skupine; spinový stav hral menšiu rolu. V druhej časti som pripravil a študoval spektrá oxoželezitých komplexov s ligandmi N4Py, TPA, TQA a TMC. Z IRPD a visPD spektier týchto komplexov som za pomoci DFT výpočtov zistil, že zatiaľ, čo prvé dva majú ako spinový stav kvartet, posledné dva sú sextety. Vlnočet valenčnej Fe=O vibrácie kvartetových komplexov zodpovedá vlnočtu oxoželezičitých komplexov, v prípade sextetových komplexov je tento červeno posunutý o zhruba 70 cm^{-1} . Ďalej som ukázal, že koordinácia vody na kvartetové komplexy vedie k zmene spinu na sextet. Nakoniec som skúmal reaktivitu oxoželezitých komplexov a ukázal som, že hoci neabstrahujú vodík z 1,4-cyklohexadiénu, s etántiolom reagujú procesom abstrakcie vodíka, ktorá prebieha mechanizmom prenosu protónu a následného prenosu elektrónu. Výsledkom tejto práce je, že som ukázal potenciál spektroskopie iónov v plynnej fáze pri riešení problémov bioanorganickej chémie a pripravil pôdu pre štúdium budúcich problémov v tejto oblasti.

Abstrakt v českém jazyce

V této práci jsem studoval terminální oxo komplexy železa za pomoci měření reaktivity v plynné fázi a fotodisociační spektroskopie iontů s využitím héliového značení v IČ (IRPD) a vis (visPD) oblasti. V první části jsem změřil IRPD spektra oxoželezičitých komplexů s aminovými ligandy TMC, N4Py a PyTACN v různých nábojových stavech. Zjistil jsem, že vlnočty valenčních Fe=O vibrací jsou oproti vlnočtům v roztoku posunuty modře průměrně o 9 cm^{-1} . Taktéž jsem metodou štěpení nitrátu připravil stereoizomery komplexů $[(\text{PyTACN})\text{Fe}^{\text{IV}}(\text{O})(\text{X})]^+$, kde X je CF_3COO anebo NO_3 , které se lišily spinovým stavem. Pozoroval jsem, že vlnočty Fe=O vibrace nezávisí na spinovém stavu komplexu. Výsledky měření reaktivity v plynné fázi ukázaly, že zatímco dvakrát nabité komplexy abstrahují z 1,4-cyklohexadienu hydrid, jednou nabité komplexy přímo abstrahují vodík a přenášejí na alken kyslík za tvorby epoxidu. Největší vliv na reaktivitu měla změna ligandu v *trans* poloze vůči Fe=O skupině; spinový stav hrál menší roli. Ve druhé části jsem připravil a studoval spektra oxoželezitých komplexů s ligandy N4Py, TPA, TQA a TMC. Z IRPD a visPD spekter těchto komplexů jsem za pomoci DFT výpočtů zjistil, že zatímco první dva mají jako spinový stav kvartet, poslední dva jsou sextety. Vlnočty valenční Fe=O vibrace kvartetových komplexů odpovídá vlnočtu oxoželezičitých komplexů, v případě sextetových komplexů je tento rudě posunutý o zhruba 70 cm^{-1} . Dále jsem ukázal, že koordinace vody na kvartetové komplexy vede ke změně spinu na sextet. Nakonec jsem zkoumal reaktivitu oxoželezitých komplexů a ukázal jsem, že ačkoli neabstrahují vodík z 1,4-cyklohexadienu, s etanthiolem reagují procesem abstrakce vodíku, který probíhá mechanismem přenosu protonu a následného přenosu elektronu. Výsledkem této práce je, že jsem ukázal potenciál spektroskopie iontů v plynné fázi při řešení problémů bioanorganické chemie a připravil půdu pro studium budoucích problémů v této oblasti.

List of Abbreviations and Non-Standard Units

| | |
|------------------------------------|---|
| ACN | acetonitrile |
| BDFE | bond dissociation free energy |
| bpg | <i>N,N</i> -bis(2-pyridinylmethyl)glycinato anion |
| CASPT2 | complete active space second-order perturbation theory |
| CASSCF | complete active space self-consistent field |
| cyclam-ac | 1,4,8,11-tetraazacyclotetradecane-1-acetate |
| DAT | deuterium atom transfer |
| DESI | desorption electrospray ionization |
| DFT | density functional theory |
| DKH2 | second-order Douglas-Kroll-Hess Hamiltonian |
| ESI | electrospray ionization |
| ET-PT | electron transfer-proton transfer (mechanism) |
| EXAFS | extended X-ray absorption fine structure |
| FT-ICR | Fourier-transform ion cyclotron resonance |
| FWHM | full width at half maximum |
| H3buea | tris[(<i>N'</i> -tertbutylureaylato)- <i>N</i> -ethyl]aminato trianion |
| HAT | hydrogen atom transfer |
| HRMS | high-resolution mass spectrometry |
| IRPD | infrared photodissociation spectroscopy |
| KIE | kinetic isotope effect |
| LNHC | 3,9,14,20-tetraaza-1,6,12,17-tetraazoniapentacyclohexacosane-1(23),4,6(26),10,12(25),15,17(24),21-octaene |
| N4Py | 1,1-di(pyridin-2-yl)- <i>N,N</i> -bis(pyridin-2-ylmethyl)methanamine |
| N(afa ^{Cy}) ₃ | tris((2-((cyclohexylamino)methylene)-2H-pyrrol-5-yl)-methyl)amine |
| NRVS | nuclear resonance vibrational spectroscopy |
| OAT | oxygen atom transfer |
| OPA | optical parametric amplifier |
| OPO | optical parametric oscillator |
| PCET | proton-coupled electron transfer |
| PhIO | iodosobenzene |
| psi | pounds per square inch, (≈ 0.0068 bar), measured relative to atmospheric pressure |
| pyN4 | 2,6-bis(1,1-di(aminomethyl)ethyl)pyridine |
| PyTACN | 1-[2'-(pyridyl)methyl]-4,7-dimethyl-1,4,7-triazacyclononane |
| TDAE | tetrakis(dimethylamino)ethylene |
| TMC | 1,4,8,11-tetramethyl-1,4,8,11-tetraazacyclotetradecane |
| Torr | (¹⁰¹³²⁵ / ₇₆₀) Pa, ≈ 133 Pa |
| TPA | tris(2-pyridylmethyl)amine |
| TPFPP | <i>meso</i> -tetrakis(pentafluorophenyl)porphinato dianion |
| TQA | tris(2-quinolylmethyl)amine |

visPD

visible photodissociation spectroscopy

Table of Contents

| | |
|--|------|
| Prohlášení (Declaration) | i |
| Acknowledgement | ii |
| Abstract | iii |
| Abstrakt v slovenskom jazyku | iv |
| Abstrakt v českém jazyce | v |
| List of Abbreviations and Non-Standard Units | vi |
| Table of Contents | viii |
| CHAPTER 1. Introduction | 1 |
| 1.1. Iron Enzymes that Catalyze Oxidation Reactions | 1 |
| 1.2. Non-Heme Iron-Oxo Model Complexes | 4 |
| 1.3. Mass-Spectrometric Studies of Reactive Iron-Oxo Species | 7 |
| 1.4. Binding in the Metal-Oxo Complexes and the Oxo Wall. | 10 |
| Aims of the Work | 13 |
| CHAPTER 2. Materials and Methods | 14 |
| 2.1. Materials | 14 |
| 2.2. Electrospray Ionization Mass Spectrometry | 15 |
| 2.3. Preparation of Solutions Containing the Investigated Ions | 16 |
| 2.4. Ion-Molecule Reactions | 25 |
| 2.5. Infrared and Visible Ion Spectroscopy | 30 |
| 2.6. Theoretical Calculations | 36 |
| CHAPTER 3. Iron(IV)-Oxo Complexes in the Gas Phase | 38 |
| 3.1. Introduction | 38 |
| 3.2. Fe=O Stretching Frequencies | 38 |
| 3.3. Isomeric PyTACN Complexes | 53 |
| 3.4. Gas-Phase Reactivity | 67 |
| 3.5. Conclusions | 75 |
| CHAPTER 4. Iron(III)-Oxo Complexes in the Gas Phase | 77 |
| 4.1. Introduction | 77 |
| 4.2. IR and Vis Spectra of Iron(III)-Oxo Complexes | 79 |
| 4.3. Effect of the Hydrogen Bonding | 87 |
| 4.4. Gas-Phase Reactivity | 92 |
| 4.5. Correlation of the Fe–O Stretching Frequencies and Bond Lengths | 96 |
| 4.6. Conclusions | 98 |
| CHAPTER 5. Summary | 99 |
| References | 101 |

CHAPTER 1. Introduction

The appearance of the oxygen in the atmosphere, the Great Oxygenation Event,^{1,2} marked one of the major changes in life on Earth. Oxygen can be used as a very efficient electron sink in both respiration and other oxidation reactions. However, despite its biradical nature, it is not a kinetically competent oxidant.³ Therefore, it needs to be activated to engage in these reactions.

1.1. Iron Enzymes that Catalyze Oxidation Reactions

Out of all elements, Nature has chosen iron to harness the oxidative power of oxygen. In part, it can unleash the spin-forbidden reactivity of oxygen⁵ by enabling spin flips – a hallmark of Two State Reactivity.⁶ In the breathing process, the complicated step of controlled oxygen activation and the cleavage of O=O bond is mediated by the Cytochrome c oxidase^{7,8} - an iron and copper containing enzyme.

Oxygen is also used extensively as an oxidizing agent in the metabolism of xenobiotics, the best known example being the Cytochrome P450 enzyme family.^{9,10} Enzymes from this family belong to heme enzymes, i.e. they contain an iron atom bound to a porphyrin, and their distinctive feature is the axial cysteine ligand.¹¹ The name P450 comes from the absorption maximum in their reduced state with a bound CO molecule.¹² This family of enzymes is responsible for over 95 % of all reported enzymatic redox reactions.¹³ The reactions catalyzed by these enzymes include oxidation of aliphatic C–H bonds, epoxidations, oxidation of heteroatoms (N,S,P,I) and heteroatom dealkylations.⁹

The oxidations mediated by P450s begin by formation of the active iron(IV)-oxo radical cation intermediate (thus formally iron(V)), “compound I” (Figure 1).¹⁴ Its formation involves reversible binding of oxygen to the reduced form of the enzyme. Following one-electron reduction, the O=O bond can be cleaved to form hydroperoxo intermediate “compound 0” (see Figure 1) that eliminates water to finally yield the “compound I”.¹⁰ The “compound I” can then react with a substrate. A prominent example — the activation of an alkane substrate by “compound I” — is shown in Figure 1. The iron(IV)-oxo group can abstract hydrogen in a HAT reaction, yielding the iron(IV)-hydroxo complex. The conservation of the oxidation state in the HAT reaction is possible, because the added electron reduces the porphyrin radical cation. The reaction with the alkane then immediately

continues and alkyl radical can bind the OH radical in a rebound mechanism introduced by Groves.¹⁵

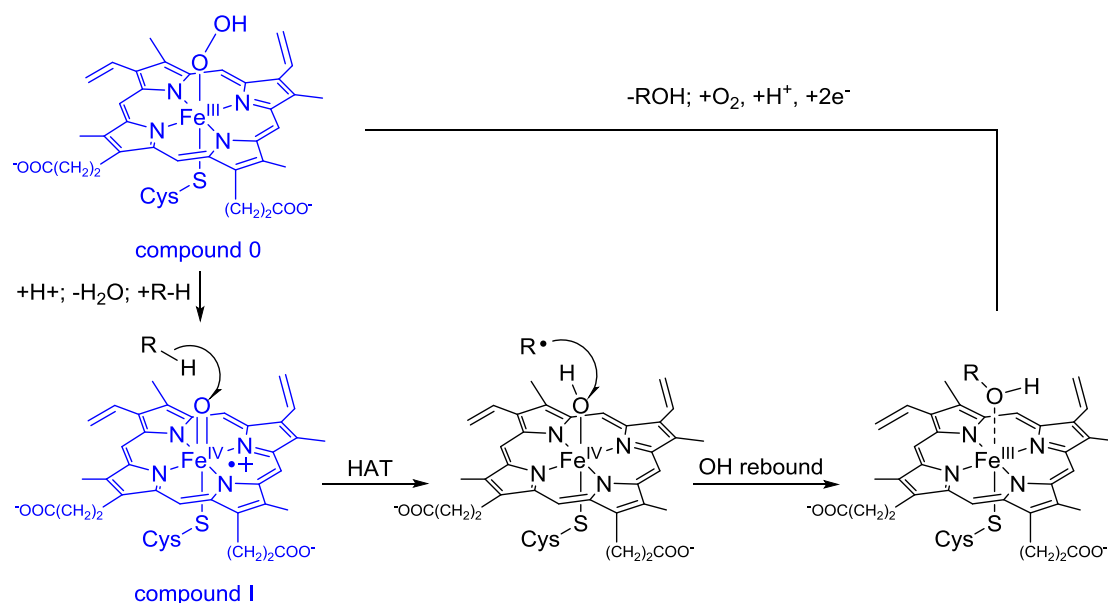


Figure 1. Rebound mechanism in oxidation of substrates by P450.¹⁶

Similar iron(IV)-oxo intermediates play role in reactions catalyzed by non-heme iron enzymes,^{17 – 19} which also serve important biological functions (Figure 2). The first characterized iron(IV)-oxo intermediate is from 2003, when the group of Bollinger and Krebs managed to observe the reactive iron(IV)-oxo intermediate for taurine dioxygenase (TauD).^{20–22} This enzyme belongs to the class of α -ketoglutarate dependent dioxygenases, which hydroxylate their substrates with O_2 as the terminal oxidant. Other examples of enzymes from this group include phenylalanine prolyl hydroxylase that forms 4-hydroxyproline, a major component of collagen²³ (the scurvy is the direct result of dysfunction of this enzyme, which also has ascorbate as a cofactor) and AlkB enzyme, which reverses the alkylation damage to the DNA.²⁴ Because O_2 , when reduced to water, is a four electron oxidant and a hydroxylation reaction requires removal of only two electrons, the α -ketoglutarate serves as a source for the two remaining electrons. These two electrons can be also supplied by other cofactor. For example phenylalanine hydroxylase, which synthesizes tyrosine in mammals, (deficiency in this enzyme causes phenylketonuria) uses tetrahydrobiopterin.²⁵ The common binding motive in α -ketoglutarate and biopterin-dependent oxygenases is the binding of iron to the facial triad of two imidazole units (from histidine) and one carboxylate.¹⁷

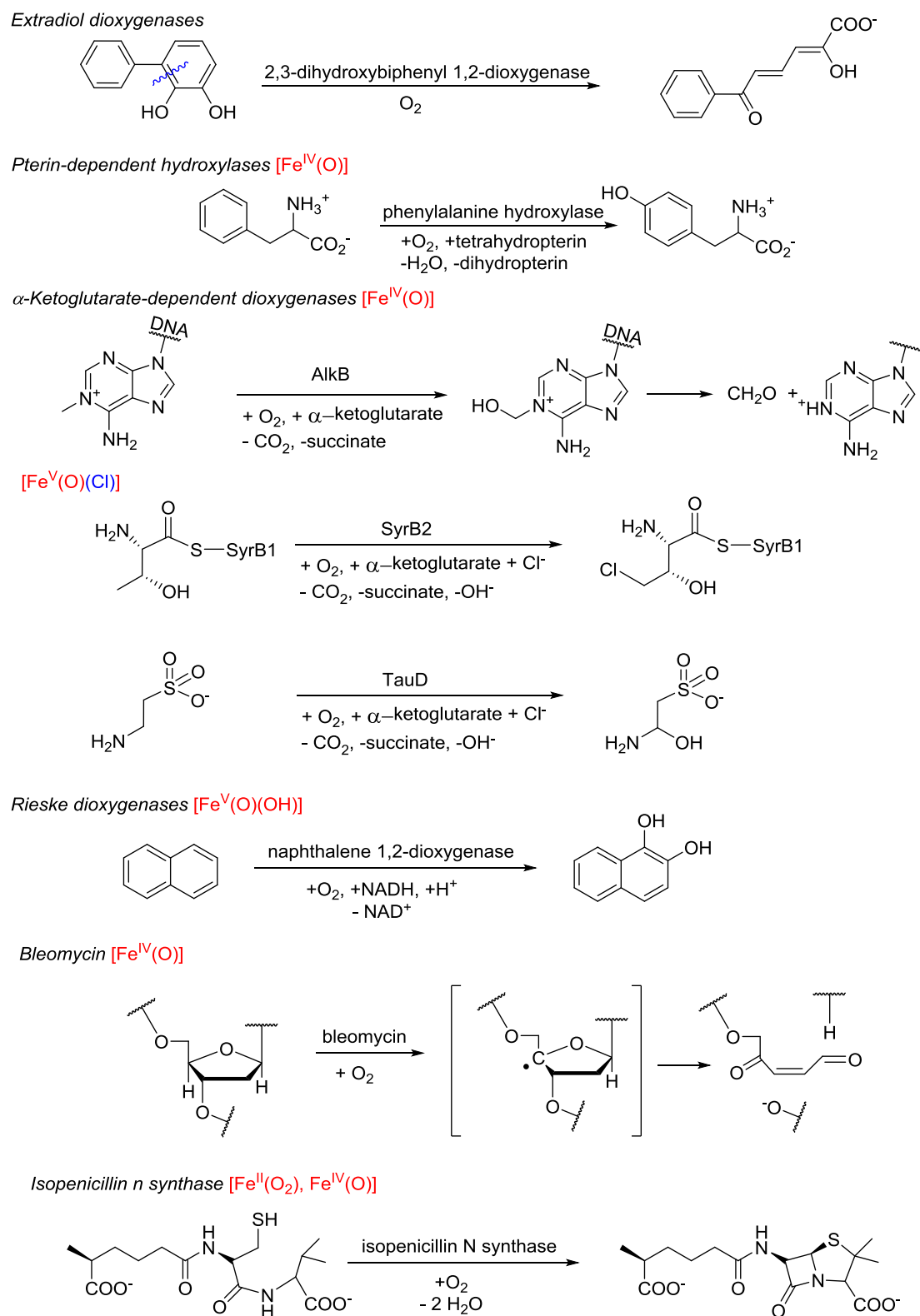


Figure 2. Selected groups of oxygen-activating non-heme iron enzymes. Adapted with permission from Ref. 18. Copyright 2013 American Chemical Society. Additional reactions were taken from the following references: alkB,²⁴ SyrB2,³⁴ TauD,²⁰ naphthalene 1,2-dioxygenase,^{26,27} bleomycin.^{28,29}

The assignment of the intermediate as iron(IV)-oxo species was done using various techniques. Taking the TauD as an example, the intermediates were first monitored by UV/vis spectroscopy. Bollinger and Krebs were initially able to perform Mössbauer spectroscopy and EPR spectroscopy of the activated enzyme and could narrow down the possibilities to iron(III)-superoxo, iron(IV)-peroxo and iron(IV)-oxo species.²⁰ They were also able to assign the electronic ground state of this form as a quintet.²⁰ The evidence of the Fe=O moiety came from the resonance Raman study by Proshlyakov *et al.*³⁰ Bollinger and Krebs later performed EXAFS to confirm the identity of this intermediate and found a short iron-oxygen distance of 1.62 Å.³¹ Another useful technique to assign the coordination sphere of iron complexes is nuclear resonance vibrational spectroscopy (NRVS),^{32, 33} which measures vibrationally-perturbed ⁵⁷Fe nuclear transitions, and thus enables to observe ⁵⁷Fe vibration modes even in complex samples. Using this technique, Wong *et al.* proved the binding of chlorine into iron halogenase enzyme SyrB2.³⁴

Even though some success has been achieved with obtaining the direct evidence of the active center structure in heme enzymes with X-ray³⁵ and neutron diffraction,^{36,37} direct evidence for most of the intermediates is likely not going to be available anytime soon. The interpretation of the experimental data has relied and will rely on the comparison with the benchmark data of comprehensively characterized model complexes.³⁸⁻⁴⁰

1.2. Non-Heme Iron-Oxo Model Complexes

Inspired by the iron enzymes and in need of the benchmark data, the first preparation of terminal iron-oxo complex was reported in 2000 by Borovik group.⁴¹ This trigonal iron(III)-oxo complex, [(H₃buea)Fe^{III}(O)]²⁻ (Figure 3a, left), stabilizes the oxo unit with the extensive hydrogen bonding in the second coordination sphere and has a sextet spin state.⁴² Interestingly, it took another fourteen years before Fout group managed to report the second and so far the only other characterized iron(III)-oxo complex [(N(afa^{Cy})₃)Fe^{III}(O)]⁺ (Figure 3a, right),⁴³ again stabilized by the hydrogen bonding and in the sextet state.

Meanwhile, the iron(IV)-oxo chemistry research has been much more fruitful. In 2000, Grapperhaus *et al.* (Wieghardt group) managed to oxidize [(cyclam-ac)Fe^{III}(OTf)]²⁺ with ozone at -80°C and obtain evidence of iron(IV)-oxo species from the analysis of Mössbauer data.⁴⁴ The definitive confirmation of the existence of such species came in 2001, when Rohde *et al.* managed to prepare iron(IV)-oxo complex [(TMC)Fe^{IV}(O)(ACN)]²⁺ (Figure 3b, left) by oxidation of [(TMC)Fe^{II}(OTf)₂] by iodosobenzene and obtain its X-ray

structure.⁴⁵ Another big development was the characterization of complex $[(\text{N4Py})\text{Fe}^{\text{IV}}(\text{O})]^{2+}$ (Figure 3b, center; see also Ref. 46 for the related iron(III)-hydroperoxo complex), which was one of the first to oxidize cyclohexane.^{47,48} Moreover, it is exceptionally stable even at room temperature. However, these early examples failed to model the spin state of the enzyme intermediates, as they were all in triplet state, with the exception of $[(\text{H}_2\text{O})_5\text{Fe}^{\text{IV}}(\text{O})]^{2+}$ (Figure 3c, left), an intermediate observed upon oxidation of Fe^{2+} with ozone in water at pH 1 characterized by Pestovsky *et al.* in 2005.⁴⁹ Achieving the synthesis of a high-spin model complex therefore became an important task in the field, even more so because DFT calculations predicted that the quintet state complexes should be exceptionally reactive.^{50–53}

In 2005, England *et al.* reported, for the first time quintet iron(IV)-oxo complex $[(\text{TMG}_3\text{tren})\text{Fe}^{\text{IV}}(\text{O})]^{2+}$ (Figure 3c, center) that was sufficiently stable to be thoroughly characterized,⁵⁴ the quintet ground spin state has been achieved by the trigonal (as opposed to tetragonal) symmetry of iron coordination environment. The complex was, however, not exceptionally reactive. First quintet state iron(IV)-oxo complex in tetragonal environment $[(\text{TQA})\text{Fe}^{\text{IV}}(\text{O})(\text{ACN})]^{2+}$ (Figure 3c, right; interestingly, related $[(\text{TPA})\text{Fe}^{\text{IV}}(\text{O})(\text{ACN})]^+$ complex⁵⁵ with pyridines instead of quinolines has a triplet spin state) was reported in 2015 by Biswas *et al.*,⁵⁶ and this complex has been shown to be very reactive in C–H oxidations and C=C epoxidation reactions. To put it into perspective, however, it has about the same reactivity as the most reactive triplet iron(IV)-oxo complex, $[(\text{Me}_3\text{NTB})\text{Fe}^{\text{IV}}(\text{O})(\text{ACN}?)^+]$ (Figure 3b, right; the question mark marks the uncertain presence of the ACN ligand).⁵⁷ Nevertheless, the influence of the spin state on reactivity of iron-oxo complexes has stayed unclear, because the changes in reactivity can be also attributed to differences in the coordination sphere and not only to the spin state difference.

Identification of the reactive iron intermediates in these studies mostly relied on UV/vis absorption spectroscopy. Once the intermediates were identified, Mössbauer spectroscopy could be used to assign the oxidation state and other electronic parameters. EPR spectroscopy was also useful, but since most iron(IV)-oxo complexes have $S = 1$ spin, their EPR spectra are silent. Magnetic circular dichroism can also reveal additional information about the electronic structure.^{58,59} The geometry around the iron center was assessed from X-ray diffraction; where this was not possible EXAFS was used instead.⁴⁵ The most convincing evidence for the iron-oxo motif was usually supplied by resonance Raman spectroscopy,^{65–67} which uses the resonance enhancement of Raman lines and relies on the presence of intense electronic absorption features.⁶⁰ However, this has not been always possible and some

complexes could not be characterized in this way.⁶¹⁻⁶³ Finally, I also have to mention the use of ⁵⁷Fe NRVs spectroscopy,⁶⁴ which is sensitive to Fe=O vibrational mode, but is technically difficult, because it requires the use of synchrotron light source and ⁵⁷Fe-enriched samples. Most of these techniques, however, require accumulation of the studied species in relatively pure form, i.e. they must be a significant fraction of the present iron species. Therefore, some species may remain unnoticed.

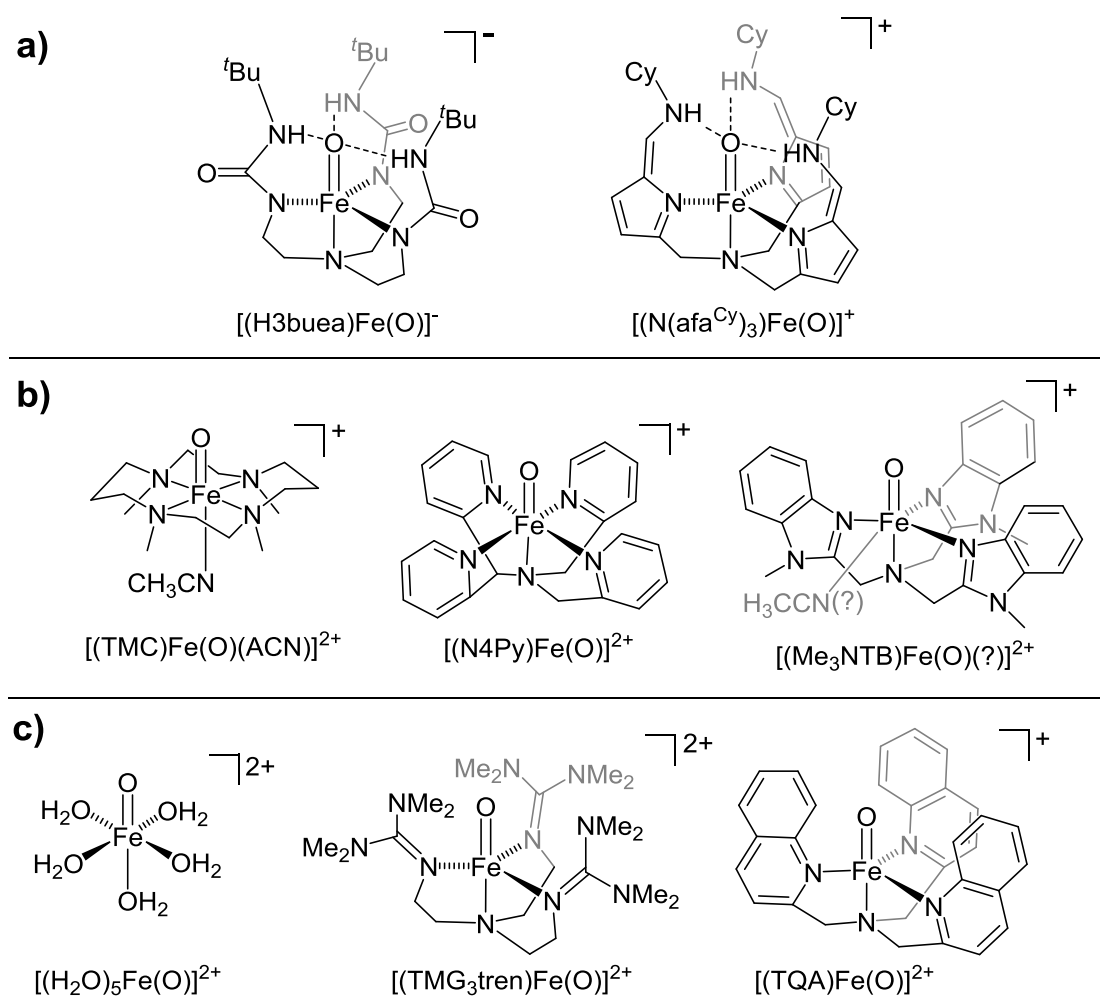


Figure 3. (a) Iron(III)-oxo complexes, (b) selected iron(IV)-oxo complexes in the triplet spin state and (c) selected iron(IV)-oxo complexes in the quintet spin state.

So far, more than 80 non-heme iron-oxo complexes have been reported in the literature, which has been covered by several excellent reviews, where some focus mostly on terminal iron-oxo⁶⁵⁻⁶⁷ and some focus on the broader field of metal-oxygen species.⁶⁸ Perspectives from the two main groups synthesizing these complexes: Nam⁶⁹⁻⁷¹ and Que,⁷² are also available.

Parallel to the development of model complexes, some groups also took advantage of the iron complexes in catalytic oxidations.^{73,74} Notably, Chen and White reported [(*S,S*-pdp)Fe^{II}(ACN)₂]²⁺ as effective catalyst for the oxidation of inert C–H bonds with H₂O₂,⁷⁵ and used the system extensively on many diverse substrates.^{76,77} Other groups used it to carry out epoxidations and proposed that these reaction proceed through iron(V) intermediates.^{78,79} One of the main techniques used to obtain information about short lived intermediates present in low concentration is mass spectrometry, as described in the next section.

1.3. Mass-Spectrometric Studies of Reactive Iron-Oxo Species

Mass spectrometry coupled with ESI ionization is ideally suited for detection of charged reactive species present in reaction mixtures in low concentrations⁸⁰ due to its excellent dynamic detection range up to one million.⁸¹ HRMS characterization is almost always employed in the field of biomimetic iron complexes to characterize new species and has often been the only method to prove the presence of the oxo unit in absence of other techniques.⁸²⁻⁸⁴ This was usually done with isotopic exchange of ¹⁶O isotope of oxygen for the ¹⁸O isotope. In a particularly intriguing example, Prat *et al.* reported observation of iron(V)-oxo-hydroxo species [(PyTACN)Fe^V(O)(OH)](OTf)⁺ by oxidizing [(PyTACN)Fe^{II}(OTf)₂] by H₂O₂ and ESI ionization of the resulting solution, using CryoSpray ESI source from Bruker, at low temperature (-40°C).⁸⁵ As the temperature was raised, the signal of the species decreased. Moreover, it exchanged one oxygen for ¹⁸O when mixed with H₂¹⁸O, and this was taken as evidence of Fe^V(O)(OH), where one of the oxygen atoms comes from water and the other from H₂O₂. In isobaric iron(III)-hydroperoxo complex, both oxygen atoms would come from the hydrogen peroxide and no exchange would be observed. This raised interest among mass spectrometrists, whether these species could be studied in the gas phase by other techniques.

Mass spectrometry has been long used to study oxidation reactions and allows us to work with extremely reactive species.⁸⁶ In order to reach the “holy grail” of controlled oxidation of methane to methanol at room temperature, Schwarz group has extensively studied gas-phase activation of methane.^{87,88,89} Particularly prominent was the oxidation of methane by [Fe^{III}O]⁺ cation,⁹⁰ which led to the formulation of the two state reactivity concept^{6,91-94} which is the notion that reaction involving transition metals often go through the minimum energy pathway involving potential surfaces of more than one multiplicity. Despite the broad range of ions capable of reacting even with methane discovered by

Schwarz, finding ligated ions retaining at least some of this reactivity turned out to be difficult.^{86,95}

Only a handful of biomimetic iron-oxo complexes have been rigorously studied in the gas phase, despite the routine use of ESI-MS for their characterization. Chiavarino *et al.* reported reactivity of $[(\text{TPFPP})\text{Fe}^{\text{V}}(\text{O})]^+$ (Figure 4a), which is an iron(IV)-oxo porphyrin radical (thus formal iron(V)) complex resembling “compound I” from cytochrome P450, with aliphatic and aromatic amines using FT-ICR mass spectrometer.⁹⁶ They observed three reaction pathways: electron transfer, hydride transfer and oxygen atom transfer. Later, the same group (Fornarini and Crestoni) reported reactions of the $[(\text{TPFPP})\text{Fe}^{\text{V}}(\text{O})]^+$ with alkenes and observed mostly oxygen atom transfer.⁹⁷ They do not mention whether they tried the reaction with less active substrates, like aromates though. Another similar study was conducted in a quadrupole ion trap by Donald *et al.*⁹⁸ They reported oxidation of MeOH and EtOH to aldehydes with the $[(\text{bpg})\text{Fe}^{\text{IV}}(\text{O})]^+$ ion (Figure 4b). Interestingly, they prepared the $[(\text{bpg})\text{Fe}^{\text{IV}}(\text{O})]^+$ ion by CID of $[(\text{bpg})\text{Fe}^{\text{III}}-\text{O}-\text{Fe}^{\text{III}}(\text{bpg})]^{2+}$, showing how gas-phase reactions can also be used for preparation of species unstable in solution, in this case against dimerization. Also employing gas-phase dissociation reactions, Schröder *et al.* tried to prepare high-valent iron nitride $[(\text{cyclam-ac})\text{Fe}^{\text{V}}(\text{N})]^+$ (Figure 4c) by dissociation of $[(\text{cyclam-ac})\text{Fe}^{\text{III}}(\text{N}_3)]^+$ azide. They succeeded to prepare the ion with correct m/z ratio, but based on the lack of bimolecular reactivity they (wrongly⁹⁹) concluded that the ion was a product of intramolecular oxidation and not the expected iron(V) nitride.¹⁰⁰ Later, Schlangen *et al.* succeeded to prepare iron(V)-nitrido complex $[(\text{pyN4})\text{Fe}^{\text{V}}(\text{N})]^{2+}$ (Figure 4d), which was highly reactive.¹⁰¹ Mas-Ballesté *et al.* carried out a CID study of iron(IV)-oxo complexes and they tried to prove their structure with the dissociation patterns.¹⁰² Assigning structure from the CID spectra of complex ligated species is, however, difficult at best, impossible at worst. In contrast to relatively simple systems like $[(\text{phen})\text{Cu}^{\text{III}}(\text{O})]^+$, the ligated iron(IV)-oxo ions will not typically lose oxygen, but degrade the ligand and then release an oxidized part of the ligand skeleton. Some success in this respect was achieved by Xu *et al.*, who described the use of DESI¹⁰³ to prepare iron(V) intermediate $[(\text{TPA}^*)\text{Fe}(\text{O})(\text{OH})]^{2+}$ (Figure 4e), which was characterized by CID.¹⁰⁴ However, the two main fragmentation channels of this complex were loss of water and loss of $\text{H}_2\text{O} + \text{H}$ [sic], none of which is convincing evidence for an iron-oxo intermediate.

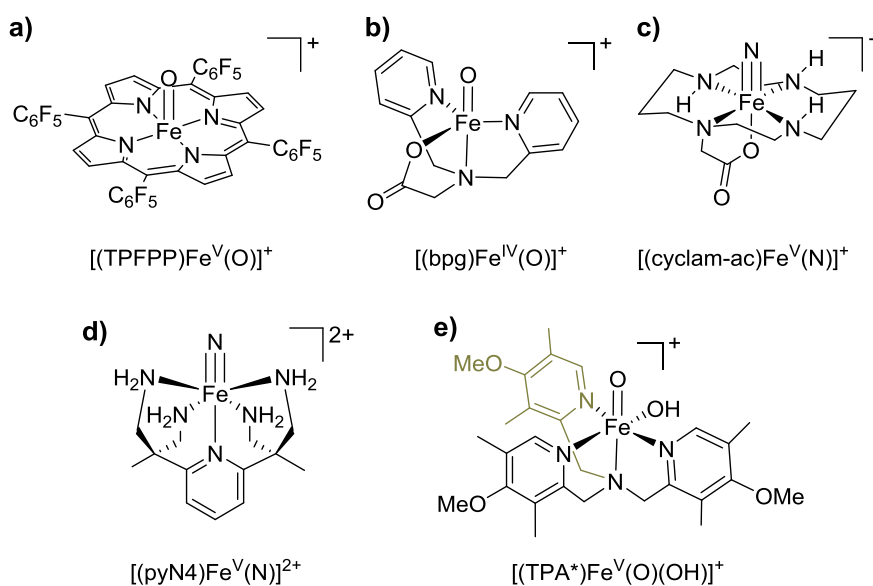


Figure 4. (a-e) Examples of reactive iron-oxo and nitrido species studied by mass spectrometry.

The requirements for the structural assignment of the ions observed in mass spectra stimulated the developments in ion spectroscopy.^{105–111} Ion spectroscopy enables us to obtain vis, IR and rotational¹¹² spectra of mass-selected ions. Comparison of these spectra with a suitable theoretical prediction method can lead to confident assignment of molecular structure. Moreover, it enables us to obtain spectroscopic characteristics that are difficult to predict, much like IR and UV/vis spectroscopies in solution.

The fundamental problem of ion spectroscopy lies in the detection of the photon absorption. Because the number of ions is typically very low, we cannot detect the changes in photon flux as in absorption spectroscopy. Instead, we have to rely on a process triggered by the photon absorption, which results in a change of the m/z ratio of the probed ions. In vis range, it is possible to measure photodissociation spectra of the ions resulting from the molecule fragmentation upon absorption of one or few photons. Due to the relatively high energy of the photons, this can be done using conventional laser setups.

However, in the IR range, the required photon flux becomes very big and therefore infrared multiphoton dissociation spectra (IRMPD) can be only measured at facilities equipped with a powerful source of IR light, such as free electron laser. It is also possible to combine IR and vis absorption in a number of schemes, but these require the presence of well-resolved vibronic transitions of suitable energy.

An alternative to IRMPD that has gained traction recently is the use of ion tagging methods. These rely on formation of weakly bound ionic complexes with so called tagging molecules (H_2O , N_2 , D_2 , Ar, Ne, He) at cryogenic temperatures which can be easily dissociated even with low-energy IR photons.^{113–118} Therefore, light absorption in these complexes can be detected by their dissociation. Binding of the tagging atom causes some disturbance to the structure, though. In this respect helium tagging offers by far the smallest binding energies and smallest disturbances to molecular structures.¹¹⁹ This results in very nicely resolved spectra. In our laboratory, $\sim 1 \text{ cm}^{-1}$ line widths, limited by the line width of the laser system can be achieved. Contrast this to typical line width of 10 cm^{-1} in IRMPD spectroscopy. Our particular approach, helium tagging infrared photodissociation spectroscopy (IRPD) consists in trapping the ions of interest in a cryogenic ion trap ($T = 3 \text{ K}$) filled with helium. The ions are cooled in collisions with the helium and form weakly bound helium complexes. The complexes are irradiated by a tunable laser and boil off the helium if they absorb a photon. We obtain the helium tagging spectra (IRPD or visPD, to distinguish the measured spectral region) as a dependence of the helium complex depletion on the light frequency.^{120,121} Additional details and experimental conditions are to be found in section 2.5.

The use of tagging action spectroscopies for reactive metal intermediates has been known for long time, but the applications in biomimetic chemistry were rare (Figure 5 shows species that bear some resemblance to iron-oxo complexes).^{122, 123} Therefore, we hypothesized that we could connect ion spectroscopy with the biomimetic iron-oxo chemistry and gain new insights into the structure and reactivity of the iron-oxo complexes.

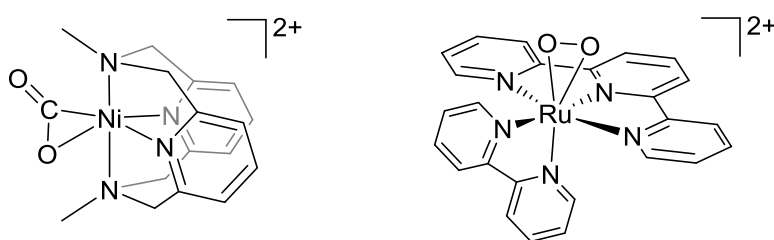


Figure 5. Examples of reactive metal intermediates studied by tagging spectroscopy from Refs 122,123.

1.4. Binding in the Metal-Oxo Complexes and the Oxo Wall.

The question, why Nature has chosen iron-oxo complexes (and to some extent manganese) to activate the oxygen for reaction with strong bonds is quite intriguing. Perhaps some reasons

for this lie in the electronic structure of metal-oxo complexes. In 1962, Ballhausen and Gray published their seminal work on the electronic structure of $[(\text{H}_2\text{O})_5\text{V}^{\text{IV}}(\text{O})]^{2+}$, which has an axially-compressed tetragonal field and found that electronic configuration of this ion was $(d_{xy})^1 (d_{xz})^0 (d_{yz})^0$, with π -antibonding d_{xz} and d_{yz} orbitals much higher than the d_{xy} orbital. Therefore, the M–O π bond order of d^0 and d^1 complexes is 2, and it decreases to 1.5 and 1 in d^3 and d^4 complexes, respectively. This decrease in bond order can be observed in lower M–O stretching frequencies.¹²⁴ Ultimately, as Gray and Winkler put it: “Three π^* electrons cannot be tolerated, so multiply bonded tetragonal d^5 oxos are not stable. With a d^4 limit, then, an oxo wall separates groups Fe–Ru–Os and Co–Rh–Ir in the periodic table.”¹²⁴ Alternatively, older observation by Holm: „M=O groups are stabilized at metal centers with an oxidation state of no less than 4+ and no more than four d electrons.“¹²⁵ These observations mostly apply in octahedral complexes¹²⁶ while complexes with trigonal or square planar or square pyramidal complexes can accommodate more electrons.^{127,128} The latter is the case in reported oxo complexes with more than four d electrons in Figure 6, except for $[(13\text{-TMC})\text{Co}^{\text{IV}}(\text{O})]^{2+}$, which adopts quartet electronic structure, where $d_x^2-y^2$ orbital gets occupied instead of d_{xz} or d_{yz} (and whose geometry is also pyramidal, rather than octahedral).¹²⁹

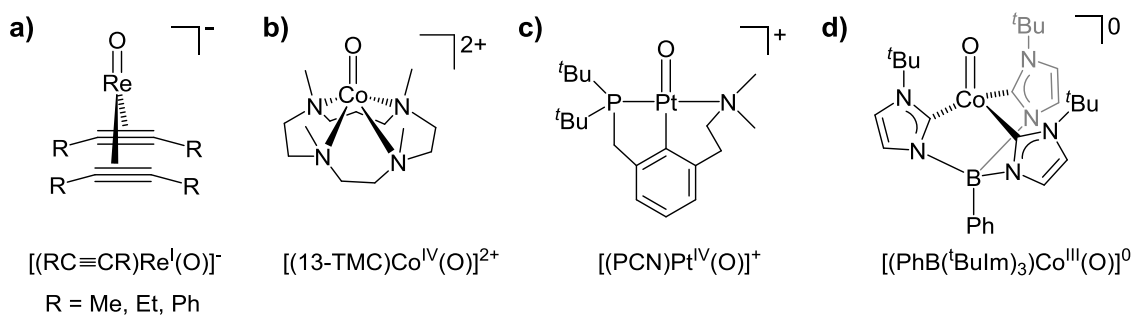


Figure 6. Reported (a,c,d; Refs 130-132) d^0 and (b; Ref. 129) d^5 metal-oxo complexes (see also d^5 iron(III)-oxo complexes in Figure 3a).

Iron(IV)-oxo complexes have four d electrons and therefore do not violate these rules. However, iron(III)-oxo complexes of tetragonal symmetry are good candidates to violate some definitions of these rules, because they would be d^5 configuration (note that the two already reported iron(III)-oxo complexes are of trigonal symmetry and moreover feature extensive hydrogen bonding networks). Iron(III)-oxo complexes can be also conceptually interesting, because the HAT reaction of iron(IV)-oxo species can be regarded as a combination of electron and proton transfers (Figure 7).¹³³⁻¹³⁵ The electron transfer is driven

by the electrophilicity of the active iron center, whereas the proton transfer depends on the basicity of the corresponding iron(III)-oxo compound. Access to the iron(III)-oxo compounds could therefore aid study of HAT reactions.^{136–139} Additionally, iron(III)-oxo intermediates have been implicated as intermediates in the ET-PT mechanism proposed for the reactions of iron(IV)-oxo complexes with electron-rich substrates, such as dimethylanilines.^{140–143} Also, these elusive species have been proposed to form in one-electron reduction of $[(\text{TMC})\text{Fe}^{\text{IV}}(\text{O})(\text{ACN})]^{2+}$ in dry acetonitrile.¹³⁹ Therefore, studying iron(III)-oxo species could shed light on the borderline cases of the oxo wall concept and on the reactivity of iron(IV)-oxo species with electron-rich substrates.

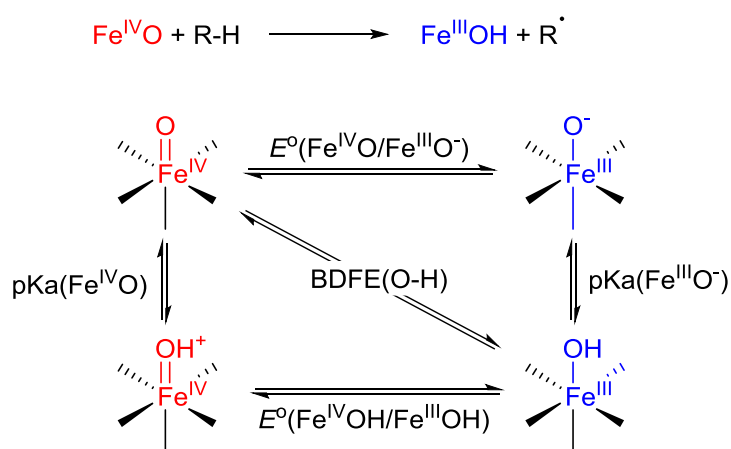


Figure 7. Thermodynamically equivalent paths to achieve a net HAT from R–H to iron(IV)-oxo complex. BDFE stands for bond dissociation free energy (See Ref. 144) and is used here instead of the more commonly used BDE, because pKa and E° both refer to free energies.

Aims of the Work

Biomimetic iron chemistry is an established field that involves investigation of reactive intermediates and currently employs IR and resonance Raman spectroscopy to detect iron-oxo vibrations. Because the investigated intermediates are not always present in sufficiently large quantities, the field could benefit from the superior sensitivity and flexibility of ion spectroscopy. More specifically, the aims of this work are:

- 1) Devise convenient methods of transfer or preparation of iron-oxo complexes in the gas phase.
- 2) By measuring benchmark iron(IV)-oxo data, establish the use of ion spectroscopy in the field of biomimetic chemistry.
- 3) Utilizing the mass-selection capabilities of the ion spectroscopy, study different species present in the solution and, if possible, establish the spectroscopic and chemical correlations between the gas phase and the condensed phase.
- 4) Study iron(III)-oxo complexes, which cannot be prepared in solution, using gas-phase techniques.

CHAPTER 2. Materials and Methods

2.1. Materials

Ligated iron(II) complexes used as the starting materials were obtained from our collaborators from the University of Girona (Prof. Miquel Costas) and the University of Minnesota (Prof. Lawrence Que, Jr.).

HPLC grade ACN (Fisher Scientific) and H_2^{18}O (95 % ^{18}O , Armar Chemicals) were used as received.

I synthesized 1,4-cyclohexadiene-1,2,3,4,5,6- d_6 by the Birch reduction according to a published procedure.¹⁴⁵⁻¹⁴⁷ I used *t*-BuOH as a proton donor and 0.1 mol of benzene- d_6 (99% D). The purity of the resulting material was verified by NMR spectroscopy. The 2.64 ppm (^1H) signal was used as a reference in the NMR measurement of the neat material. NMR spectra showed only minor impurities that were not taken into consideration in the following experiments (around 1 % of cyclohexene- d_6 , and around 1% of 1,4-cyclohexadiene- d_5). NMR spectra measured by Bruker Avance III 600 MHz spectrometer: ^1H NMR (600.17 MHz, CDCl_3): δ 2.64 (m, 2H); ^1H NMR (600.17 MHz, neat): δ 2.64 (m, 2H); ^2H NMR (92.13 MHz, neat): δ 5.73 (s, 4^2H), 2.65 (d, $J_{\text{DH}} = 2$ Hz, 2^2H); ^{13}C NMR (150.91 MHz, neat): δ 123.6 (t, $J_{\text{CD}} = 24.0$ Hz, 4C), 25.0 (dt, $J_{\text{CH}} = 127$ Hz, $J_{\text{CD}} = 19.4$ Hz, 2C).

I prepared ^{18}O labeled HNO_3 by an isotope exchange of HNO_3 with ^{18}O labeled water^{148,149}, by heating a mixture of ca. 30 mg of H_2^{18}O (95 % ^{18}O) with the same mass of 65% HNO_3 in a sealed polypropylene tube to 80°C for one day. I measured the isotopic labeling by mass spectrometry of nitrate-containing ions and estimated it to be 38 mol. % by measuring ESI spectrum of dilute sample in negative mode. I later found out that much better results can be obtained by heating the mixture in a sealed glass ampoule made of Pasteur pipette. This way I obtained 60 % ^{18}O -labeled nitric acid by heating a mixture of 41 mg of freshly-distilled 100 % nitric acid with 72 mg of ^{18}O -labeled water (95 % ^{18}O) to 90°C in the glass ampoule for 33 hours.

I prepared mixture of EtSH with EtSD to determine intermolecular kinetic isotope effects for reactions with ethanethiol (Table 8) by mixing EtSH with D_2O and removal of the organic layer. The EtSH/EtSD ratio in the collision cell of the TSQ 7000 instrument was

determined from a ligand exchange reaction with gold(I) complexes for which KIE of 1 was assumed.

Other chemicals and solvents were obtained from commercial sources.

2.2. Electrospray Ionization Mass Spectrometry

In this work, I focused on the study of ions in the gas phase, which are of relevance to the condensed phase. Therefore, I needed a technique that can transfer charged species from solution to the gas phase with minimum disturbance. I used ESI source¹⁵⁰ mounted on TSQ 7000 tandem mass spectrometer.^{151–152} The arrangement of the ESI ion source is shown in Figure 8. The solution is infused at a rate of approximately 100–300 $\mu\text{l/hr}$ through a 100/180 μm (internal/external diameter) fused-silica capillary with polyamide coating (Postnova Analytics GmbH). The infusion was done either by a standard syringe pump using glass syringe (7.28 mm internal diameter, 2.5 ml GASTIGHT 1000 series, Hamilton) or 1 ml plastic syringe (Injekt 1 mL LS Syringe, B. Braun Medical Inc.) or by an overpressure of nitrogen gas above the solution from a 2.5 ml glass vial in which one end of the capillary was submerged.

The solution in the capillary is connected to a high voltage (+ for positive ions) of several kilovolts in order to create an excess of charged species of one polarity at the spraying tip of the capillary. This results in the formation of Taylor cone, which emits small charged droplets towards the mass spectrometer orifice. The individual ions are released as these droplets evaporate by two main mechanisms: a series of droplet fission events resulting in only one charged molecule per droplet (charged residue model) or direct emission of individual ions from the droplets (ion evaporation model).¹⁵³ To evaporate the droplets more efficiently, the ion source is equipped with a nitrogen sheath gas source that flows around the capillary (typical pressures are 0–100 psi). The ions together with surrounding solvent vapors and nitrogen gas pass through a heated metal capillary into the vacuum section of the ion source. Here, most of the solvent and nitrogen molecules are removed by two-stage oil forepump and ions continue through a skimmer. By adjusting the voltages applied to the heated capillary and tube lens electrode (skimmer voltage is set to 0 V against the ground), the ions are accelerated at different rates through this intermediate vacuum region (pressure approximately 1 Torr). The accelerating potential placed at the tube lens electrode not only serves to push the ions towards the skimmer, but the collisions which the ions repelled from the electrode undergo can also cause a buildup of their internal energy this can lead to

fragmentation (illustrated as formation of "red" ions in Figure 8). This way of ion fragmentation is called "in source collision induced dissociation" (or in source CID). The ions are further transferred through skimmer to a transfer quadrupole region that is pumped by turbomolecular pumps to pressure less than 10 mTorr.

The transfer quadrupole region is the last region, where ions experience friction from collisions with a gas, before entering the main section of the mass spectrometer, and therefore sets the potential at which the ions entering the next stage of the instrument have minimum kinetic energy. Finally, the ions are focused by einzel lens to the mass selective quadrupole. Mass spectra were usually measured by scanning this first quadrupole mass and, after passing via octopole collision cell and second mass-selective quadrupole operating in the RF-only mode, the ions were detected by a Daly-type detector (conversion dynode + electron multiplier).

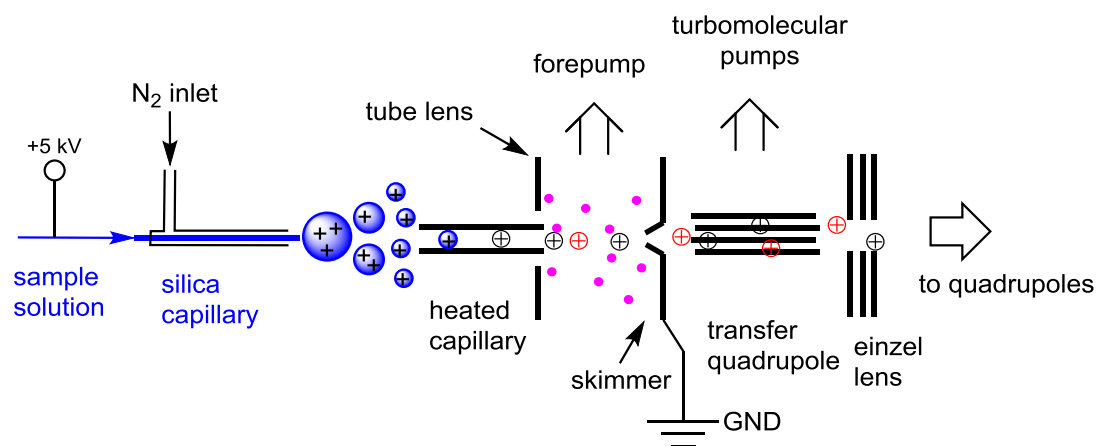


Figure 8. Schematic representation of the ESI ion source.

2.3. Preparation of Solutions Containing the Investigated Ions

Iron(IV)-oxo complexes that I investigated are listed in Figure 11. They were prepared by oxidation procedures published in the literature,^{45,137,154} by oxidation of the corresponding iron(II) triflate precursors dissolved in acetonitrile (typically 0.1-1 mM concentration). Oxidation of [(TMC)Fe^{II}(OTf)₂] by iodosobenzene afforded solution containing complexes **1** and **2**, oxidation of [(N4Py)Fe^{II}(OTf)₂] by iodosobenzene afforded solution containing complexes **4** and **5**, oxidation of [(PyTACN)Fe^{II}(OTf)₂] by peracetic acid afforded solution containing complexes **6** and **7**. The azide complex **3** was generated by addition of 1 equivalent of sodium azide to the solution of **1/2**. Similarly, complexes **8**, **9** and **10** were prepared by addition of 2, 0.3 and 2 equivalents of the HNO₃, CF₃COOH and HClO₄,

respectively, to the solution containing **6/7**. The complexes were transferred to the gas phase by an ESI ion source at mild ionization conditions (capillary temperature about 60°C and low voltage differences in the ion transfer region of the ESI source).

The solution containing $[(\text{TMC})\text{Fe}^{\text{IV}}(\text{O})(\text{ACN})]^{2+}$ (**1**, m/z 184.5) and $[(\text{TMC})\text{Fe}^{\text{IV}}(\text{O})(\text{OTf})]^+$ (**2**, m/z 477) was prepared by mixing 90 μl of 2 mM $[(\text{TMC})\text{Fe}^{\text{II}}(\text{OTf})_2]$ solution in ACN with 9 μl of 20 mM solution of PhIO in MeOH at $\sim -40^\circ\text{C}$. After 5 minutes, the solution was diluted with 1 ml of acetonitrile at room temperature. The ^{18}O labeling was carried out by addition of 10 μl of H_2^{18}O to this solution. Alternatively, the solution was also made by oxidation of 2 mM solution of $[(\text{TMC})\text{Fe}^{\text{II}}(\text{OTf})_2]$ with an excess of solid PhIO at room temperature. The solutions were cooled to -10°C during the measurement. Spraying conditions were: 4.5 kV spray voltage, 120°C capillary temperature, 0 V capillary voltage, 80 V tube lens voltage, 8 psi of N_2 sheath gas. The flow rate was 60 $\mu\text{l hr}^{-1}$.

$[(\text{TMC})\text{Fe}^{\text{IV}}(\text{O})(\text{N}_3)]^+$ (**3**, m/z 370) was prepared by mixing the solution of **1** (*vide supra*) with 1 eq. of NaN_3 in the form of 40 mM water solution. Spraying conditions: 6.5 kV spray voltage, 100°C capillary temperature, 0 V capillary voltage, 50 V tube lens voltage, 30 psi of N_2 sheath gas. The flow rate was 80 $\mu\text{l hr}^{-1}$.

The solution containing $[(\text{N4Py})\text{Fe}^{\text{IV}}(\text{O})]^{2+}$ (**4**, m/z 219.5) and $[(\text{N4Py})\text{Fe}^{\text{IV}}(\text{O})(\text{OTf})]^+$ (**5**, m/z 588) was prepared by oxidation of 2 mM $[(\text{N4Py})\text{Fe}^{\text{II}}(\text{OTf})_2]$ solution in acetonitrile by solid PhIO or 2-(tert-butylsulfonyl)iodosylbenzene. Spraying conditions: 6.5 kV spray voltage, 100°C capillary temperature, 0 V capillary voltage, 50 V tube lens voltage, 30 psi of N_2 sheath gas. The flow rate was 80 $\mu\text{l hr}^{-1}$.

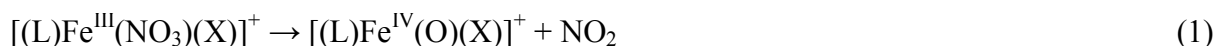
The solution from which $[(\text{PyTACN})\text{Fe}^{\text{IV}}(\text{O})(\text{ACN})]^{2+}$ (**6**, m/z 180.5) and $[(\text{PyTACN})\text{Fe}^{\text{IV}}(\text{O})(\text{OTf})]^+$ (**7**, m/z 469) were sprayed was prepared by sequentially adding into 900 μl of acetonitrile: 100 μl of 1 mM solution of $[(\text{PyTACN})\text{Fe}^{\text{II}}(\text{OTf})_2]$ in acetonitrile and 20 μl of 20 mM solution of AcOOH in acetonitrile (4 eq.). In the case of ^{18}O labeling, 10 μl of H_2^{18}O was also added (^{18}O exchange takes place at RT in about 5 minutes). The resulting solution was kept in a syringe cooled at -10°C during spraying. Spraying conditions: 4.5 kV spray voltage, 120°C capillary temperature, 0 V capillary voltage, 60 V tube lens voltage, 30 psi of N_2 sheath gas. The flow rate was 40 $\mu\text{l hr}^{-1}$.

$[(\text{PyTACN})\text{Fe}^{\text{IV}}(\text{equatorial-O})(\text{NO}_3)]^+$ (**8_{eq}**) was prepared in mixture with **8_{ax}** where **8_{eq}** dominated, by sequentially adding into 900 μl of acetonitrile: 100 μl of 1 mM solution of $[(\text{PyTACN})\text{Fe}^{\text{II}}(\text{OTf})_2]$ in acetonitrile, 20 μl of 20 mM solution of AcOOH in acetonitrile (4

eq.), waiting for 3 minutes, then adding 10 μl of 20 mM HNO_3 solution in acetonitrile (2 eq.). In the case of ^{18}O labeling, 10 μl of H_2^{18}O was also added (^{18}O exchange takes place at RT in about 5 minutes). The resulting solution was kept in a syringe cooled at -10°C during spraying. Spraying conditions: 4.5 kV spray voltage, 120°C capillary temperature, 0 V capillary voltage, 60 V tube lens voltage, 30 psi of N_2 sheath gas. The flow rate was $40 \mu\text{l hr}^{-1}$. Resulting spectrum in dependence of ionization conditions is shown in Figure 10a.

To enhance the ion signal of **8**, I used $[(\text{PyTACN})\text{Fe}^{\text{II}}(\text{NO}_3)_2]$ in some experiments instead of the $[(\text{PyTACN})\text{Fe}^{\text{II}}(\text{OTf})_2]$. I used the procedure used in similar ion exchange reactions previously.¹⁵⁵ Amberlite resin was washed and decanted with water (50 ml) twice and it was poured into a chromatographic column (2 cm diameter). Then it was washed with water (2 x 50 ml), 5M aqueous KNO_3 (60 ml), water (50 ml), 1M aqueous HNO_3 (60 ml) and with water (1000 ml in total) until the pH of the water coming out from the column reached ~ 7 . The column was loaded with the iron complex (36.6 mg) in water (4 ml) and eluted with water (30 ml) to yield yellow solution. Evaporation of the solution afforded 26.0 mg (quant.) of iron(II)-nitrate complex as greenish solid. Successful exchange of triflate ligands was confirmed by ESI-MS.

Alternative way of generation of complexes **7**, **8**, **9** and **10** was the elimination of nitrogen dioxide radical from their $[(\text{PyTACN})\text{Fe}^{\text{III}}(\text{NO}_3)(\text{X})]^+$ precursors during the electrospray ionization (Equation (1)):¹⁵⁶



Corresponding MS/MS spectrum of this dissociation in the case of complex **8** is shown in Figure 9a.

$[(\text{PyTACN})\text{Fe}^{\text{IV}}(\text{axial-O})(\text{NO}_3)]^+$ (**8_{ax}**) was prepared in mixture with **8_{eq}**, where **8_{ax}** dominated, by sequentially adding into 900 μl of acetonitrile: 100 μl of 1 mM solution of $[(\text{PyTACN})\text{Fe}^{\text{II}}(\text{OTf})_2]$ (or the nitrate, see above) in acetonitrile, 20 μl of 2.5 mM H_2O_2 solution (1 eq. to oxidize iron(II) to iron(III)) and 20 μl of 20 mM HNO_3 in acetonitrile (4 equivalents; omitted in the case of using iron nitrate). Spraying conditions: 6 kV spray voltage, 170°C capillary temperature, 20 V capillary voltage, 87 V tube lens voltage, 20 psi of N_2 sheath gas. The flow rate was $40 \mu\text{l hr}^{-1}$. Influence of the ionization conditions on the resulting mass spectra are shown in Figure 10. It shows, that maximum generation of iron(IV)-oxo complex is achieved at hard ionization conditions (120 V tube lens). The final optimized conditions were slightly different (see above).

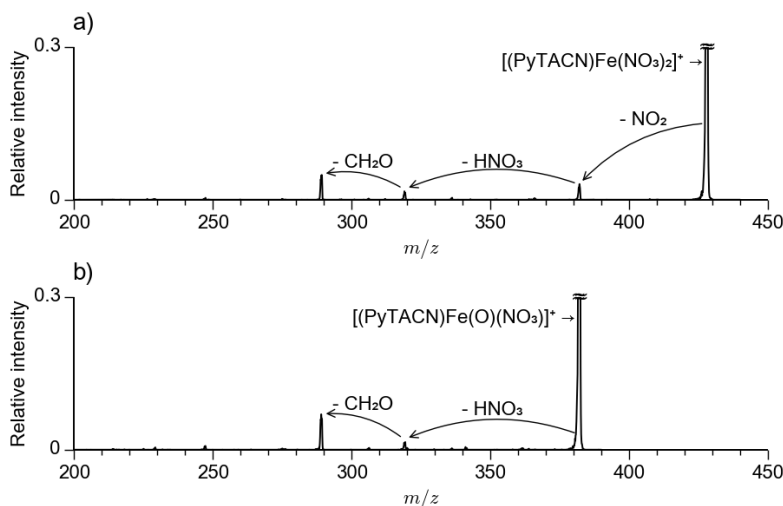


Figure 9. Collision-induced dissociation spectra with xenon as a collision gas at $E_{\text{cm}} = 5$ eV, $p = 0.1$ mTorr. (a) $[(\text{PyTACN})\text{Fe}^{\text{III}}(\text{NO}_3)_2]^+$ (m/z 428), (b) gas-phase generated $[(\text{PyTACN})\text{Fe}^{\text{IV}}(\text{O})(\text{NO}_3)]^+$ (m/z 382).

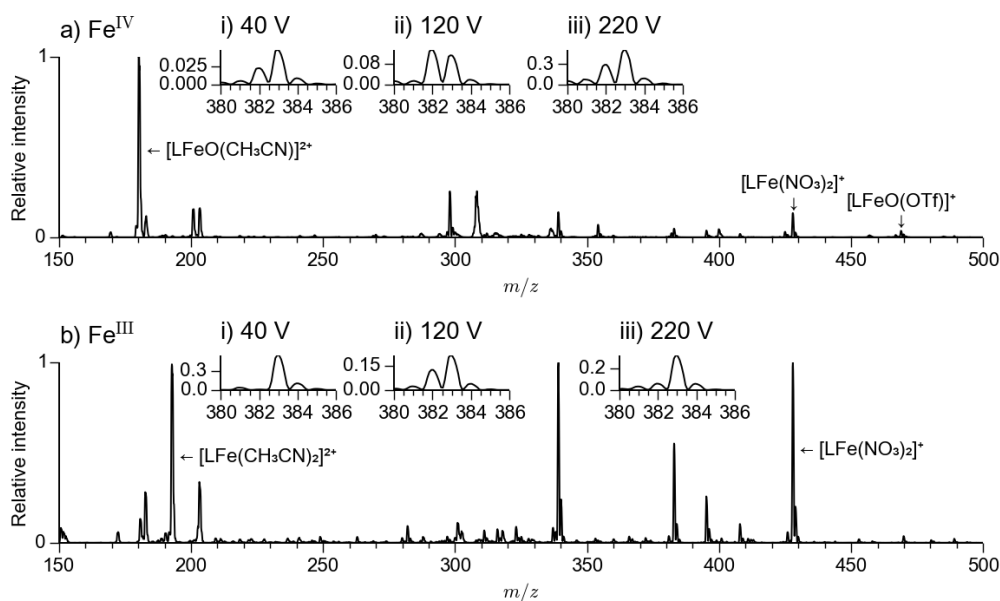


Figure 10. ESI-MS spectra of (a) a solution containing $[(\text{PyTACN})\text{Fe}^{\text{IV}}(\text{O})(\text{NO}_3)]^+$ complexes ($\mathbf{8}_{\text{eq}}$), (b) a solution of with $[(\text{PyTACN})\text{Fe}^{\text{III}}(\text{NO}_3)_2]^+$ complexes used for in-source generation of the iron(IV) complexes $\mathbf{8}_{\text{ax}}$ (both ESI-MS spectra measured with tube lens voltage 40 V). Insets show the mass range around m/z 382 ($[(\text{PyTACN})\text{Fe}^{\text{IV}}(\text{O})(\text{NO}_3)]^+$) with the tube lens voltages (i) 40 V, (ii) 120 V and (iii) 220 V. Capillary temperature was 40°C , capillary voltage was 0 V, auxiliary gas flow was 600 l hr^{-1} and no sheath gas was used.

$[(\text{PyTACN})\text{Fe}^{\text{IV}}(\text{equatorial-O})(\text{CF}_3\text{COO})]^+$ (**9_{eq}**) was prepared in mixture with **9_{ax}**, where **9_{eq}** dominated, by sequentially adding into 900 μl of acetonitrile: 100 μl of 1 mM solution of $[(\text{PyTACN})\text{Fe}^{\text{II}}(\text{OTf})_2]$ in acetonitrile, 20 μl of 20 mM solution of AcOOH in acetonitrile (4 eq.), waiting for 3 minutes, then adding 10 μl of 20 mM CF_3COOH solution in acetonitrile (2 eq.). In the case of ^{18}O labeling, 10 μl of H_2^{18}O was also added (^{18}O exchange takes place at RT in about 5 minutes). The resulting solution was kept in a syringe cooled at -10°C during spraying. Spraying conditions: 6.5 kV spray voltage, 120°C capillary temperature, -20 V capillary voltage, 60 V tube lens voltage, 45 psi of N_2 sheath gas. The flow rate was $80\ \mu\text{l}\ \text{hr}^{-1}$.

$[(\text{PyTACN})\text{Fe}^{\text{IV}}(\text{axial-O})(\text{CF}_3\text{COO})]^+$ (**9_{ax}**) was prepared by sequentially adding into 900 μl of acetonitrile: 100 μl of 1 mM solution of $[(\text{PyTACN})\text{Fe}^{\text{II}}(\text{OTf})_2]$ in acetonitrile, 20 μl of 2.5 mM H_2O_2 solution (1 eq. to oxidize iron(II) to iron(III)), 10 μl of 20 mM HNO_3 in acetonitrile (2 eq.) and 1.5 μl of 20 mM CF_3COOH in acetonitrile (0.3 eq.). Spraying conditions: 6.5 kV spray voltage, 150°C capillary temperature, 0 V capillary voltage, 90 V tube lens voltage, 45 psi of N_2 sheath gas and $100\ \text{l}\ \text{hr}^{-1}$ of N_2 auxiliary gas. The flow rate was $40\ \mu\text{l}\ \text{hr}^{-1}$.

$[(\text{PyTACN})\text{Fe}^{\text{IV}}(\text{O})(\text{ClO}_4)]^+$ (**10**) from the solution was prepared analogously to **8_{eq}**, using HClO_4 instead of HNO_3 . In the case of generation in the gas phase, 2 equivalents of HClO_4 and 2 equivalents of HNO_3 were used instead of 4 equivalents of HNO_3 and other aspects were identical as in the generation of **8_{ax}**.

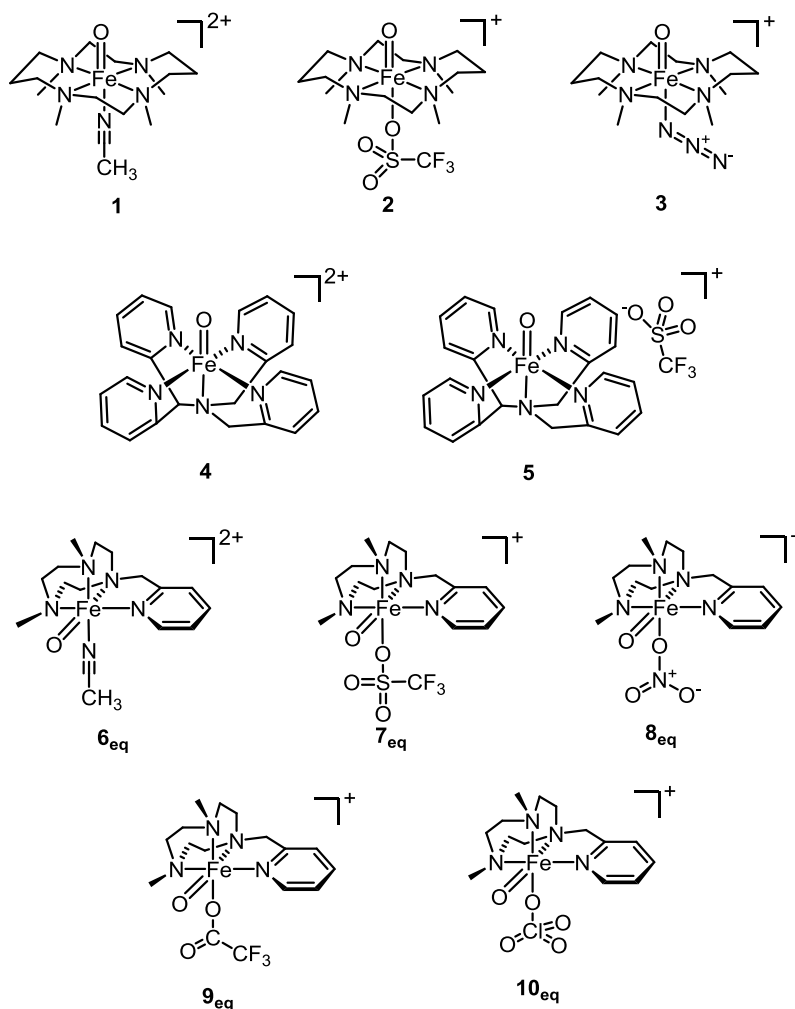


Figure 11. Studied iron(IV)-oxo complexes.

Iron(III)-oxo complexes (Figure 12) were formed from by the NO_2 elimination from their $[(\text{L})\text{Fe}^{\text{II}}(\text{NO}_3)]^+$ precursor ions, similarly to iron(IV)-oxo complexes.¹⁵⁶ Typical spectra, along with the ionization conditions are shown in Figure 13. Similarly, ^{18}O -labeled $[(\text{L})\text{Fe}^{\text{III}}(^{18}\text{O})]^+$ ions were prepared using ^{18}O -labeled nitric acid.¹⁵⁷ Alternatively, the iron(III)-oxo ions **11** and **14_{anti}** were prepared from the corresponding iron(IV)-oxo complexes **4** and **1** by one-electron reduction in the gas phase. Specifically, I introduced gaseous tetrakis(dimethylamino)ethylene (TDAE) at ~ 0.5 Torr pressure in the transfer quadrupole collision cell (described on page 27) mounted onto the transfer quadrupole in the electrospray ionization source. This led to the formation of iron(III)-oxo complexes along with the TDAE cation radical (Equation (2), Figure 13c).



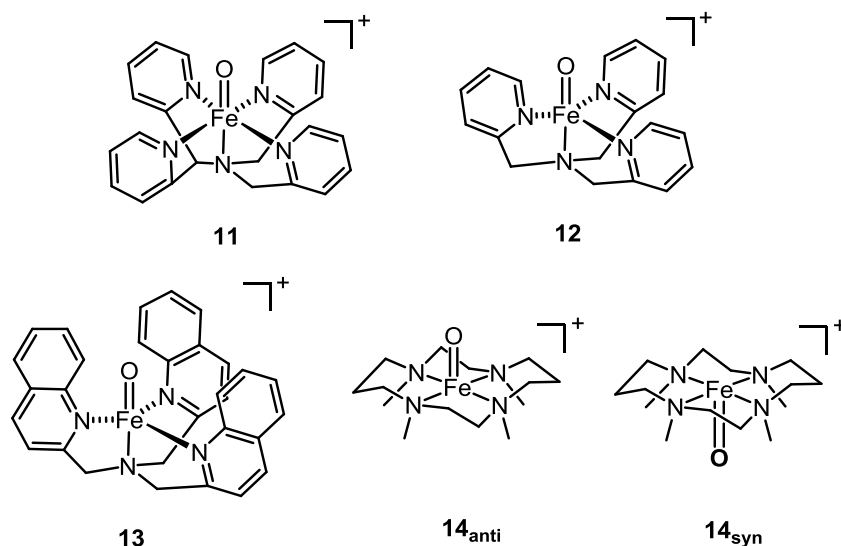


Figure 12. Studied iron(III)-oxo complexes.

Complexes of iron(III)-oxo ions with water. Formation of complexes of iron(III)-oxo complexes **11-13** with water was achieved in the cold trap of the ISORI instrument by controlling the helium pulse sequence - it required several hundred millisecond long opening of the helium piezo valve. The complexes resulted from reaction between the iron(III)-oxo complexes and trace water molecules present in the cold trap.

Generation of $[\text{Fe}^{\text{III}}\text{O}]^+$ for the reactivity calibration. For the determination of absolute rate constants, the experimental setup was calibrated by measurement of the known reaction between $[\text{Fe}^{\text{III}}\text{O}]^+$ and methane. $[\text{Fe}^{\text{III}}\text{O}]^+$ was generated according to a published procedure by spraying 10 mM iron(III) nitrate solution in water (Figure 14a).¹⁵⁶ Conditions: capillary temperature 200°C, capillary voltage 100 V, tube lens voltage 130 V, N_2 sheath gas pressure 20 psi, N_2 auxiliary gas flow 10 l/min.

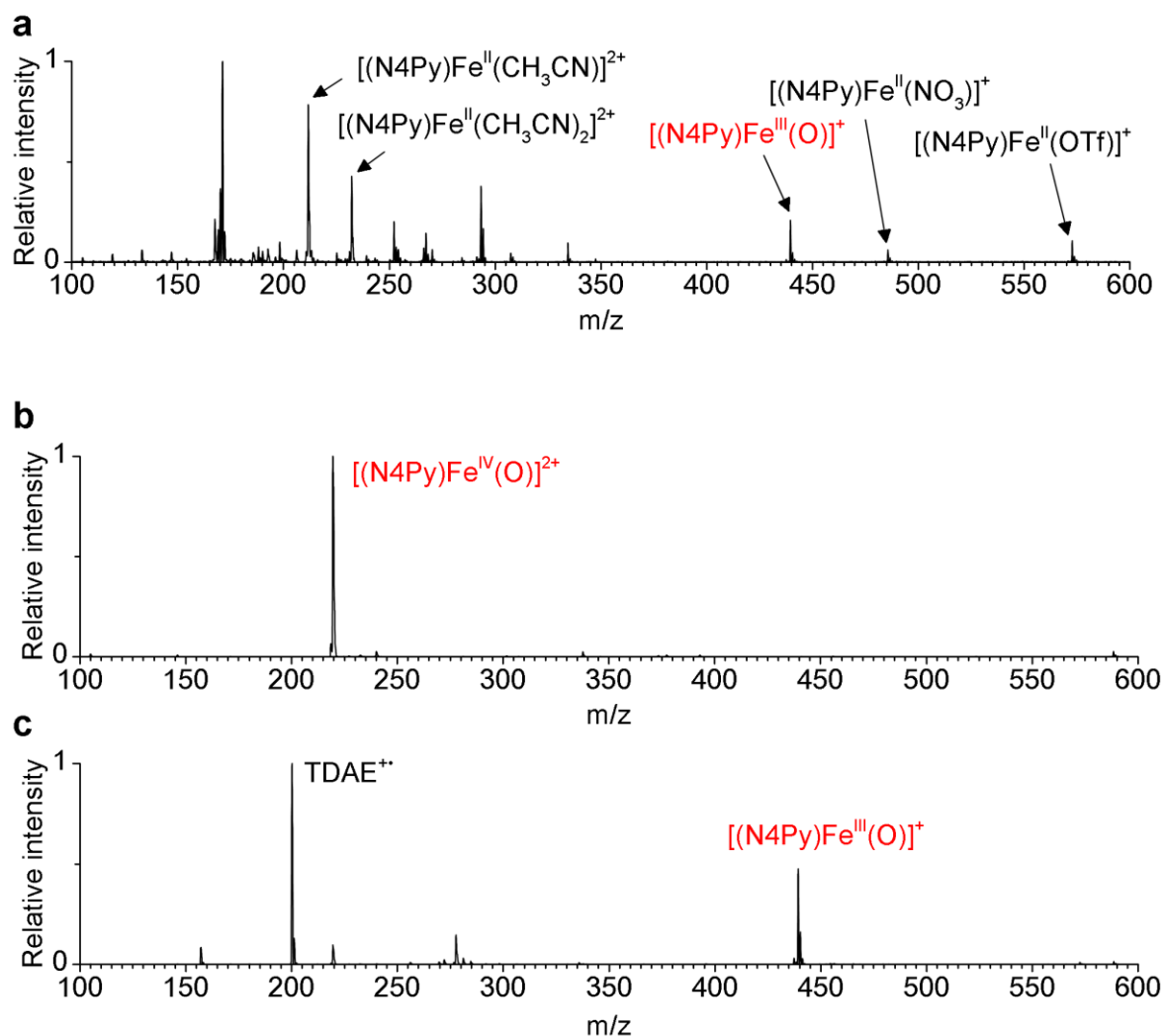


Figure 13. Ionization conditions and mass spectra for generation of iron(III)-oxo complexes. (a) Mass spectrum of 50 μM solution of $[(\text{N}4\text{Py})\text{Fe}^{\text{II}}(\text{OTf})_2]$ with 6 equivalents of nitric acid (diluted from concentrated aqueous nitric acid) in acetonitrile. Typical ESI settings: 5 kV capillary voltage, 40 psi sheath gas pressure, 120 $^\circ\text{C}$ capillary temperature, 0 V capillary voltage and 80-120 V tube lens voltage, 0.1 ml hr^{-1} flow rate. The peak at m/z 485 represents the $[(\text{N}4\text{Py})\text{Fe}^{\text{II}}(\text{NO}_3)]^+$ cation, whereas the peak at m/z 439 corresponds to the $[(\text{N}4\text{Py})\text{Fe}^{\text{III}}(\text{O})]^+$ cation **11**. Complexes **12–14** were obtained under analogous conditions (d-f, panel (e) shows the use of ^{18}O -labeled nitric acid to obtain ^{18}O labeled **14**). (b) Mass spectrum of solution containing the iron(IV)-oxo complex $[(\text{N}4\text{Py})\text{Fe}^{\text{IV}}(\text{O})]^{2+}$ (**4**). The solution was prepared by mixing 100 μl of 1 mM solution of $[(\text{N}4\text{Py})\text{Fe}^{\text{II}}(\text{OTf})_2]$ in acetonitrile with an excess of solid iodosobenzene and diluting the resulting solution to 3 mL with acetonitrile. The ionization conditions were similar as in (a) with lower tube lens voltage (~ 40 V). Panel (c) shows the spectrum measured at identical ionization conditions as in (b); however, gaseous tetrakis(dimethylamino)ethylene (TDAE; pressure ~ 0.5 Torr) was introduced in a 3-cm-long collision cell located in the transfer quadrupole of the electrospray ionization source. Collisions of TDAE with $[(\text{N}4\text{Py})\text{Fe}^{\text{IV}}(\text{O})]^{2+}$ yielded complex **11** and TDAE^{2+} (m/z 200). The same procedure (reduction of iron(IV)-oxo complex with TDAE) was used to prepare complex **14_{anti}** (panels g,h).

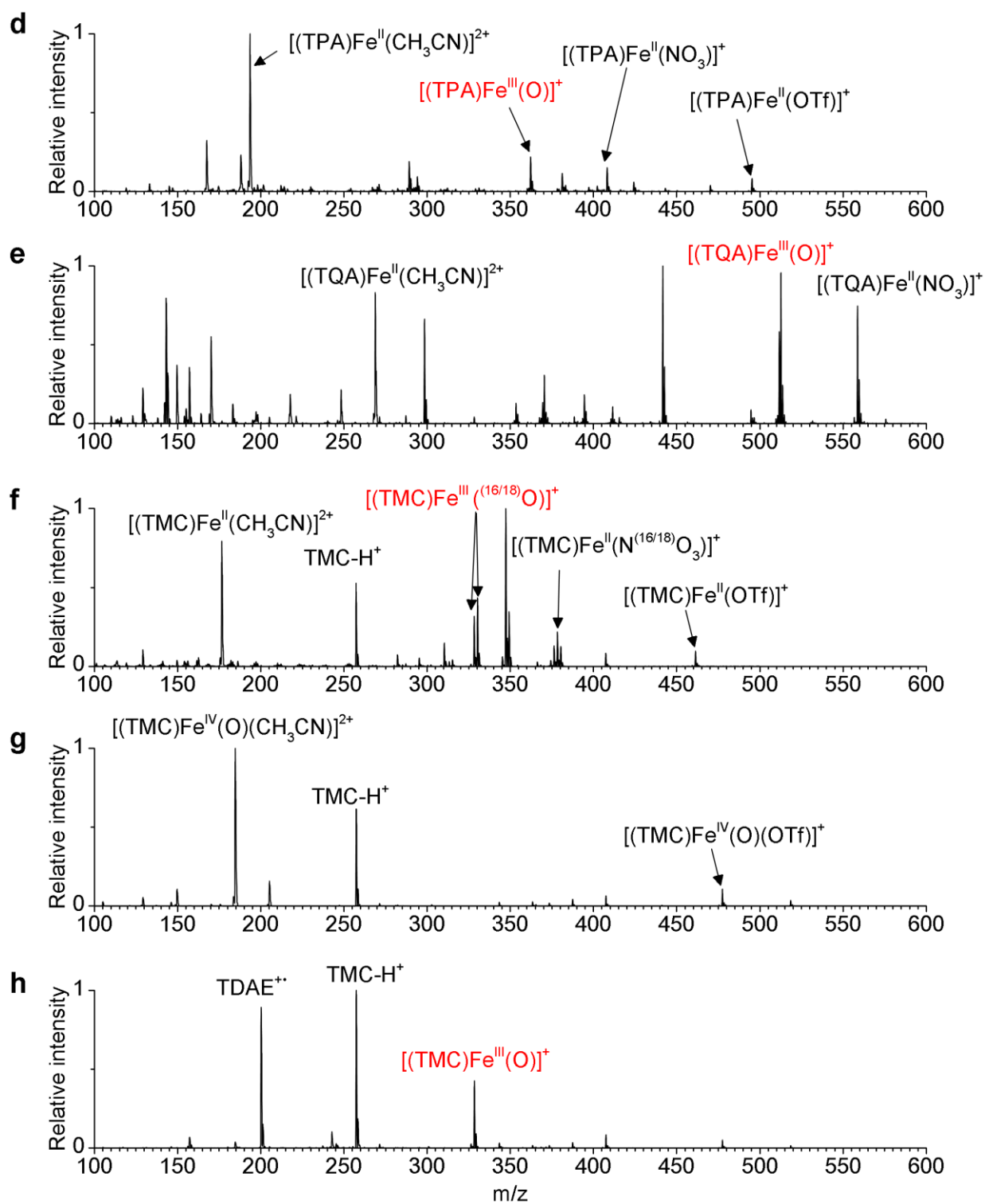


Figure 13. (continued).

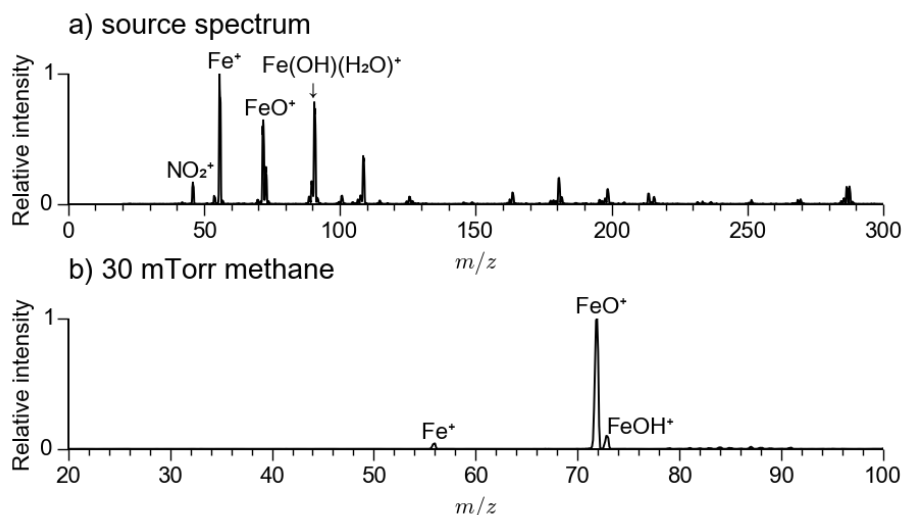


Figure 14. (a) ESI-MS spectrum of the 10 mM aqueous solution of $\text{Fe}^{\text{III}}(\text{NO}_3)_3$. (b) Reaction of the mass-selected $[\text{Fe}^{\text{III}}\text{O}]^+$ (m/z 72) with methane at nominally zero collision energy. We can observe OAT (Fe^+ , m/z 56) and HAT ($[\text{Fe}^{\text{II}}\text{OH}]^+$, m/z 73).

2.4. Ion-Molecule Reactions

The TSQ 7000 instrument has two mass-selective quadrupoles and an octopole collision cell (Figure 15). After the ions leave the transfer quadrupole, the first quadrupole mass-selects the studied ions, which then undergo collisions with a neutral reagent in the octopole collision cell. The kinetic energy of these collision events can be varied by with varying electric potential of this octopole with respect to the transfer quadrupole (or, more precisely, against the nominally zero collision energy potential that is determined from retarding potential analysis described later). The products of these collisions are mass-analyzed by the third quadrupole (whose potential is set to the sum of the transfer quadrupole and the collision cell potentials) and detected with a Daly-type detector. In these experiments, the two crucial parameters are (i) pressure of the neutral reactant and (ii) the kinetic and internal energy of the reacting ions.

(i) In order to measure the pressures of the gaseous reactants, the collision cell in TSQ 7000 is equipped with a Pirani gauge that works by measuring heat conductance. However, this pressure gauge is sensitive to the chemical composition of the gas. Therefore, I changed it to 120 AA Baratron pressure gauge (MKS Instruments) that operates as a membrane pressure gauge and is therefore capable to measure all gases without the need of recalibration for each used gas.

(ii) The energy distribution of the ions passing through the collision octopole region has been measured indirectly using the retarding potential analysis method.¹⁵⁸ This method works by changing the offset of the octopole cell and observing changes of the ion current.

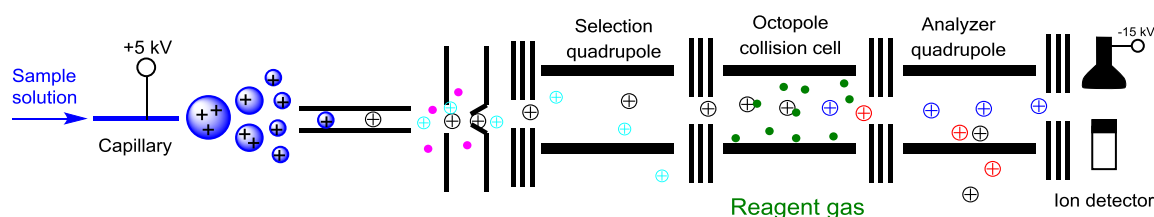


Figure 15. Scheme of the TSQ 7000 instrument (transfer quadrupole not shown).

As the potential of the collision octopole (denoted as U_{oct} in Figure 16) is lowered, more ions have sufficient energy to cross it. When the derivative is plotted, one can obtain the shape of the energy distribution. The kinetic energy of the ions with respect to the collision cell is given by the difference of the potential at the maximum derivative of the ion current with respect to the collision cell offset (which is approximately equal to the offset of the transfer quadrupole in the ion source region and the actual collision cell offset). When it is desirable to get as slow ions as possible to allow for a long reaction time, the U_{oct} needs to be set at the potential corresponding to the maximum of the derivative of the ions current U_{zero} . This is referred to as the nominally zero collision energy (the real energy is always above zero and its minimal value is limited by the FWHM of the energy distribution). The kinetic energy of the ions with respect to the collision cell (E_{lab}) is given by $E_{\text{lab}} = Z e (U_{\text{oct}} - U_{\text{zero}})$, where Z is the integer charge of the ions and e is the elementary charge. For studying the collisions with a gas, it is more convenient to express the collision energy in the center of mass reference frame (E_{cm}). This gives the maximum amount of energy which is dissipated in an inelastic collision. It is related to the kinetic energy with respect to the collision cell by formula

$$E_{\text{cm}} = E_{\text{lab}} m / (M + m) \quad (3),$$

where M is the mass of the ion and m is the mass of the collision gas.

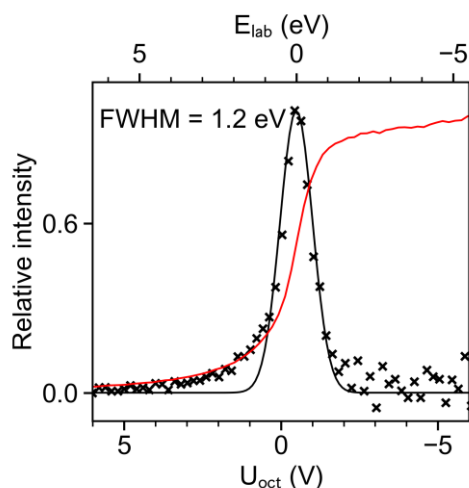


Figure 16. Typical ion kinetic energy distribution measured for studied iron-oxo species by the retarding potential analysis. The full width at half maximum (FWHM) of the measured distribution was in the range 0.7 to 1.5 eV. Red trace corresponds to the ion current, whereas the black crosses correspond to the derivative of the ion current according to the offset potential. The black line is a Gaussian fit to the derivative.

Another important factor determining the reactivity is the amount of internal energy, or the temperature of the ions. This is most relevant, when the ions are formed "hot" in collisions with the nitrogen gas in the tube lens region. Therefore, I adapted our TSQ 7000 with another collision cell in transfer quadrupole region. The dimensions of this cell are 3 cm diameter, 2 cm length and 1.5 cm holes for the quadrupole. I tested for reactivity changes with the pressure in this collision cell. Fortunately, the reactivity did not change, indicating that the ions already reached and equilibrium temperature with the instrument (typically 40°C to 70°C depending on the exact measurement).

The mass spectra of the products obtained after collision with the reactant gas were analyzed with the assumption, that no ions are lost in the process. Thus, for the reaction $P \rightarrow F_1 + F_2 + \dots + F_N$, where P is the reactant (parent) and $F_1 \dots F_N$ are the products with intensities I_P and $I_1 \dots I_N$, the cross section σ_i is defined determined as¹⁵⁸

$$\sigma_i d \ell = -\ln(1 - \Sigma I_n / (\Sigma I_n + I_P)) I_i / \Sigma I_n \quad (4),$$

where ΣI_n is the sum of the intensities of all products, d is the gas number density in the collision cell and ℓ is the collision cell length.

Alternatively, the cross sections can be converted to the rate constants by utilizing the relation

$$\sigma_i d \ell = k d t \quad (5),$$

where t is the mean residence time in the reaction cell. This can be calculated from the measured energy distribution, but in this case it was determined by measuring the cross section of a known reaction of $[\text{Fe}^{\text{III}}\text{O}]^+$ with methane (Figure 14b, Figure 19).¹⁵⁹ In our instrument, the t has been determined as 0.93 milliseconds.

Note that our instrument was operating in an unintentional ion trapping mode (as can be seen from the time almost 1 millisecond). Therefore, I employed longer scan times to obtain ion intensities as the stationary state.

The reactions rates were also usually measured at different pressures and linear slope of the reaction rate was taken.

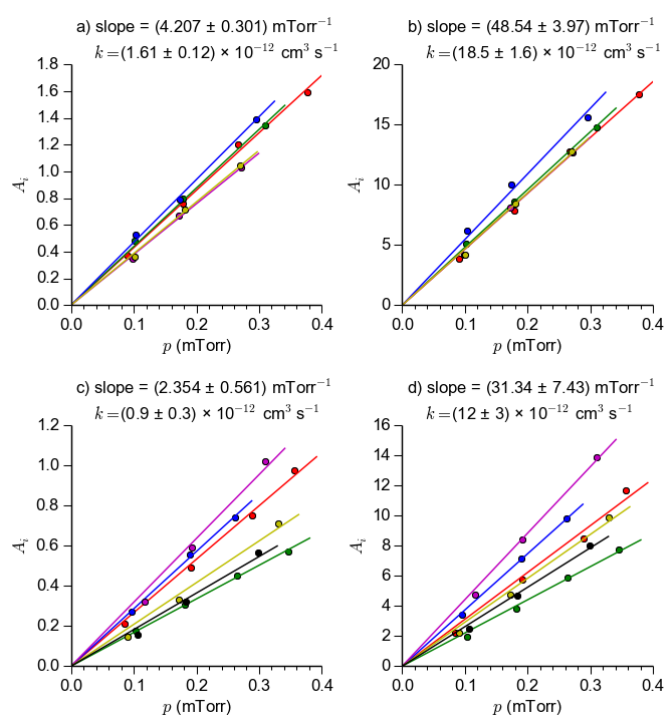


Figure 17. Reaction of 1,4-cyclohexadiene with $[(\text{PyTACN})\text{Fe}^{\text{IV}}(\text{O})(\text{NO}_3)]^+$ (a, b) generated in the gas phase (c,d) transferred from solution. Subplots (a) and (c) show the OAT reaction channel, whereas subplots (b) and (d) show the HAT reaction channel. Points are the experimental data, lines are the result of linear regression. The average slope of each set of lines is shown in the respective subplot. Total intensity of neglected fragments was $<2\%$.

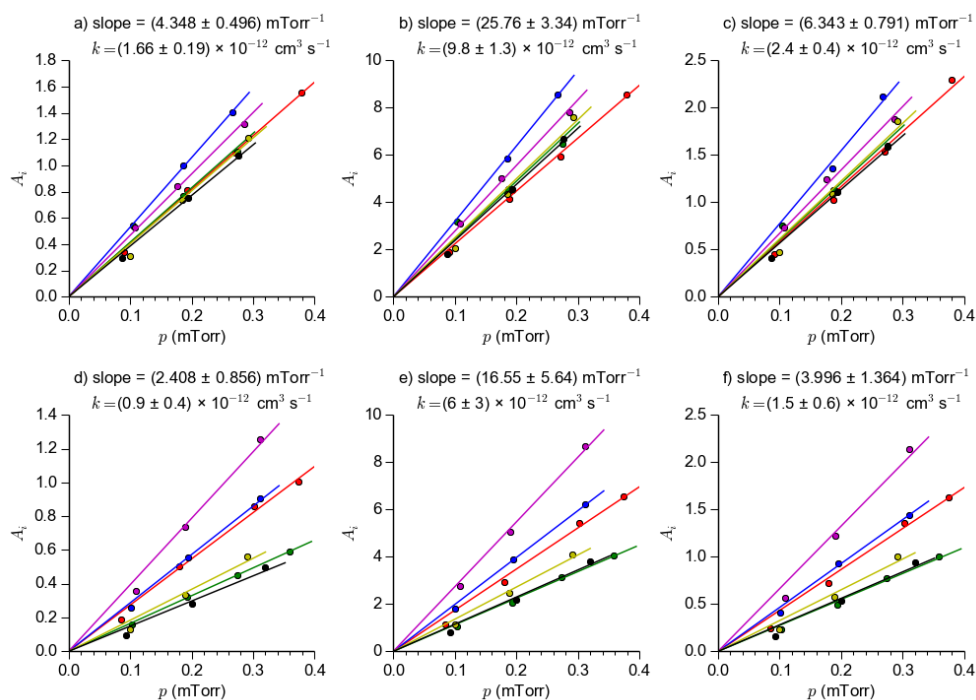


Figure 18. Reaction of 1,4-cyclohexadiene-1,2,3,4,5,6-d₆ with [(PyTACN)Fe^{IV}(O)(NO₃)]⁺ (a, b, c) generated in the gas phase or (d, e, f) transferred from solution. Subplots (a) and (d) show the OAT reaction channel, subplots (b) and (e) show the HAT reaction channel and subplots (c) and (f) show the DAT reaction channel. Points are the experimental data, lines are the result of linear regression. The average slope of each set of lines is shown in the respective subplot. Total intensity of neglected fragments was <2 %.

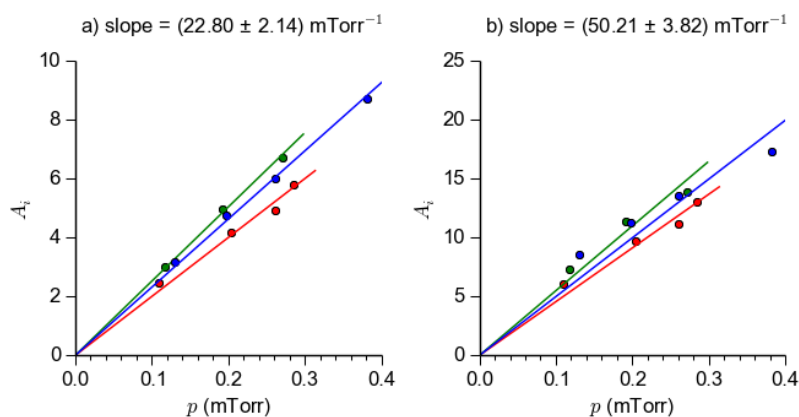


Figure 19. Reaction of methane with [Fe^{III}O]⁺. (a) OAT reaction channel, (b) HAT reaction channel. Points are the experimental data, lines are the result of linear regression. The average slope of each set of lines is shown in the respective subplot. Total intensity of neglected fragments was <10 %.

2.5. Infrared and Visible Ion Spectroscopy

In our laboratory, we have the unique capability to measure IR^{160, 161} and vis¹⁶² photodissociation spectra of the ions. All of the used techniques belong to action spectroscopy, where we monitor changes in m/z ratio of the ions as the consequence of laser irradiation. In this thesis, several action spectroscopic techniques are used. In the visible range, the absorption usually leaves the molecule with a sufficient energy to fragment. However, this is usually not the case in the IR range.

Thus, infrared photodissociation spectroscopy (IRPD)¹¹⁶ is carried out with the use of helium tagging. The tagging relies on a creation of weakly bound complexes of the ions of interest with helium (the binding energy is usually below 0.3 kcal mol⁻¹). This is facilitated in the 3 Kelvin in trap of the ISORI instrument,¹⁶³ depicted in Figure 20 that was used for these measurements.¹⁶⁴ The ISORI instrument itself is a modified TSQ 7000 instrument. After the first quadrupole, there is a quadrupole bender, transfer octopole and a cryogenic wire quadrupole ion trap. The ions are mass-selected by the first quadrupole and guided through the bender and octopole to the ion trap. The ion trap is attached to second stage of a Sumitomo RDK-101E cold head capable of reaching <3 K temperature, which operates with 1 Hz frequency derived from 50 Hz electric power grid frequency. The ions are trapped with helium gas introduced to the ion trap through a piezo valve. The collisions with the helium atoms cool the ions and finally lead to the formation of the helium complexes in around 1 % yield ($M^{n+} + m \text{ He} \rightarrow [(M)\text{He}_m]^{n+}$). After the helium complexes are formed, the ion bender potential is switched so that no more ions enter the trap. In addition to helium complexes, nitrogen and water complexes are also formed in the ion trap – the nitrogen and water are background impurities always present in the ion trap. After the helium is pumped out (100–200 ms), the contents of the trap are irradiated by IR light from our laser system described on page 33.

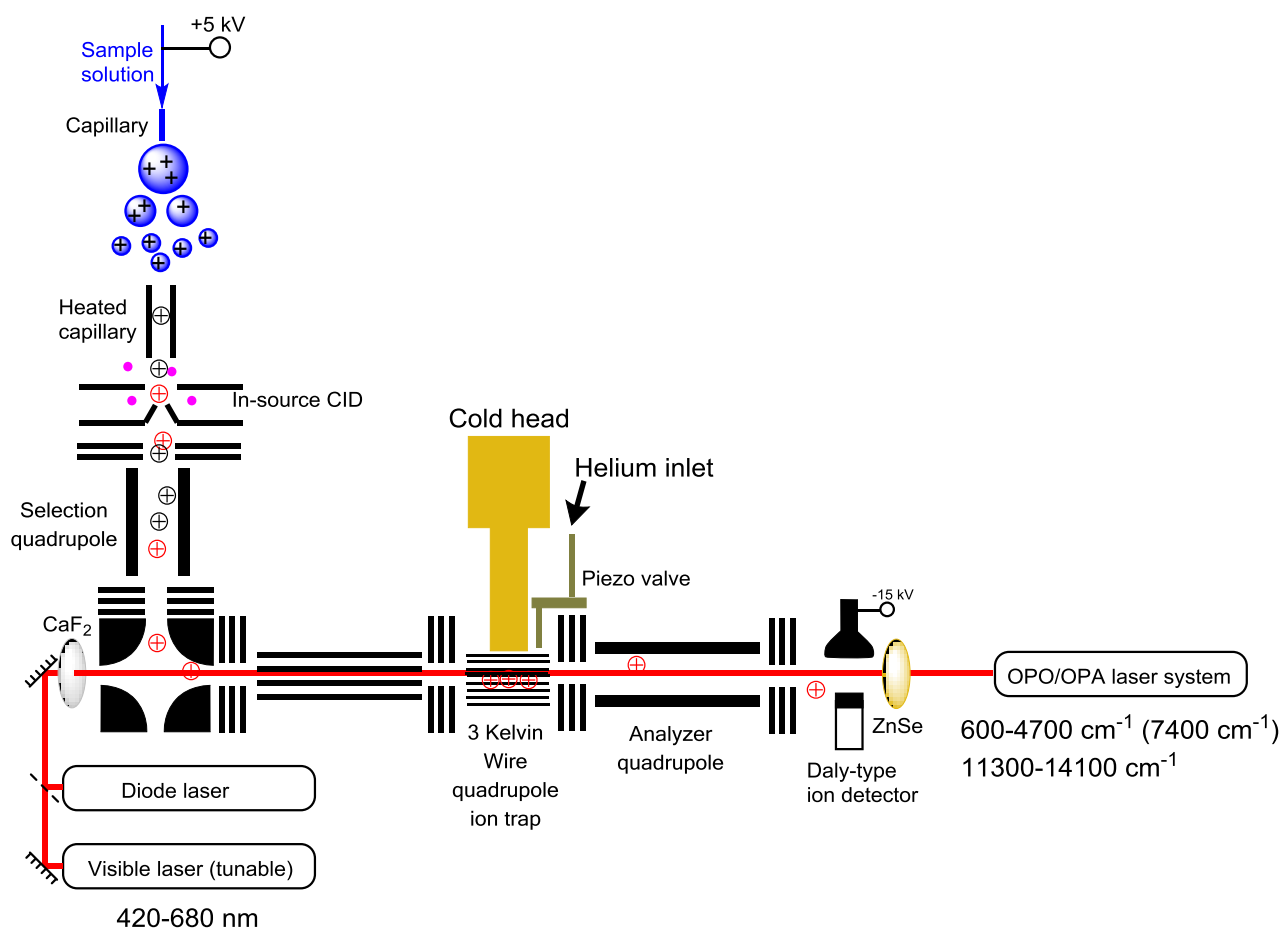


Figure 20. Schematic depiction of the ISORI instrument.

The absorption of an IR photon increases the internal energy of the helium complexes, which then lose helium atoms. The dissociation is a single-photon process because the binding energy of a helium tagging atom is very low (typically below $0.1 \text{ kcal mol}^{-1}$). The effect of a helium tagging atom on the spectra therefore is negligible, as previously discussed.¹²⁰ Finally, the ions are extracted from the trap by applying a negative (for positively charged ions) potential at the exit electrode of the ion trap, they are mass-analyzed by a quadrupole (which is in the case of IRPD experiment set to the mass of helium complexes) and counted by a Daly-type detector operating in ion counting mode (Maximum number of detectable ions is determined by the bandwidth of the pulse counter, which is 20 MHz. Due to the speed of extraction process, this is usually around 4000 ions.). By monitoring the number of the surviving helium complexes N_i as a function of the laser wavelength, we obtain the IR spectrum. To get the base number of helium complexes N_{i0} , a second cycle is carried out without the IR irradiation. With the typical trap filling period of 1

second, the laser system was scanned at $0.2\text{--}0.4\text{ cm}^{-1}\text{s}^{-1}$ and the laser irradiation took around 800 ms. This resulted in one point for each $0.4\text{--}0.8\text{ cm}^{-1}$ and the final IRPD spectrum is constructed as

$$\text{Attenuation}(\tilde{\nu}) = 1 - N_i(\tilde{\nu}) / N_{i0} \quad (6).$$

Alternatively, when the ions consist only of one absorbing species, we can plot the spectrum as

$$\text{Absorption}(\tilde{\nu}) = -\ln(N_i(\tilde{\nu}) / N_{i0}) \quad (7).$$

The timing sequence of the IRPD experiment is shown in the Figure 21. In some experiments, we prolonged the trap filling period to N seconds, which allowed for longer laser irradiation, and proportionately slowed down the laser scanning speed. The cycle length N has to be an integer, because the temperature in the trap changes with 1 s period due to the periodic operation of the cold head and this affects the number of helium complexes formed. The longer irradiation time proportionally increases the attenuation for weak spectral features and up to 10 times enhancements have been observed with 10 second operating period (9.8 s irradiation time). However, the decomposition of the helium complexes from the black body IR radiation limits the maximum ion storage time especially for singly charged ions.

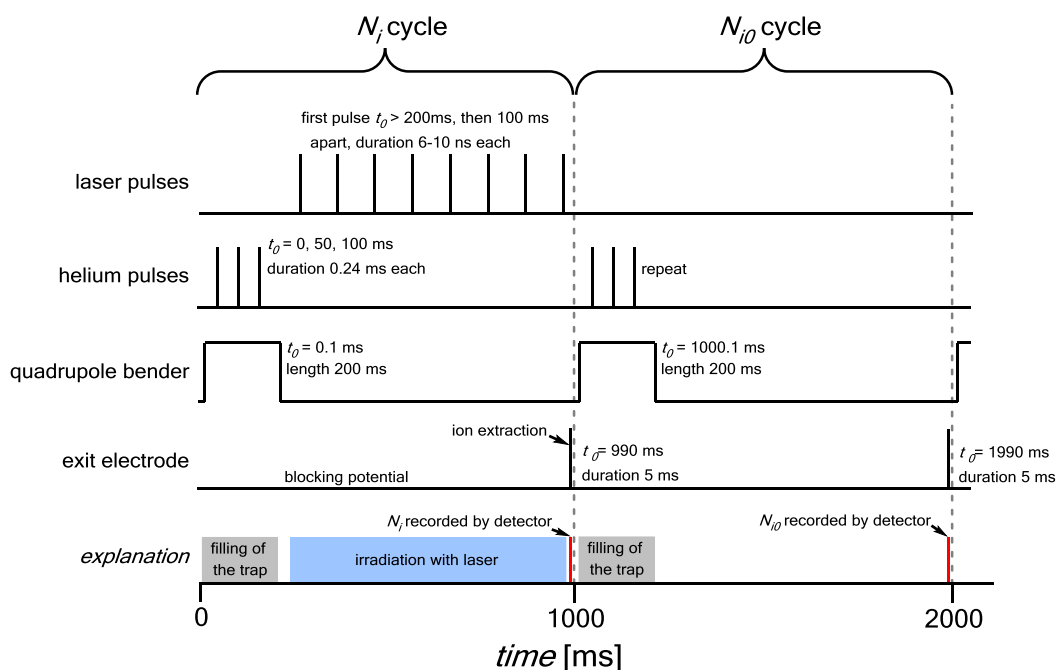


Figure 21. A typical timing sequence used for the acquisition of the IRPD spectra.

In two-color experiments, two laser beams with a different frequency were introduced into the trap.¹⁶⁴ One of the beams was tuned to a fixed frequency with wavenumber $\tilde{\nu}_2$ and the

other was scanned. The presence of the laser beam with the fixed frequency admitted into the trap in every cycle leads to dissociation of the helium complexes that absorb at that wavelength – therefore enriching the helium complexes mixture in non-absorbing species. The spectrum is then constructed in a similar way to single color experiments as

$$\text{Attenuation}(\tilde{\nu}) = 1 - N_i(\tilde{\nu}, \tilde{\nu}_2) / N_{i0}(\tilde{\nu}_2) \quad (8).$$

The measurement in the visible range is technically the same as in the IR range, except for the use of vis laser. Typical irradiation time with the vis laser was 720 ms (corresponding to 1 second overall cycle length) but was also shortened or lengthened, when necessary.

Light sources and frequency calibration. Infrared OPO/OPA laser system (LaserVision, USA) is capable to generate the IR light in the range of 600–7000 cm^{-1} in 10 nanosecond pulses and 10 Hz frequency (typical energy from 50 μJ at 600 cm^{-1} raising to 1 mJ above 1000 cm^{-1} , focus size around 1.5 mm at 50 % power, Figure 22). The typical FWHM of the spectral distribution of our laser system was 3 cm^{-1} without seeding the pumping Nd-YAG laser and was improved to 1 cm^{-1} by using a seeding diode laser.

The laser wavelength of the OPO/OPA system was measured with wavelength meter WS-600 from HighFinesse GmbH, which works by monitoring the visible output (signal) of the OPO stage of our laser system as the output frequency is a linear combination of this frequency and the stable frequency of the pumping Nd-YAG laser. Before the WS-600 wavelength meter was available, our frequency calibration method was based on monitoring the changes in the beam energy caused by the absorption of water and methane vapors. The wavenumber of the output IR light in our system ($\tilde{\nu}$) is determined as a frequency difference between two laser beams with their respective wavenumbers $\tilde{\nu}_{\text{pump}}$ and $\tilde{\nu}_{\text{signal}}$, related by the formulas $\tilde{\nu}_{\text{Nd-YAG pumping laser}} = \tilde{\nu}_{\text{pump}} + \tilde{\nu}_{\text{signal}}$ ($\tilde{\nu}_{\text{Nd-YAG pumping laser}} = 9396.686 \text{ cm}^{-1}$) and $\tilde{\nu} = \tilde{\nu}_{\text{pump}} - \tilde{\nu}_{\text{signal}}$. Therefore, the absorptions at both $\tilde{\nu}_{\text{pump}}$ and $\tilde{\nu}_{\text{signal}}$ must be taken into account (absorptions at $\tilde{\nu}$ are negligible). Figure 23 thus shows absorptions at both wavelength ranges and the corresponding dips in the measured pulse energy.

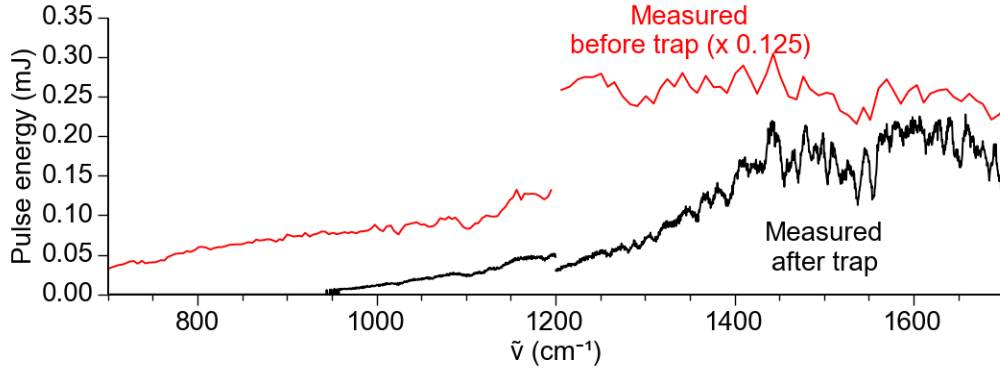


Figure 22. Dependence of laser pulse energy on wavelength for our OPO/OPA laser system. Lower intensity after the trap is caused by due to the divergent photon beam that is obscured by octopole entrance electrode and the exit window made of calcium fluoride that absorbs below 1400 cm^{-1} (the entrance windows is made of zinc selenide, that transmits most of the radiation in this spectral range).

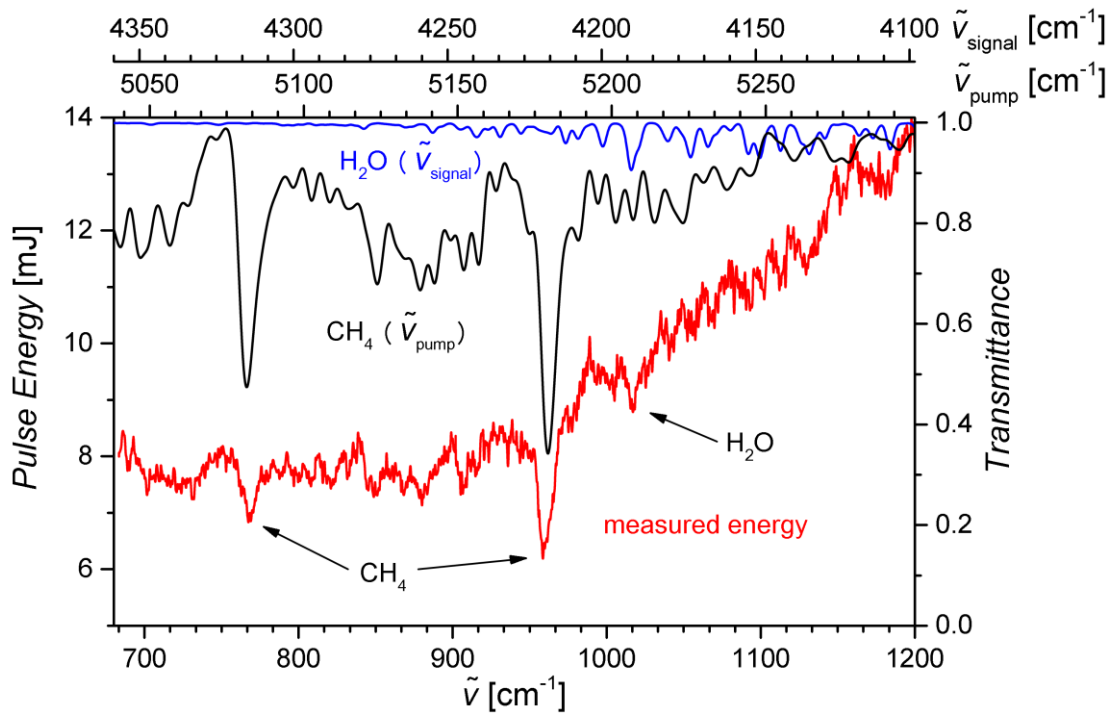


Figure 23. Wavenumber calibration of the OPO/OPA system. Positions of the methane and water absorption lines were taken from the HITRAN database.¹⁶⁵

The visible laser system for the visPD spectra measurement consists of supercontinuum NKT Photonics SuperK Extreme laser (78 MHz seed laser repetition rate), where appropriate wavelengths are selected by tunable acousto-optic filter (AOTF) SuperK Select (range 400–650 nm; spectral FWHM 1.8 nm at 400 nm, 8.5 nm at 650 nm). The laser

is focused in the trap from the other side of the ion trap than the IR laser (Figure 20), allowing simultaneous vis and IR irradiation. The focal size of the visible laser is 0.3 mm (50 % power). The power of the laser was measured by Thorlabs PM100A power meter equipped with Thorlabs S120C detector and is shown in Figure 24. The manufacturer gives the accuracy of the wavelength-selecting AOTF in the range of ± 0.2 nm of the nominal value over all wavelengths. We observed that in our setup the position of absorption maxima in measured spectra of the same species could differ by ~ 2 nm depending on the overlap of the laser beam and the ion cloud.

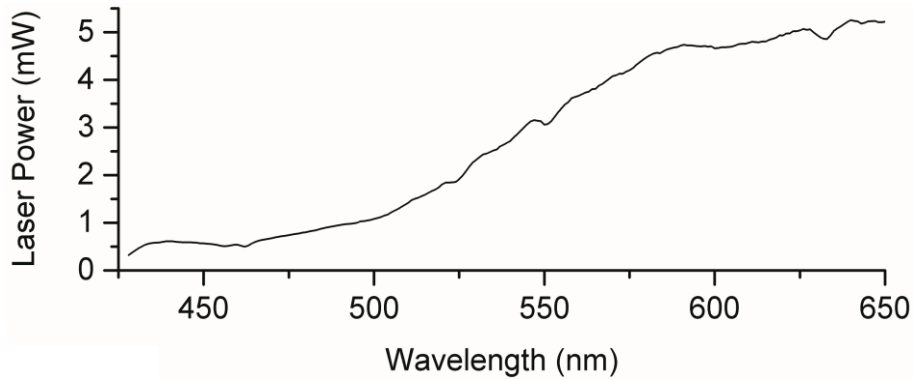


Figure 24. Power output of visible laser used in visPD measurements.

Post-processing of the acquired spectra. Because the IR laser scanning movement is irregular to some extent (this is not the case for vis measurement, where we can set the wavelength exactly), the acquired spectra were usually binned to the nearest integer wavenumber (of half wavenumber). The attenuation from multiple points with the same wavelength was calculated by first summing the corresponding ion counts and the calculation from the formula

$$\text{Attenuation}(\tilde{\nu}) = 1 - \Sigma N_i(\tilde{\nu}) / \Sigma N_{i0} \quad (9).$$

In some cases, where only one species absorbed, the logarithmic form was used

$$\text{Intensity}(\tilde{\nu}) = -\ln(\Sigma N_i(\tilde{\nu}) / \Sigma N_{i0}) \quad (10).$$

Where the absorption bands were wider than the laser energy fluctuations, which was the case in the vis region, the calculated *Attenuation* or *Intensity* was normalized to the laser pulse energy.

The acquired spectra were usually smoothed by a Savitzky-Golay filter (<11 points, 2nd or 3rd order polynomial).¹⁶⁶

2.6. Theoretical Calculations

DFT calculations. In this thesis, I calculated the molecular properties using density functional theory. The software that I used for the calculations was Gaussian 09¹⁶⁷ with its implementations of DFT functionals: M06, M06-2X,¹⁶⁸ PBE,¹⁶⁹ OLYP,^{170,171,172} B3LYP,^{173–176} M06L and B97D3. These functionals were combined with Grimme's empirical dispersion correction with Becke-Johnson damping¹⁷⁸ and with zero damping.¹⁷⁹ Pople's 6-31G^{180–189} (including diffuse functions¹⁹⁰), 6-311G^{191–195} and Ahlrich's TZVP^{196,197} and def2-TZVP¹⁹⁸ basis sets were used. In some complexes containing triflate and perchlorate anions, I used a specially constructed basis set with 6-311++G** (or 6-311+G** without any loss of accuracy) basis functions, extended by pc-3^{199–202} basis functions on S and Cl atoms. I also extended the basis functions by the pc-3 basis set on the carbon atoms in the CF₃ groups. These additional basis functions were, however, only included in the complexes, where I analyzed the IR stretches of these counterions. In those cases, the combined basis set is abbreviated as BS1.

The optimized structures were checked to be minima on the potential energy surface by calculating the Hessian and checking for imaginary vibrational frequencies. This also served to predict IR spectra that were the most important calculated properties in this work. However, the calculated IR spectra needed to be frequency-scaled to account for the anharmonicity of the PES. Therefore, I used either fixed scaling factors (most commonly 0.99 for B3LYP-D3/6-311+G** functional/basis set in the range below 1200 cm⁻¹) or, in some cases, wavenumber-linear frequency scaling.²⁰³ The scaling factors in other cases were usually determined on basis of the skeletal organic ligand vibrations. All presented IR spectra were convoluted with Gaussian function with FWHM 5 cm⁻¹. Vibrational frequency scaling was not used for the calculation of zero-point vibrational energies

The complexes investigated in this study have significant multireference character. Because DFT in its standard formulation uses a single determinant wave function, the description of these systems by DFT is not theoretically correct. Therefore I relied mostly on the observation of trends rather than actual values.

For the predictions of the vis spectra, I used Time-Dependent DFT (TD-DFT) as implemented in Gaussian 09.

CASSCF^{204,205}/**CASPT2**^{206–209} **calculations** were all carried out by our collaborator Martin Srnec with the MOLCAS 8.0.²¹⁰ ANO-RCC basis set was used for all atoms, contracted to [6s5p3d2f1g] for Fe, [4s3p2d] for the ligating O, N atoms, [3s2p] for other N, O, F and C

atoms, [4s3p] for Cl and S atoms, and [2s] for H atoms. DKH2 one-electron spinless Hamiltonian was used in all calculations to account for spin-free relativistic effects.²¹¹⁻²¹³ CASSCF energies were calculated at the B3LYP-optimized geometries with 12-electrons-in-9-orbitals active space. The active space included five $3d_{Fe}$ orbitals, three $2p_{oxo}$ orbitals and one chelate-based orbital. To improve the accuracy of the calculations, the CASPT2 energies were used on the diagonal of the two-component Hamiltonian matrix. Additionally, a level shift of 5 a. u. was used in the CASSCF calculations to aid convergence. Similarly, in CASPT2 calculations, an imaginary level shift of $i0.2$ a. u. was used to eliminate intruder states^{214,215} and no orbitals were frozen.

CHAPTER 3. Iron(IV)-Oxo Complexes in the Gas Phase

This chapter is based on publications (1) and (2) as referenced in Prohlášení (Declaration) on page i.

3.1. Introduction

My first goal in the study of high-valent iron-oxo species was to demonstrate that IRPD spectroscopy can be used for their characterization in the gas phase. To that end we designed a study, where we acquired IRPD spectra and gas-phase reactivity of different iron(IV)-oxo compounds (Figure 11). The unique advantage of ion spectroscopy for analysis of these compounds is the ability to mass-select different species present in solution. For example, solution prepared by oxidation of $[(\text{TMC})\text{Fe}^{\text{II}}(\text{OTf})_2]$ contains both complexes $[(\text{TMC})\text{Fe}^{\text{IV}}(\text{O})(\text{CH}_3\text{CN})]^{2+}$ (**1**) and $[(\text{TMC})\text{Fe}^{\text{IV}}(\text{O})(\text{OTf})]^+$ (**2**). Because complexes **1** and **2** differ in their m/z ratio, it is very simple to study them separately using the ion spectroscopy, without the need of their prior separation in solution (which is virtually impossible). To cover different bonding arrangements, I studied complexes of iron with three different amine/aminopyridine ligands – tetradentate TMC, whose free sites are *trans* to each other, pentadentate N4Py, and tetradentate PyTACN, whose free sites are in *cis* position. These different ligands enabled me to observe the effect of anionic ligand variation in different positions to the oxo unit. Assignment of vibrational bands as the Fe=O stretching modes is based on the ^{18}O labeling, which has been achieved by the oxygen atom exchange with H_2^{18}O .^{216,217}

3.2. Fe=O Stretching Frequencies

IRPD spectrum of complex **1** is shown in Figure 26. The Fe=O stretching vibration is located at 848 cm^{-1} and shifts to 812 cm^{-1} upon ^{18}O labeling (Figure 26a,b), which is consistent with the Hooke's law for diatomic Fe=O oscillator (from $\tilde{\nu} = (k/\mu)^{1/2}$ and $\mu = m_{\text{Fe}} m_{\text{O}} / (m_{\text{Fe}} + m_{\text{O}})$) follows that $\tilde{\nu}_{\text{Fe}^{18}\text{O}} / \tilde{\nu}_{\text{Fe}^{16}\text{O}} = (\mu_{\text{Fe}^{16}\text{O}} / \mu_{\text{Fe}^{18}\text{O}})^{1/2} = 0.956$; $848\text{ cm}^{-1} \times 0.956 = 811\text{ cm}^{-1}$). I also verified the identity of this iron compound by comparing the acquired IRPD spectrum with DFT predictions. I used the B3LYP functional, because it outperforms other functionals in the predictions of IR spectra.^{123,218-225} Theoretical spectrum calculated with the B3LYP/6-311+G* method (Figure 26c), employing a frequency scaling factor of 0.99 provides an excellent prediction of the vibrational fingerprint region of the TMC ligand, when we assume

that the complex **1** is in the triplet state, which is the ground state both in solution,⁴⁵ and that the oxo group is in *anti* position relative to the TMC methyl groups. On the other hand, the predicted Fe=O stretching frequency was blue-shifted by 66 cm⁻¹. To see if other DFT functionals can perform better with regards to the Fe=O frequency, I tested several of them and found that most of them gave worse agreement, with the exception of M06L that gave only slightly worse description of ligand vibrations and a better estimate of the Fe=O frequency (I did the screening on the TMC ligand, Figure 27, and on the PyTACN ligand, Figure 33). However, because the Fe=O frequency can be assigned directly from the spectra, I decided to use B3LYP for all systems, because of its better description of ligand vibrations.

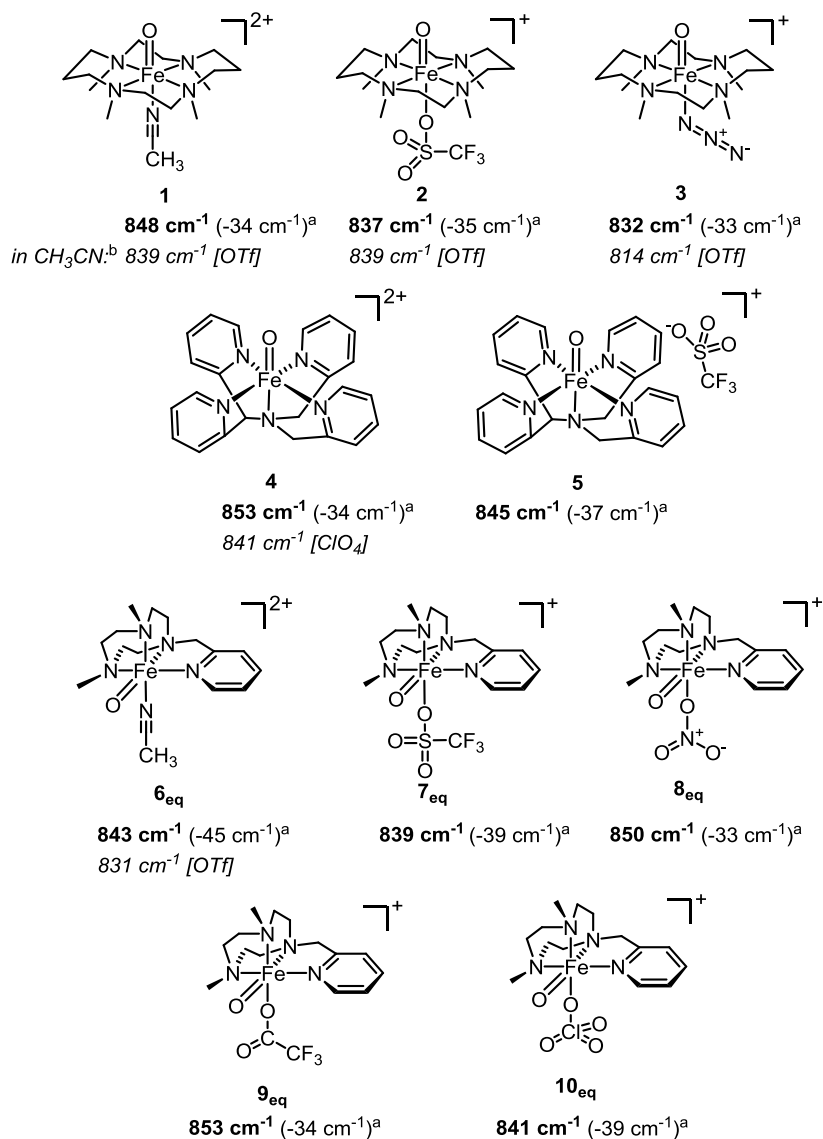


Figure 25. Studied iron(IV)-oxo complexes and their determined Fe=O stretching frequencies (in bold). Values from previous studies in solution are in parentheses. Present counter ions are given in brackets. ^aSpectral shift upon ¹⁸O labeling. ^bFrequencies of the complexes measured in acetonitrile solution by resonance Raman spectroscopy^{65,66} are printed in italics.

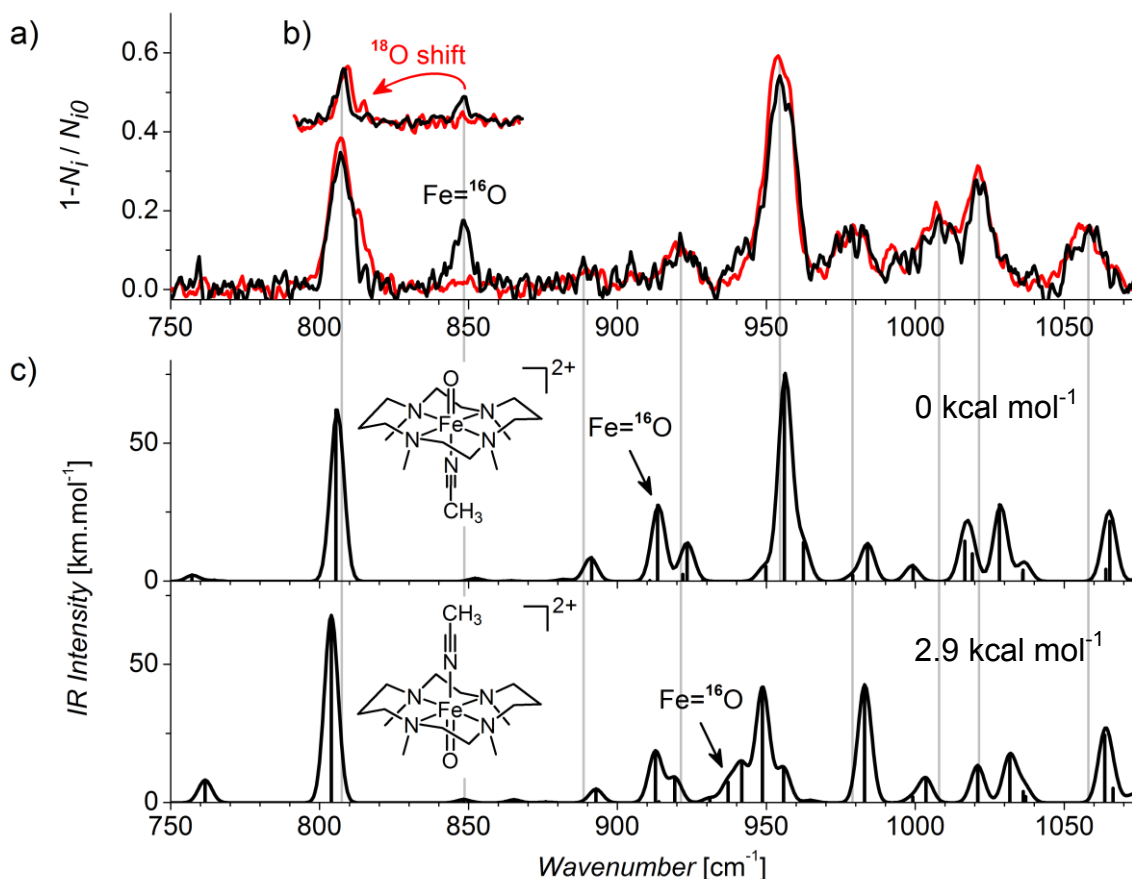


Figure 26. (a) Helium tagging IRPD spectrum of the $[(\text{TMC})\text{Fe}^{\text{IV}}(\text{O})(\text{CH}_3\text{CN})]^{2+}$ (**1**); (b) the spectral range with $\text{Fe}=\text{}^{16}\text{O}$ and $\text{Fe}=\text{}^{18}\text{O}$ stretching vibrations measured with a seeded laser; (c) B3LYP-D3/6-311+G* theoretical IR spectrum of $[(\text{TMC})\text{Fe}^{\text{IV}}(\text{O})(\text{CH}_3\text{CN})]^{2+}$ isomers in the triplet state (frequency scaling factor is 0.99). Shown energies are relative enthalpies at 0 K calculated at the same level as the IR spectra.

IR spectrum of complex **2**, containing triflate ligand instead of acetonitrile, is shown in Figure 28. It shows the $\text{Fe}=\text{O}$ stretching vibration at 837 cm^{-1} . The shift of the $\text{Fe}=\text{O}$ stretching vibration by -35 cm^{-1} with the ^{18}O labeling is consistent with iron(IV)-oxo species. The value of 837 cm^{-1} is an 11 cm^{-1} red shift with respect to **1**. Even though the DFT predictions are mostly correct for the vibrations of the sulfonyl group in triflate, the vibrations of trifluoromethyl group are red shifted by $\sim 50 \text{ cm}^{-1}$. We also measured azide-containing complex **3** (Figure 29) and obtained $\text{Fe}=\text{O}$ stretching frequency of 832 cm^{-1} . By comparison of the $\text{Fe}=\text{O}$ frequencies in **1–3**, we can see that the frequency of the $\text{Fe}=\text{O}$ stretch is only mildly sensitive to the ligand in the *trans* position with respect to the oxo unit of the $\text{Fe}=\text{O}$ group.

IR spectra of complexes **4** and **5** with the pentadentate ligand N4Py are shown in Figures 30 and 31. I considered various coordination modes of the triflate anion and found a satisfactory agreement with the spectra for the uncoordinated version, where the triflate is not bound to the iron center and is only attached by ion-ion interaction. The difference in coordination is also obvious when comparing it with the complex **2** – in that case the various intense S–O vibration modes span from 1010 to 1350 cm^{-1} . However, in the case of complex **5**, they span from 1020 to 1280 cm^{-1} , indicating a binding mode with less asymmetric binding of the three oxygen atoms in the triflate unit. The reasoning is also supported by data shown in Figure 31. We can see that when the OTf anion is coordinated to the iron, we get very similar triflate vibrations as observed in complex **2**.

The Fe=O stretching frequency is red shifted in **5** by 8 cm^{-1} with respect to **4** (845 vs 853 cm^{-1}) and, similarly to the complexes with TMC ligand, this small shift does not indicate any substantial change in the Fe=O bonding.

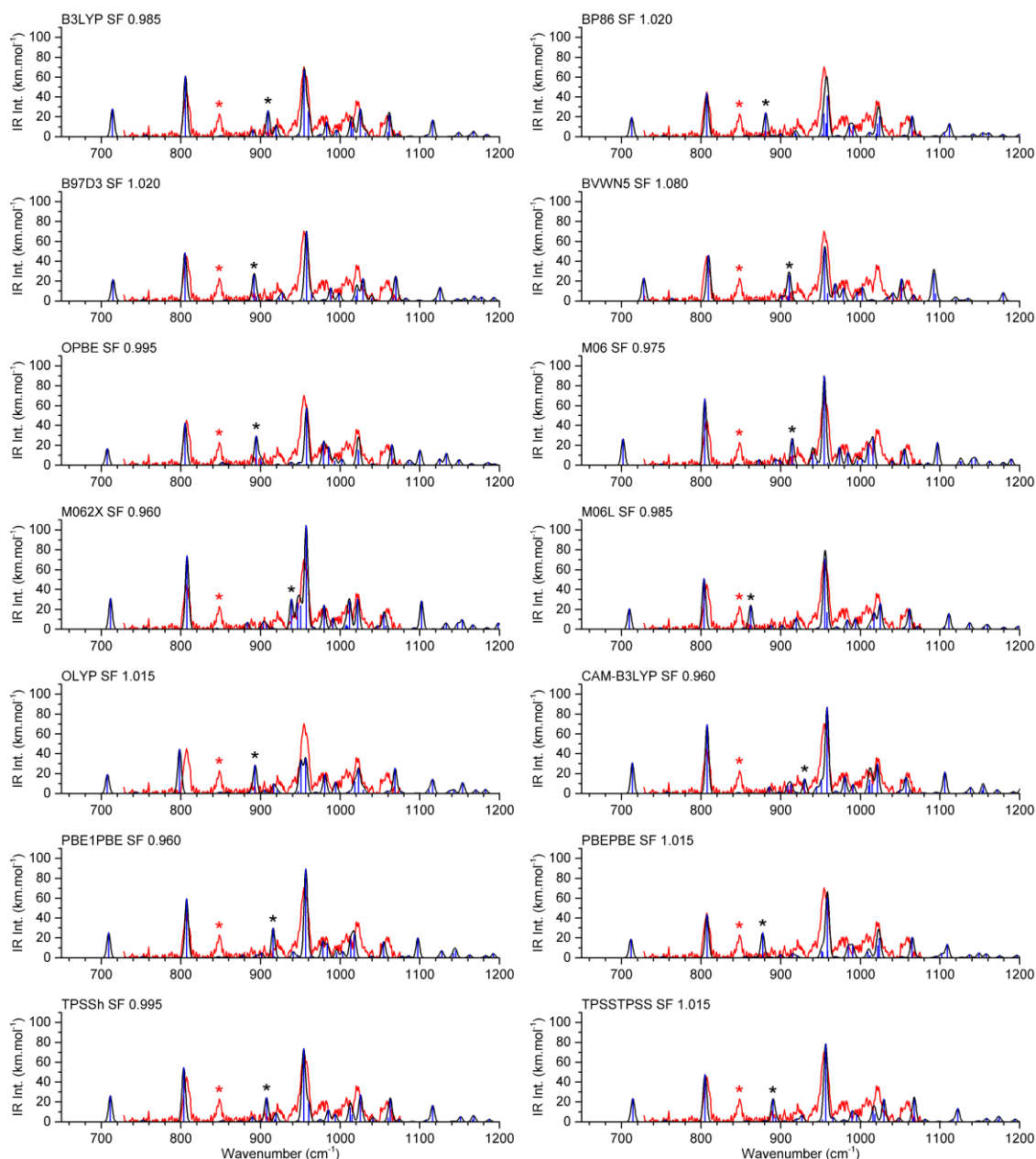


Figure 27. Comparison of experimental (red) and calculated (black, blue) spectra of **1** with various DFT functionals with 6-311+G** basis set. Scaling factor is given in each graph and was chosen to maximize the overlap between theory and experiment (defined as the sum of product of two spectra $\Sigma(\text{Attenuation}_{\text{Exp}}(\tilde{\nu}) \times \text{Intensity}_{\text{Calc}}(\tilde{\nu}))$). Grimme's dispersion correction with Becke-Johnson damping¹⁷⁸ was included in cases of B3LYP, B97D3, PBE0 (labeled PBE1PBE), PBE (labeled PBEPBE), CAM-B3LYP and BP86. The older undamped version¹⁷⁹ was used with M06, M06-2X and M06L.

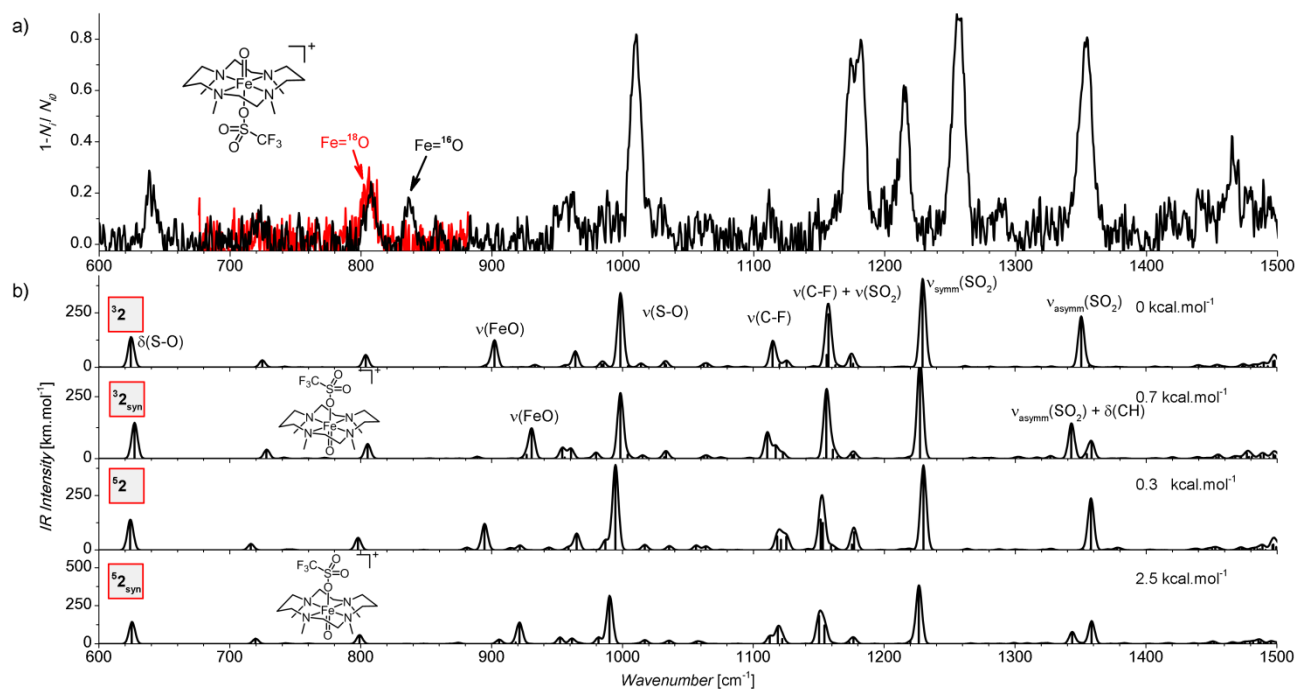


Figure 28. Comparison of (a) experimental and (b) calculated spectra of $[(\text{TMC})\text{Fe}^{\text{IV}}(\text{O})(\text{OTf})]^+$ (2). IR spectra were calculated at B3LYP-D3/BS1 level and IR frequencies were scaled by 0.99. Energies given are relative energies at 0 K calculated at the same level of theory.

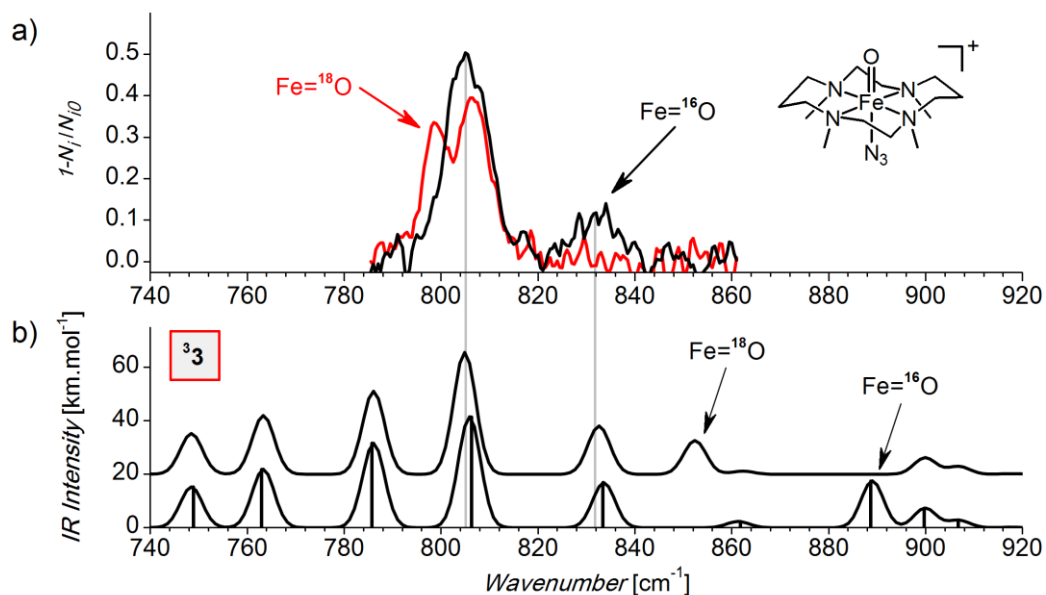


Figure 29. Comparison of (a) experimental and (b) calculated (B3LYP-D3/6-311+G**) spectra of 3. IR spectra were calculated at B3LYP-D3/6-311+G** level and IR frequencies were scaled by 0.99.

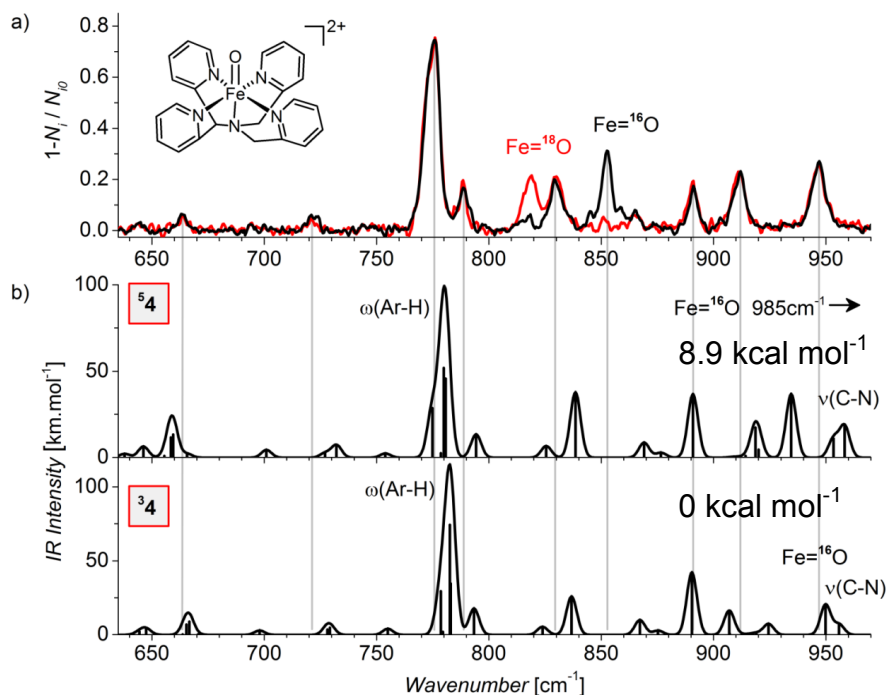


Figure 30. Comparison of (a) experimental and (b) calculated spectra of **4**. IR spectra were calculated at B3LYP-D3/6-311+G** level and IR frequencies were scaled by 0.99. Energies given are relative energies at 0 K calculated at the same level of theory.

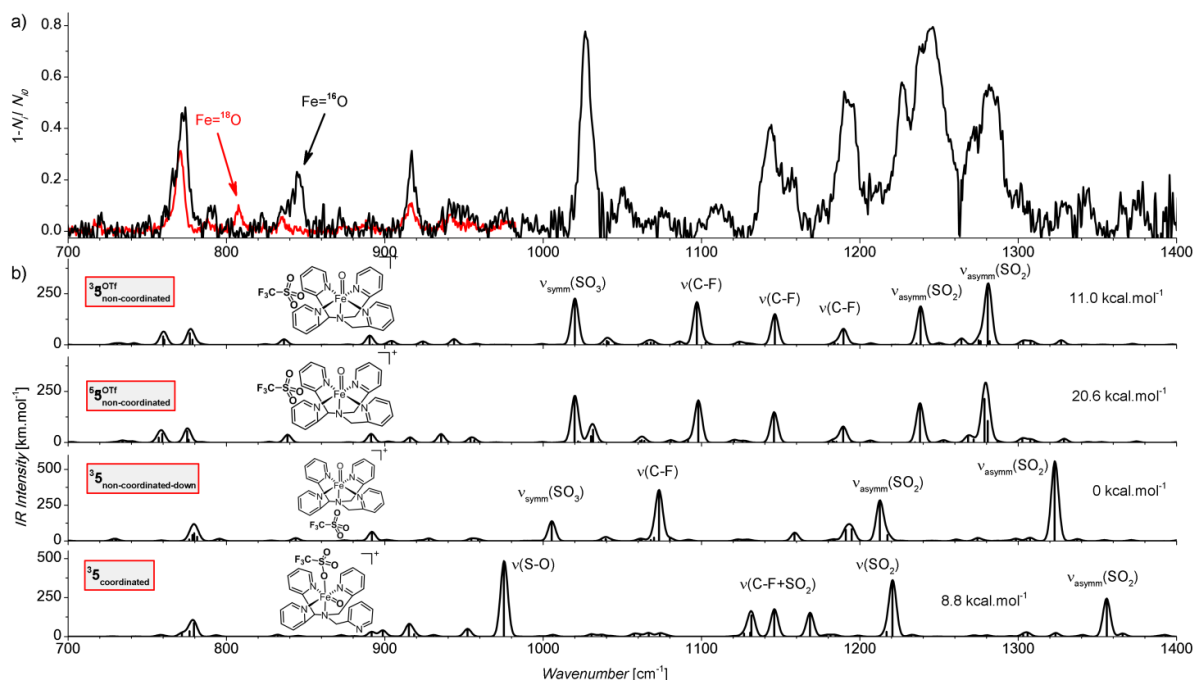


Figure 31. Comparison of (a) experimental and (b) calculated spectra of $[(\text{N4Py})\text{Fe}^{\text{IV}}(\text{O})(\text{OTf})]^+$ (**5**). IR spectra were calculated at B3LYP-D3/BS1 level and IR frequencies were scaled by 0.99. Energies given are relative energies at 0 K calculated at the same level of theory.

Complexes with the PyTACN ligand allowed us to study the influence of the exchange of ligand in *cis* position to the oxo group. Oxidation of $[(\text{PyTACN})\text{Fe}^{\text{II}}(\text{OTf})_2]$ by peracetic acid in acetonitrile yielded the dicationic complex $[(\text{PyTACN})\text{Fe}^{\text{IV}}(\text{O})(\text{CH}_3\text{CN})]^{2+}$ (**6**; Figure 32; see also Figure 33 for the assessment of DFT functionals) and the monocationic complex $[(\text{PyTACN})\text{Fe}^{\text{IV}}(\text{O})(\text{OTf})]^+$ (**7**; Figure 34). The Fe=O stretching vibrations in complexes **6** and **7** are located at 843 and 839 cm^{-1} , respectively. This is similar to all other studied iron(IV)-oxo complexes. The triflate stretching vibrations in **7** span even larger range than in the case of **2**. Specifically, the S–O vibration is shifted to 960 cm^{-1} from 1010 cm^{-1} in **2**. The S=O vibrations, on the other hand do not seem to be affected as much and stay around 1350 cm^{-1} . By addition of the appropriate anion into the solution of iron(IV)-oxo complexes **6** and **7**, I also generated complexes with different ligand (NO_3 , CF_3COO , ClO_4 ; **8**, **9**, **10**; shown in Figures 35, 36, and 37). As in the previous cases, coordination of the triflate or perchlorate cause slight red shifts (by 4 cm^{-1} and 2 cm^{-1}) in the Fe=O stretching frequencies. However, coordination of nitrate and trifluoroacetate cause blue shifts of 7 and 10 cm^{-1} , respectively.

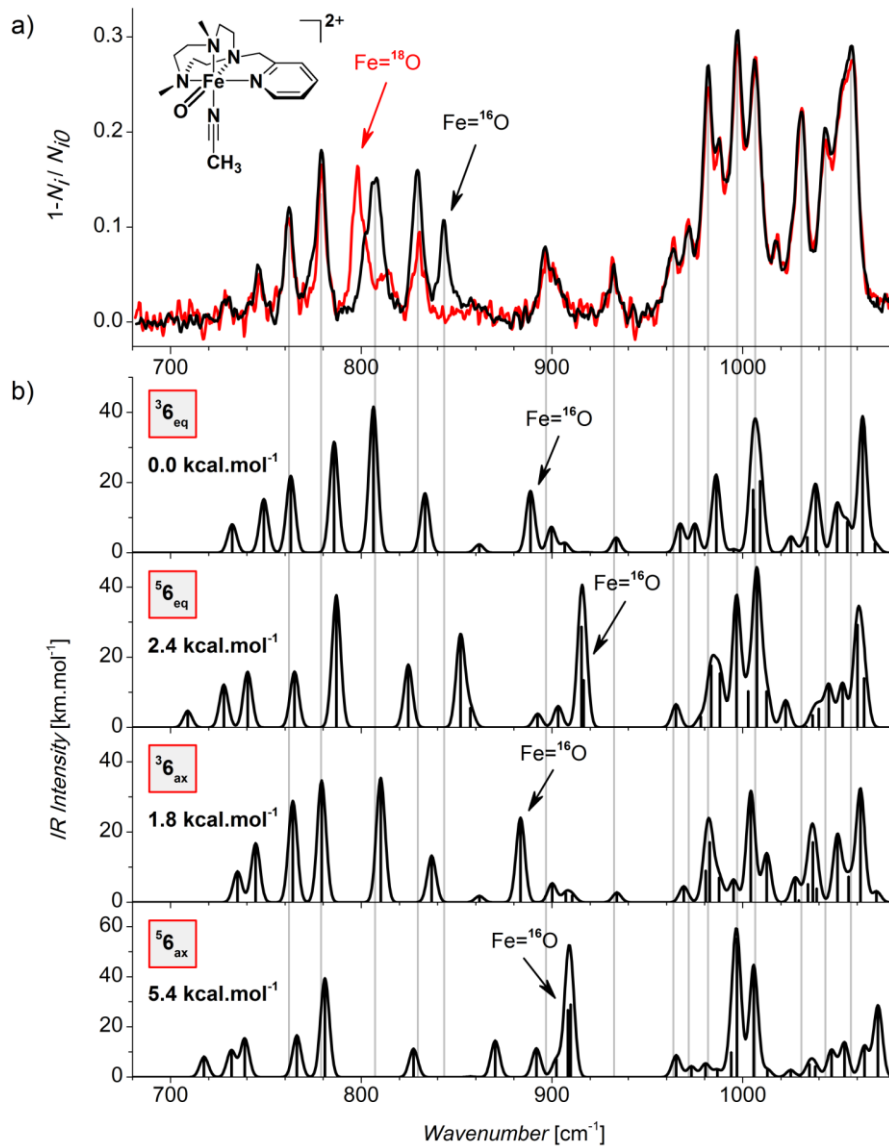


Figure 32. Comparison of (a) experimental and (b) calculated spectra of **6**. IR spectra were calculated at B3LYP-D3/6-311++G** level and IR frequencies were scaled by 0.99. Energies given are relative energies at 0 K calculated at the same level of theory.

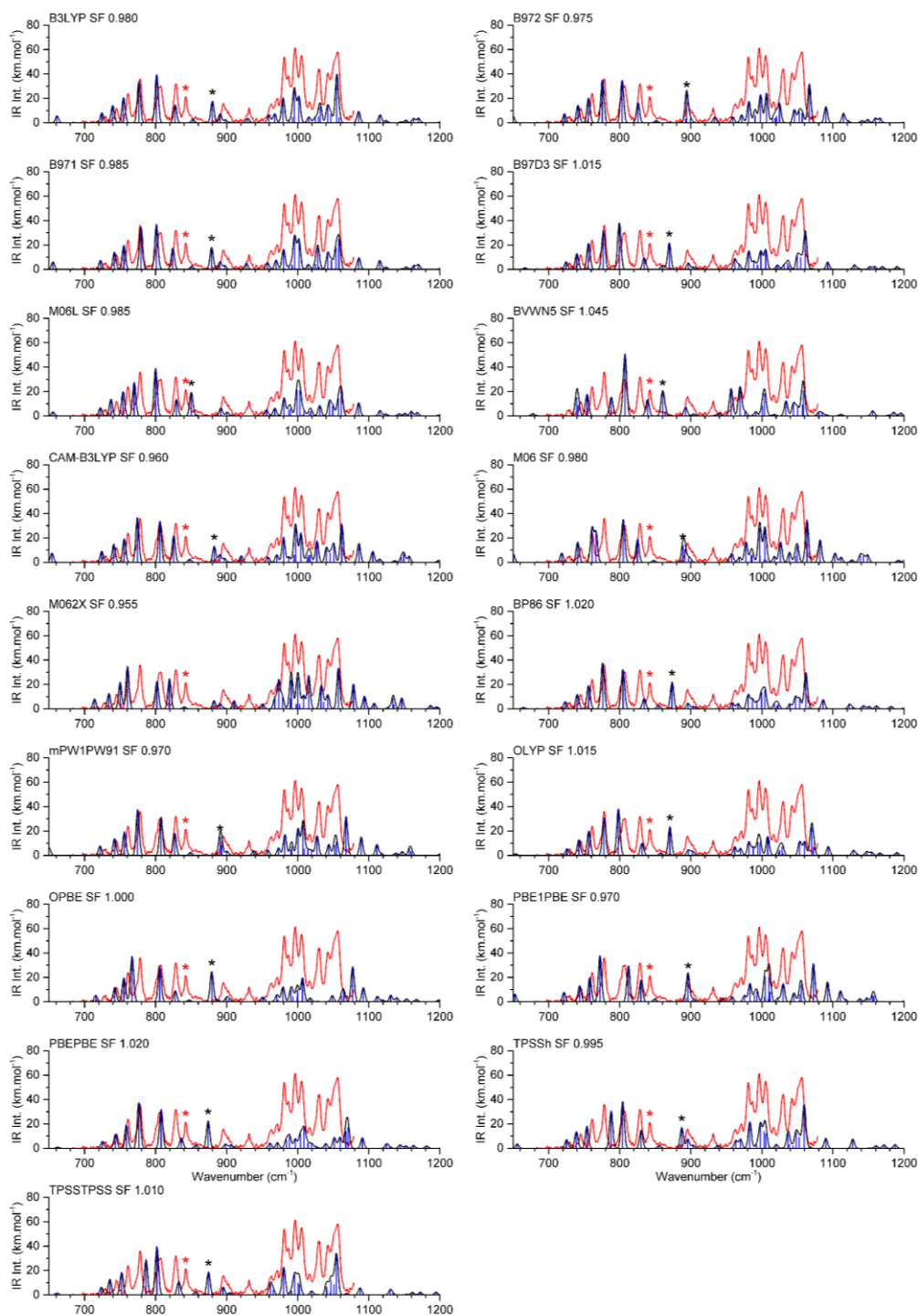


Figure 33. Comparison of experimental (red) and calculated (black, blue) spectra of **6** with various DFT functionals with 6-311+G** basis set. Scaling factor is given in each graph and was chosen to maximize the overlap between theory and experiment (defined as the sum of product of two spectra, see caption of Figure 27). For B3LYP, B97D3, PBE0 (labeled PBE1PBE), PBE (labeled PBE1PBE), CAM-B3LYP and BP86 Grimme's dispersion correction with Becke-Johnson damping¹⁷⁸ was used. The older undamped version¹⁷⁹ was used for M06, M06-2X and M06L.

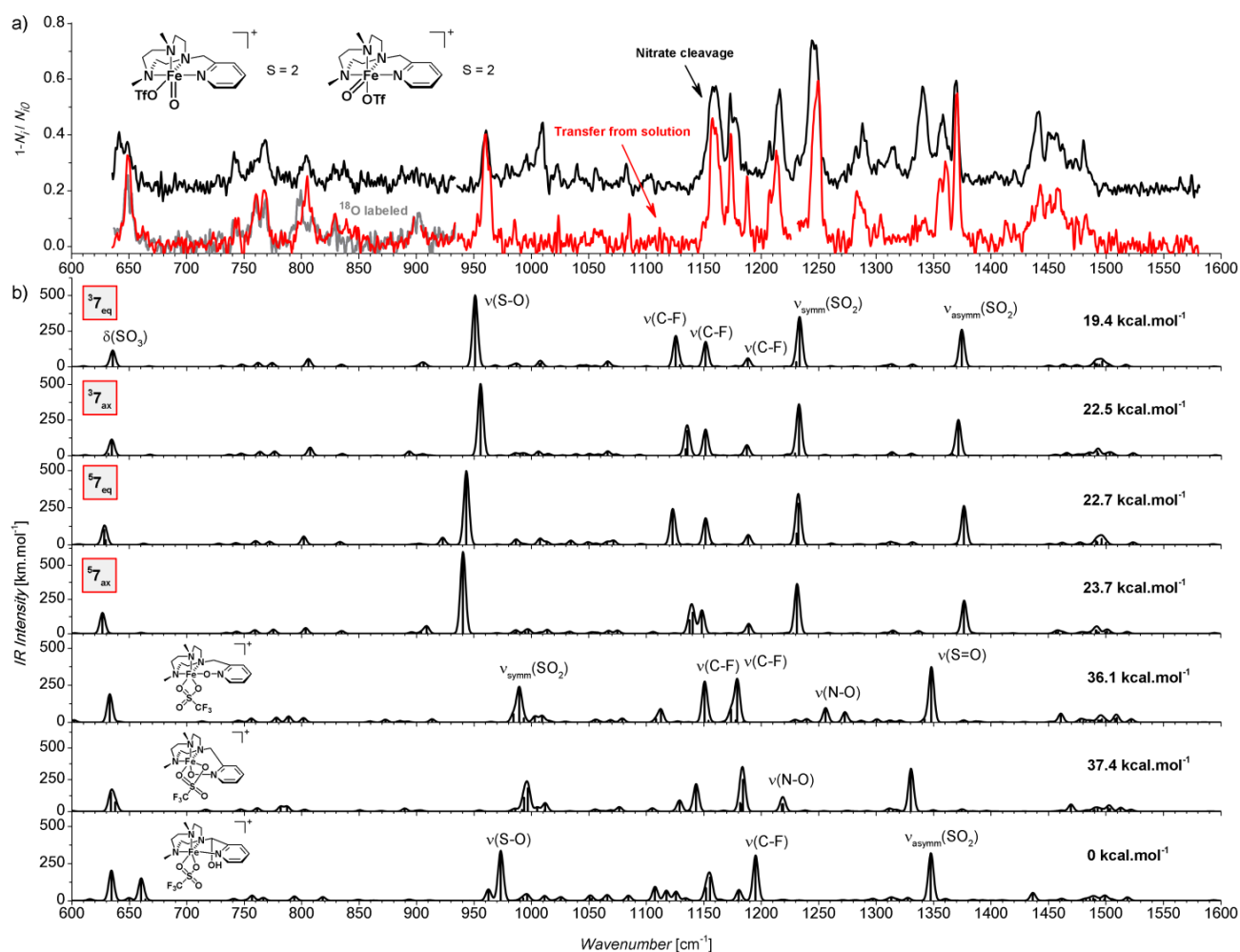


Figure 34. Comparison of (a) experimental and (b) calculated spectra of **7**. The complexes with the oxidized ligand (last three panels) are in the quintet state. IR spectra were calculated at B3LYP-D3/BS1 level and IR frequencies were scaled by 0.99. Energies given are relative energies at 0 K calculated at the same level of theory as the spectra (see also Table 3 for CASPT2 energies). The last three oxidized structures in (b) are in quintet state.

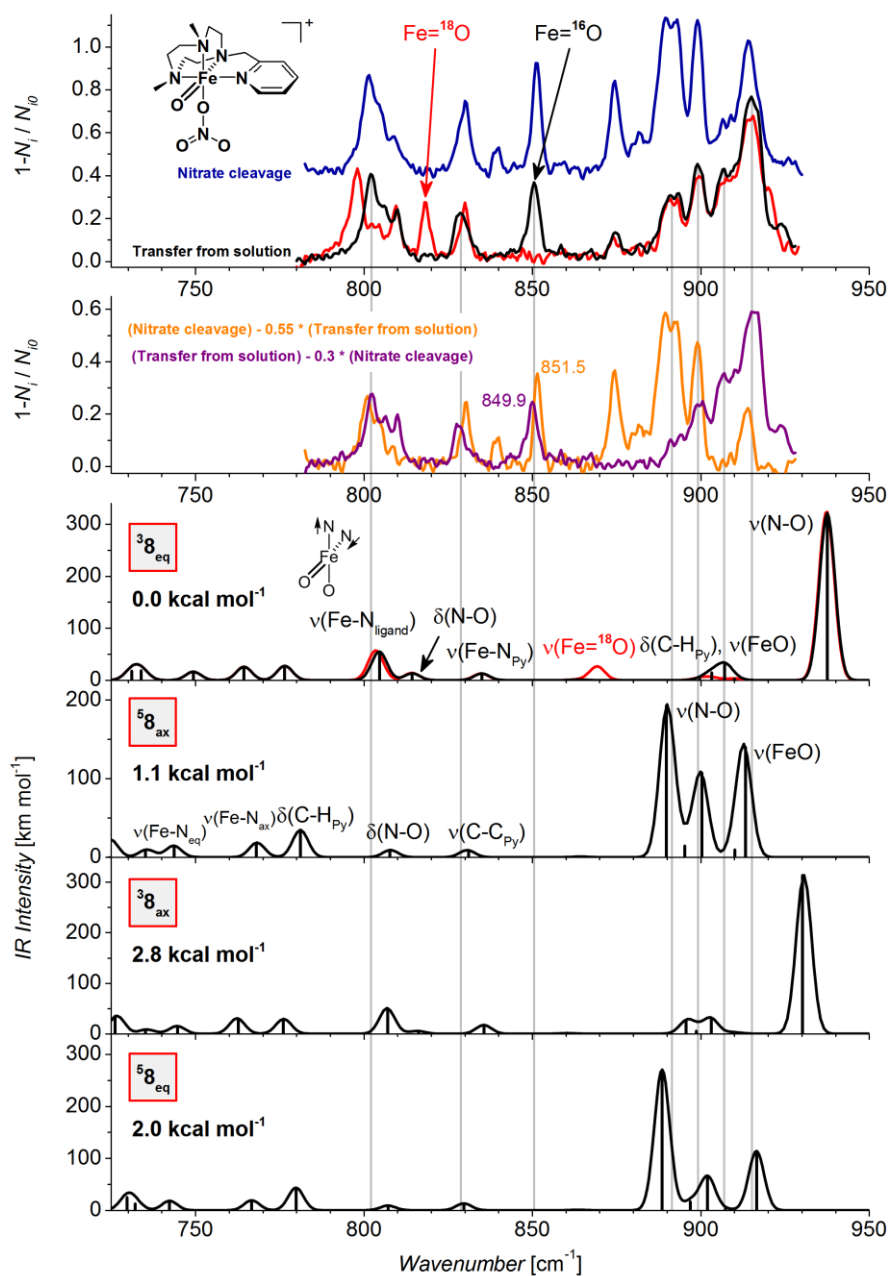


Figure 35. Comparison of (a) experimental and (b) calculated spectra of **8**. IR spectra were calculated at B3LYP-D3/6-311+G** level and IR frequencies were scaled by 0.99. Energies given are relative energies at 0 K calculated by the CASPT2 method (see also Table 3).

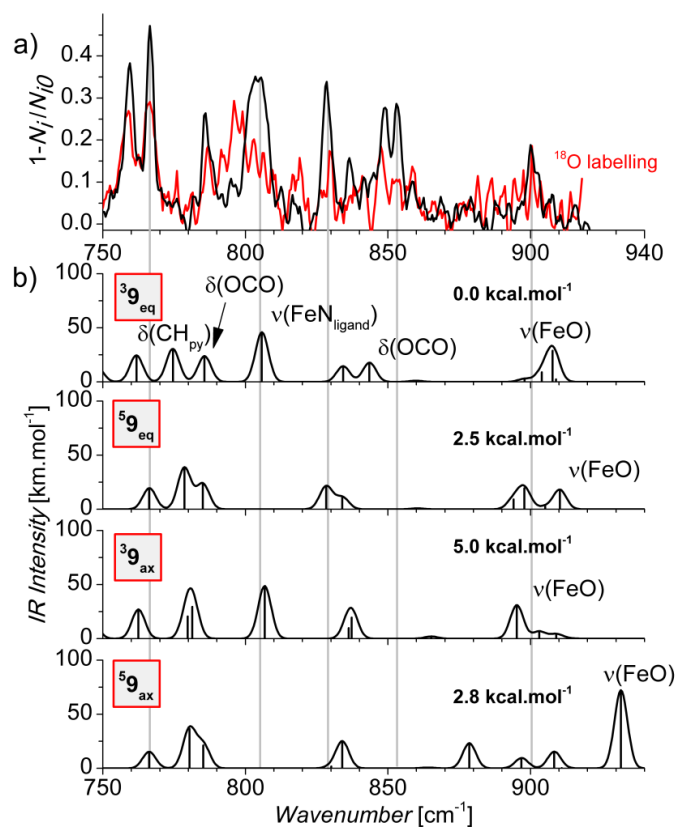


Figure 36. Comparison of (a) experimental and (b) calculated spectra of **9**. IR spectra were calculated at B3LYP-D3/BS1 level and IR frequencies were scaled by 0.99. Energies given are relative energies at 0 K calculated by the CASPT2 method (see Table 3).

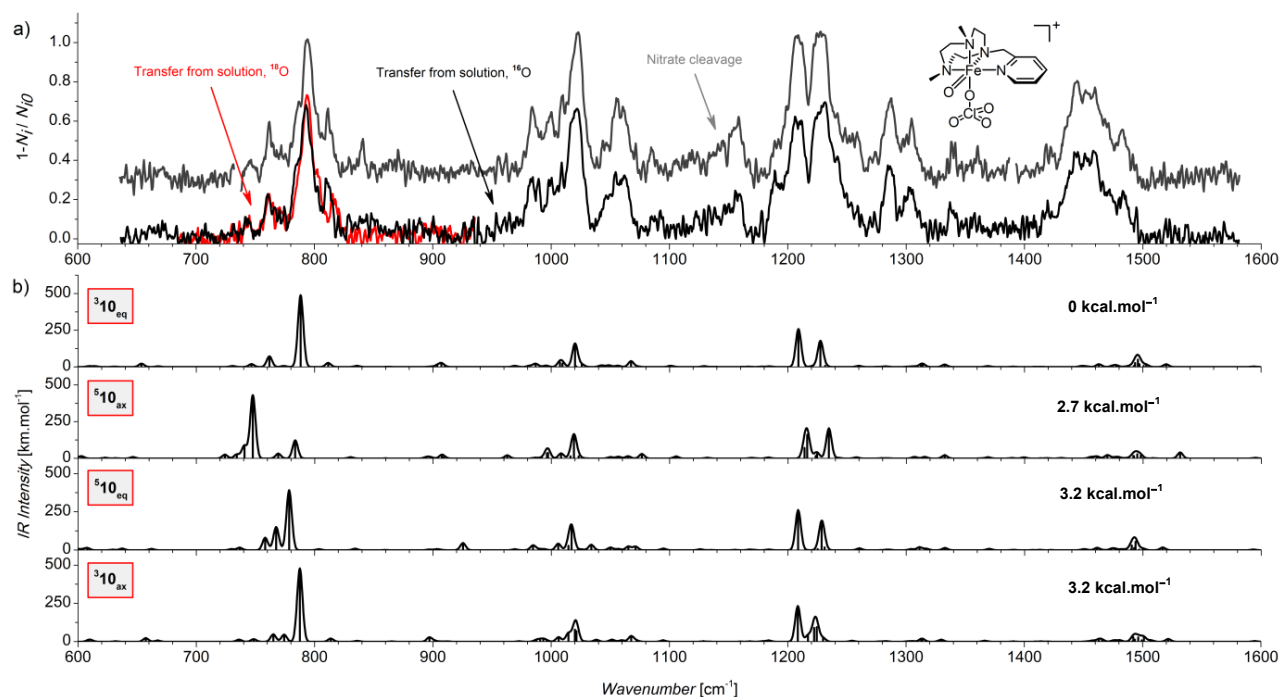


Figure 37. Comparison of experimental and calculated spectra of **10**. Experimental conditions are described in section 2.3. Energies given are relative energies at 0 K calculated by the CASPT2 method (see Table 3).

With the Fe=O stretching frequencies in hand, we were able to compare the previously reported resonance Raman and IR data with data obtained by IRPD spectroscopy. This comparison was necessary to establish the utility of this method as an alternative characterization method for these complexes. The change reflects combined effects of the solvation and the presence of negatively charged counter ions in the solution. The gas-phase values are in average 9 cm^{-1} blue-shifted (Figure 38). The shift is comparable (11 cm^{-1}) also if we assume that only the dications are present in solution. On the other hand, solution values are quite similar to the values obtained for singly charged complexes, with the exception of complex **3**, $[(\text{TMC})\text{Fe}^{\text{IV}}(\text{O})(\text{N}_3)]^+$, whose Fe=O frequency in the gas phase is 18 cm^{-1} higher than in solution.

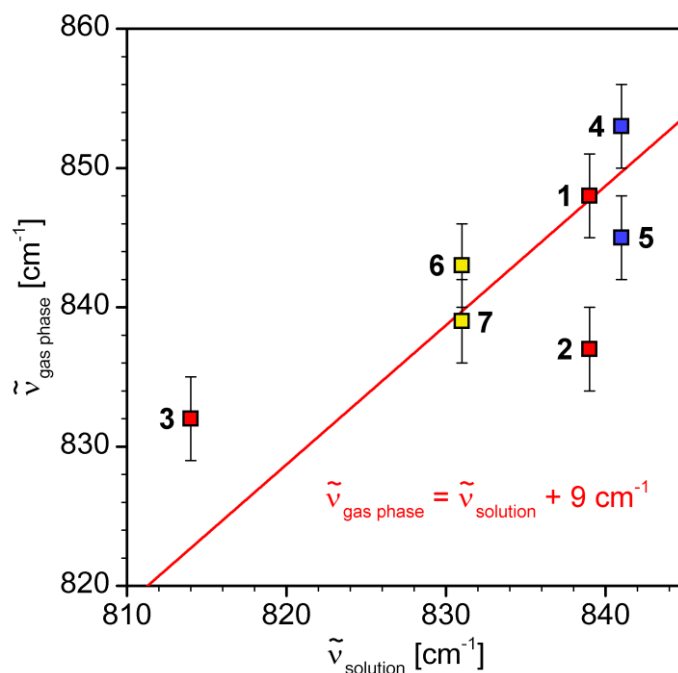
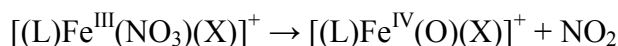


Figure 38. Comparison of the spectral shift of the Fe=O stretching vibration of the studied complexes measured in the gas phase and in acetonitrile solution (complexes with the same ligand are color-coded: TMC as red, N4Py as blue, PyTACN as yellow).

3.3. Isomeric PyTACN Complexes

The $[(\text{PyTACN})\text{Fe}^{\text{IV}}(\text{O})(\text{X})]^+$ complexes can exist in two isomeric forms - with the oxo group parallel ("equatorial") or perpendicular ("axial") to the plane of the pyridine ring. Moreover, we had to consider both triplet and quintet spin states. In addition to the anion exchange in solution presented in the previous subsection, I attempted to generate these iron(IV)-oxo by a cleavage of nitrate group:



This method yielded different spectra for complexes **7** (X = OTf), **8** (X = NO₃) and **9** (X = CF₃COO), suggesting that we might have both the axial and equatorial isomers. The IRPD spectra of the complexes with the perchlorate ligand (**10**) were identical regardless of their preparation (i.e. transfer from solution or by nitrate cleavage; Figure 37). I was also not able to use the nitrate cleavage method to generate complex **6**, because I was not able to generate the required precursor ion $[(\text{PyTACN})\text{Fe}^{\text{III}}(\text{NO}_3)(\text{ACN})]^{2+}$ in solution. IRPD spectrum of **7** (Figure 34a) prepared in the gas phase by the "nitrate cleavage" differs from that of the ions generated from solution, but the detected additional bands do not suggest the presence of multiple iron(IV)-oxo isomers. Rather, the additional sulfonyl group bands (especially the band at 1010 cm⁻¹) suggest the presence of isobaric ions with an oxidized

ligand (Figure 34b). Initially generated isomers formed upon the nitrate cleavage are very reactive and the iron(IV)-oxo moiety attacks the ligand (probably at one of the nitrogen atoms of the ligand, forming the corresponding amine *N*-oxide).²²⁶

The comparison of the two methods used to obtain **8** is shown in Figure 39 (details for each method are section 2.3). Comparison of IRPD spectra of the complexes generated by these two methods (Figure 35, Figure 40) reveals distinct differences in the range of the nitrate antisymmetric stretching mode (bands around 1590 cm⁻¹) and around 900 cm⁻¹. Because the spectra partially overlap, we have studied the range from 1540 cm⁻¹ to 1640 cm⁻¹ by two color IRPD spectroscopy¹⁶⁴ (Figure 40b) of the ions generated in the gas phase. Here, irradiation at 1603 cm⁻¹ depletes the population of helium complexes absorbing at 1603 cm⁻¹. The spectrum of the residual population measured with the second IR laser shows decrease in the peaks at 1582 cm⁻¹ and 1603 cm⁻¹. Therefore, these two absorptions belong to one group of ions (predominantly generated in the gas-phase cleavage of nitrate). The ions generated in solution, on the other hand, show absorption at 1570 cm⁻¹. We have therefore assumed that the experimental IRPD spectra of ions generated by both methods are a linear combination of the spectra of two pure species. Under this assumption, we could extract the corresponding base spectra (Figure 40c, Figure 40c). The ratio of individual components was assumed such that no peaks in the base spectra are negative. The violet spectrum in Figure 40c therefore corresponds to the iron-oxo isomer predominantly generated in the gas phase by the nitrate cleavage, whereas the pink spectrum corresponds to the other iron-oxo isomer generated in solution.

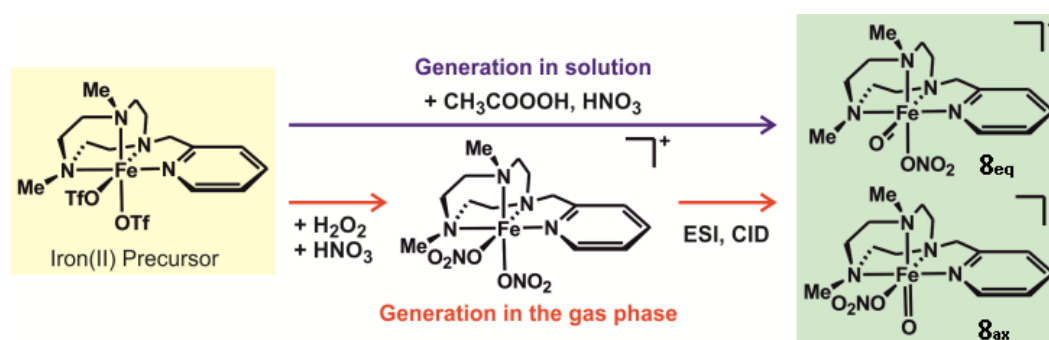


Figure 39. Generation of [(PyTACN)Fe^{IV}(O)(NO₃)]⁺ isomers by oxidation of the iron(II) precursor in solution or by in-source CID during electrospray ionization.

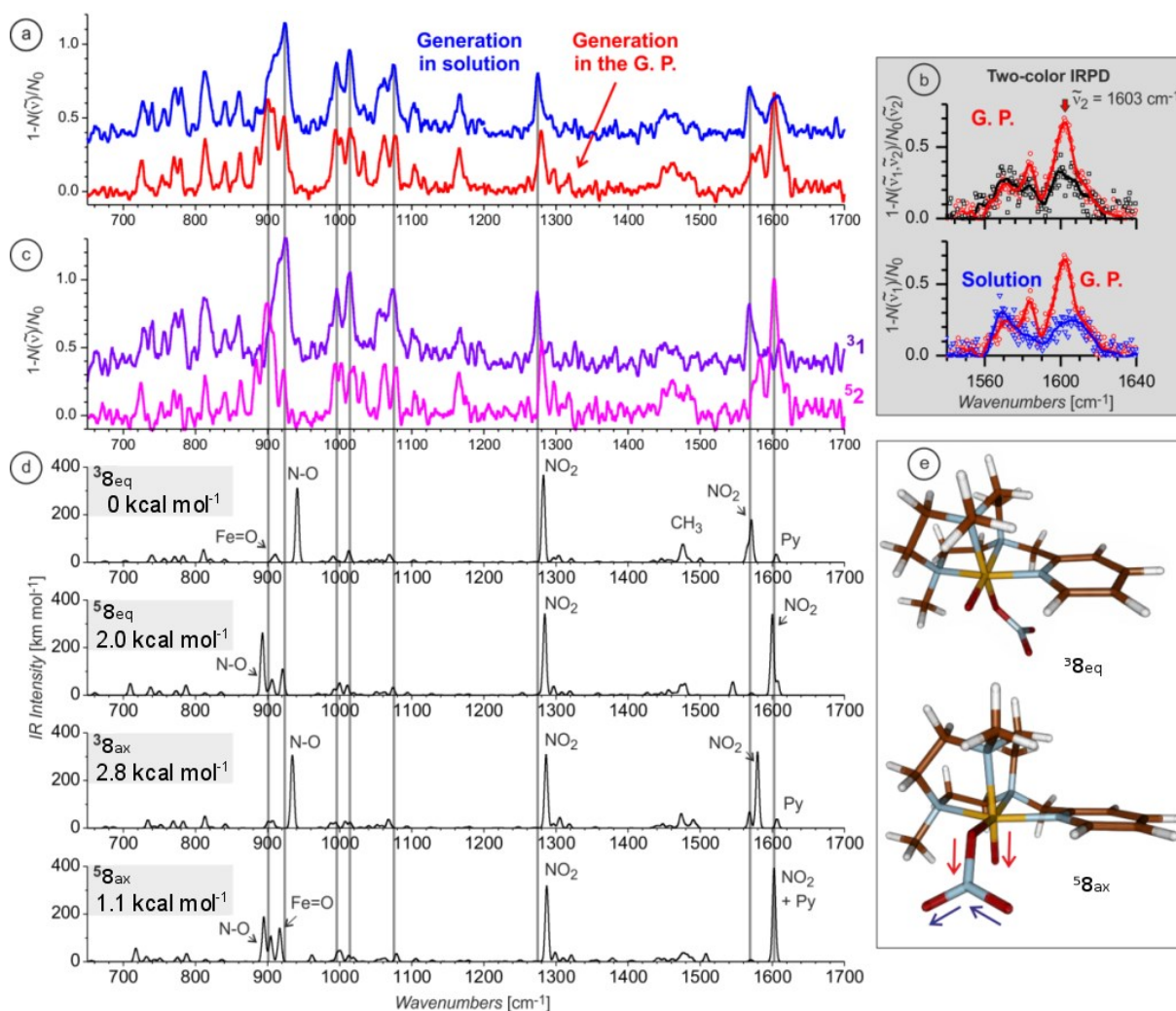


Figure 40. (a) IRPD spectra of $[(\text{PyTACN})\text{Fe}^{\text{IV}}(\text{O})(\text{NO}_3)]^+$ ions generated by oxidation in solution (blue trace, shifted by 0.4 on the y scale) or by in-source collisional activation (nitrate cleavage) during ESI ionization (red trace). (b) Top panel: Two-color IRPD experiment with the ions generated in the gas phase, one OPO was set to 1603 cm^{-1} , the second OPO was scanned (black trace). Lower panel shows one-color IRPD spectra from (a) in detail. (c) Separated spectra of the two complexes contributing to the IRPD spectra shown in (a). (d) Theoretical IR spectra of ${}^3\mathbf{8}_{\text{eq}}$, ${}^5\mathbf{8}_{\text{eq}}$, ${}^3\mathbf{8}_{\text{ax}}$, and ${}^5\mathbf{8}_{\text{ax}}$ calculated with B3LYP-D3/6-311++G**. Relative energies calculated at the same level of theory, including zero-point vibrational energies. Wavenumber-linear frequency scaling method was used to scale calculated vibrational frequencies – the scaling factors were 0.995 at 900 cm^{-1} and 0.975 at 1600 cm^{-1} . (e) The most stable structures of ${}^3\mathbf{8}_{\text{eq}}$ and ${}^5\mathbf{8}_{\text{ax}}$. Red arrows show the atoms displacements corresponding to the N-O and Fe=O stretching vibrations (bands at around 900 and at 851 cm^{-1}), the blue arrows show the antisymmetric stretch of the NO_2 group located around 1600 cm^{-1} .

The interpretation of the IRPD spectra is based on comparison with theoretical IR spectra of the possible isomers for the $[(\text{PyTACN})\text{Fe}^{\text{IV}}(\text{O})(\text{NO}_3)]^+$ complex (Figure 40d). We have assumed that the oxygen atom can either be in plane with the pyridine ($\mathbf{8}_{\text{eq}}$) or

perpendicular to the plane of the pyridine ($\mathbf{8}_{ax}$). Moreover, I excluded other spin states than triplet and quintet, because they are much higher in energy (Table 1). I also ruled out the oxidized structures based on the mismatch of IR spectra (compare Figure 40 with Figures 43 and 44 that show other isobaric oxidized structures). Ordering of the spin states cannot be reliably determined by DFT methods (Figure 41a). While the PBE/PBE functional energetically largely favors the triplet states of both isomers, B3LYP predicts ${}^3\mathbf{8}_{eq}$ as the most stable isomer followed by ${}^5\mathbf{8}_{ax}$. On the other side, the OPBE functional predicts ${}^5\mathbf{8}_{ax}$ as the most stable species and M06 functional largely stabilizes both quintet states.

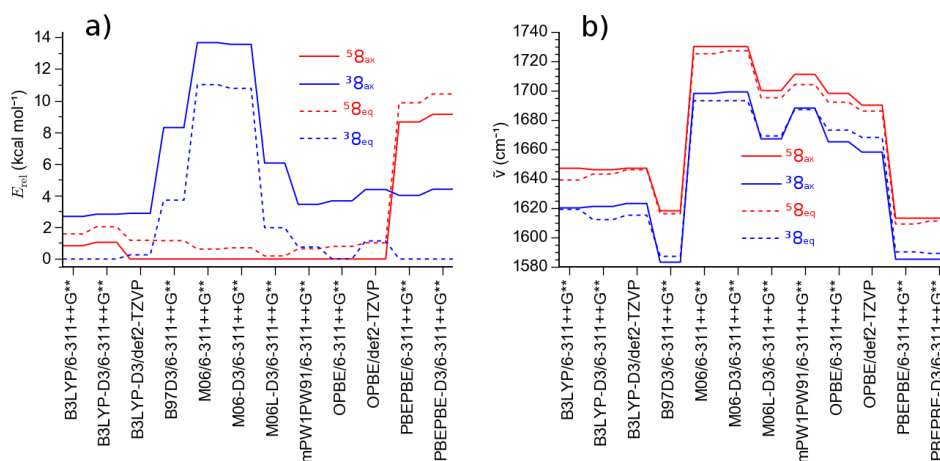


Figure 41. Relative stabilities (E_{rel}^{0K}) of isomers of **8** at different levels DFT of theory, (b) positions of the antisymmetric NO₂ stretch in isomers of **8** at different levels of DFT theory.

Table 1. Relative energies of spin isomers of δ_{eq} and δ_{ax} , their conformers and the isomers with hydroxylated ligands (cf. Figure 42) calculated at B3LYP-D3/6-311++G. Energies are given at 0 K in kJ.mol⁻¹.**

| Isomer ^a | $E_{\text{rel}}^{0\text{K}}$ (kcal.mol ⁻¹) | Isomer ^a | $E_{\text{rel}}^{0\text{K}}$ (kcal.mol ⁻¹) |
|--|---|--|---|
| ⁷ δ_{ax} | 23.0 | ⁵ CHOH (axial methylenic site) | -37.1 |
| ⁵ δ_{ax} | 1.1 | ³ CHOH axial methylenic site | -23.6 |
| ³ δ_{ax} | 2.8 | ¹ CHOH axial methylenic site | -26.3 |
| ¹ δ_{ax} | 31.0 | ⁵ CHOH equatorial methylenic site | -35.8 |
| ⁷ δ_{eq} | 20.8 | ³ CHOH equatorial methylenic site | -24.2 |
| ⁵ δ_{eq} | 2.0 | ¹ CHOH equatorial methylenic site | -31.3 |
| ³ δ_{eq} | 0.0 | ⁵ PyOH | -47.1 |
| ¹ δ_{eq} | 27.8 | ¹ PyOH | -40.8 |
| ⁵ δ_{ax} (bidentate NO ₃) | 4.1 | ⁵ PyNOX equatorial O | -0.2 |
| ⁵ δ_{eq} (NO ₃ rotated above pyridine) | 3.6 | ³ PyNOX equatorial O | 13.7 |
| ³ $\delta_{\text{eq a}}$ | 6.4 | ¹ PyNOX equatorial O | 9.1 |
| ³ $\delta_{\text{eq ab}}$ | 4.4 | ⁵ PyNOX axial O | 0.9 |
| ³ $\delta_{\text{eq bc}}$ | 4.8 | ³ PyNOX axial O | 15.9 |
| ⁵ $\delta_{\text{ax abc}}$ | 2.7 | ¹ PyNOX axial O | 9.4 |
| ³ $\delta_{\text{ax abc}}$ | 5.4 | | |
| ⁵ $\delta_{\text{eq abc}}$ | 2.9 | | |
| ³ $\delta_{\text{eq abc}}$ | 1.8 | | |
| ⁵ $\delta_{\text{eq abc}}$ (NO ₃ rotated above pyridine) | 4.3 | | |

^aIsomers are shown in Figure 42.

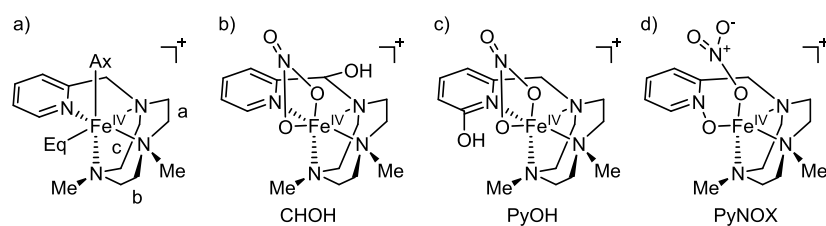


Figure 42. (a) Schematic representation $[(\text{PyTACN})\text{Fe}(\text{A})(\text{B})]^+$ with axial (Ax) and equatorial (Eq) ligands and ethylene bridges a,b and c. (b–d) Structures of possible isobaric ions with an oxidized PyTACN ligand.

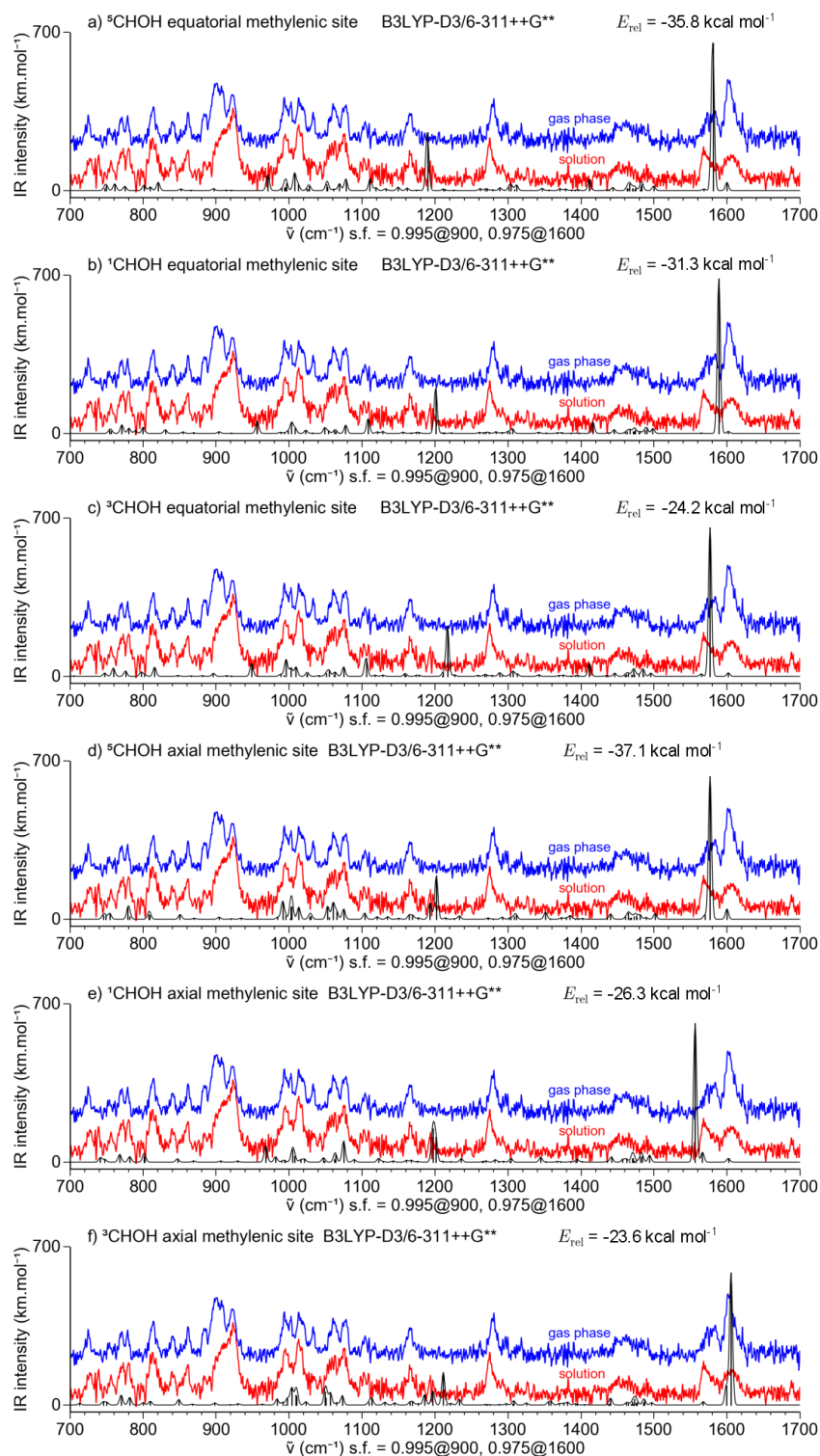


Figure 43. Theoretical spectra (black) of $[(\text{PyTACN-O})\text{Fe}^{\text{II}}(\text{NO}_3)]^+$ isomers with a ligand oxidized in the methylenic position next to pyridine (cf. Figure 42b). In (d), the band at 1200 cm^{-1} belongs to an NO_2 symmetric stretching vibration, the band at 1190 cm^{-1} belongs to a COH bending vibration and the band at 1070 cm^{-1} is due to a C–O stretching vibration. Relative energies include zero-point vibrational energies. Wavenumber-linear frequency scaling method was used to scale DFT vibrational frequencies – scaling factors are given in the figure.

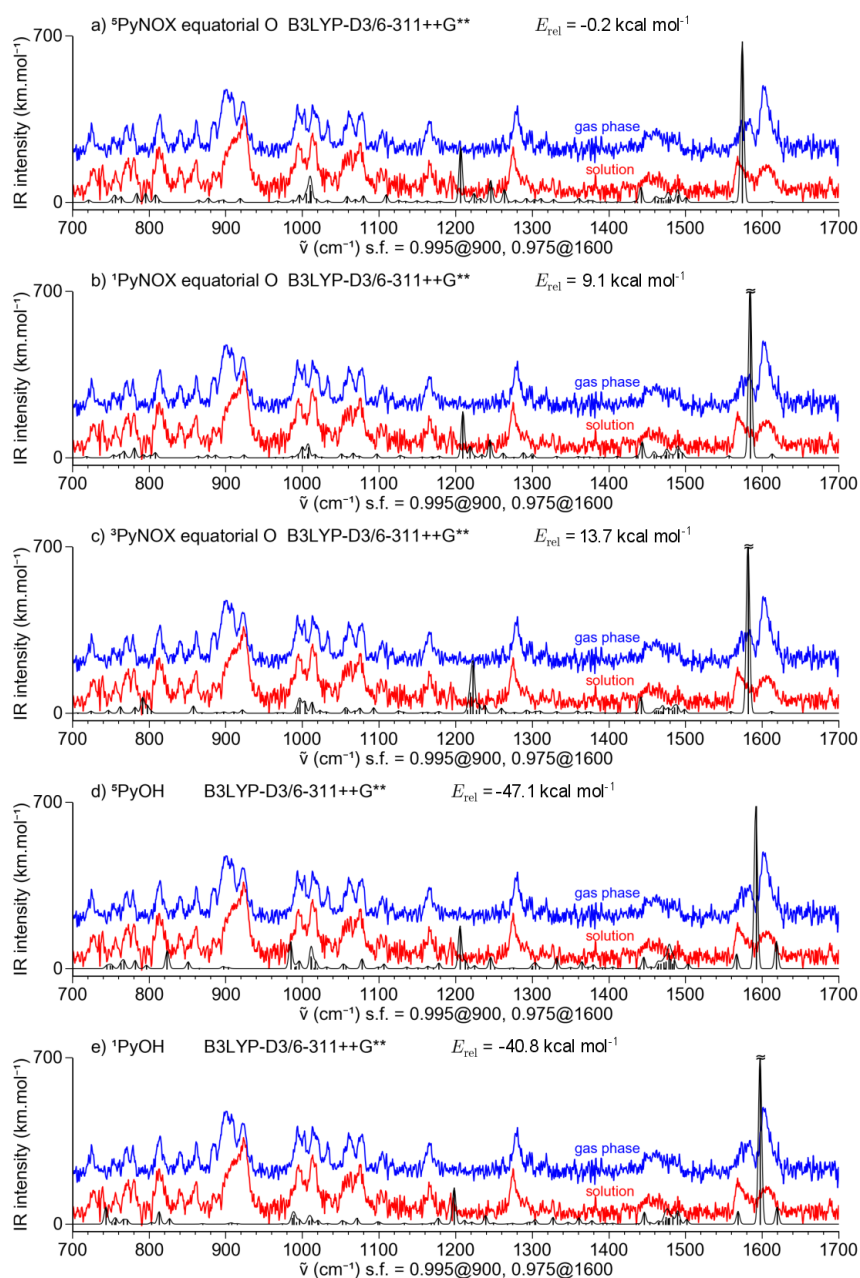


Figure 44. Theoretical spectra (black) of $[(\text{PyTACN-O})\text{Fe}^{\text{II}}(\text{NO}_3)]^+$ isomers (a,b,c) with a ligand oxidized at the pyridine oxygen forming *N*-oxide (cf. Figure 42d). In (a) the band at 1208 cm^{-1} is symmetric NO_2 stretching vibration and band at 1245 cm^{-1} is pyridine N–O stretching vibration, (d,e) with a ligand oxidized in the 6 position of the pyridine ring (cf. Figure 42c). In (d), the band at 1205 cm^{-1} is due to an NO_2 symmetric stretching vibration and the band at 1445 cm^{-1} comes from a C–O stretching vibration. Wavenumber-linear frequency scaling method was used to scale DFT vibrational frequencies – scaling factors are given in the figure.

Unlike the relative energies, the relative shift of the antisymmetric NO_2 stretch is predicted consistently. Figure 41b also shows, that the large difference ($\sim 30\text{ cm}^{-1}$) in the

position of this band between the two isomers cannot be explained by invoking $\mathbf{8}_{ax}$ and $\mathbf{8}_{eq}$ of the same spin state. The antisymmetric stretching of the NO_2 unit is blue-shifted for the quintet states with respect to the triplet states (Figure 41b). Natural population analysis²²⁷ shows that there is consistently larger spin localization at the nitrate counter ions for the quintet states which is reflected in the blue shift of the antisymmetric NO_2 stretch (Table 2). Another effect observed for the quintet state complexes is a red shift of the N–O vibration below 900 cm^{-1} (Figure 40d). Such shift is also observed experimentally (Figure 35). Therefore we conclude that the ions generated by in-source fragmentation (nitrate cleavage) of the iron(III) precursors are in the quintet state and the ions oxidized by peracetic acid in solution and transferred to the gas phase are in the triplet state.

DFT methods predict that the ${}^3\mathbf{8}_{eq}$ isomer is substantially more stable than the ${}^3\mathbf{8}_{ax}$ isomer by at least 4 kcal mol^{-1} . They are also much more reliable for determination of relative stabilities of isomers with the same multiplicity than in the prediction of relative energetics of different multiplicities.²²⁸ Therefore, we conclude that the triplet isomer that we see in the IR spectra must be ${}^3\mathbf{8}_{eq}$, presumably formed by substitution of the ACN ligand in **6** in the ESI process.

If the spin isomerization at the iron center is fast,^{92,93} we can also conclude that the other isomer (generated in the gas phase) must be ${}^5\mathbf{8}_{ax}$, because any ${}^5\mathbf{8}_{eq}$ formed would quickly relax to the triplet state. This is also consistent with the DFT calculations, where the quintet isomers ${}^5\mathbf{8}_{ax}$ are more stable than ${}^5\mathbf{8}_{eq}$ by an average of 1.5 kcal mol^{-1} . It is, therefore, possible, that we generate, by the nitrate cleavage a mixture of $\mathbf{8}_{ax}$ and $\mathbf{8}_{eq}$ in the quintet spin state and the $\mathbf{8}_{eq}$ complexes then relax to their triplet ground spin state. Therefore, the main species generated by the nitrate cleavage of the $[(\text{PyTACN})\text{Fe}^{\text{III}}(\text{NO}_3)_2]^+$ are the ${}^5\mathbf{8}_{ax}$ ions. Based on the analysis of IRPD spectra (subtraction of the IRPD spectra with the assumption that no peaks can be negative), the ratios of ${}^3\mathbf{8}_{eq}$ and ${}^5\mathbf{8}_{ax}$ are 0.75:0.25 for the ions transferred from the solution and 0.35:0.65 for the ions formed by in-source fragmentation of nitrate precursors.

Therefore, next to the triplet isomer ${}^3\mathbf{8}_{eq}$ obtained classically from solution, we have an independent access to the quintet isomer ${}^5\mathbf{8}_{ax}$, which allowed us to determine the influence of the spin state on the Fe=O stretching frequency. This was possible, because other factors known to influence this frequency, such as the nature of other ligands stay constant between the two isomers. Comparison of the IRPD spectrum in the range of the Fe=O vibrations of ${}^3\mathbf{8}_{eq}$ and its ${}^{18}\text{O}$ isotopomer, shown in the Figure 35a, leads to the assignment of Fe=O band at

850 cm⁻¹. Figure 35b shows the spectra extracted for the clean ³**8**_{eq} and ⁵**8**_{ax} species, by deconvolution of the experimental spectra. It shows a large difference in the N–O stretching band position, which reflects the different spin state (Figure 35c), similarly to the NO₂ antisymmetric stretching band position discussed above. Notably, the position of the Fe=O stretching band is almost identical. The Fe=O stretch of ⁵**8**_{ax} lies at 851.5 cm⁻¹, whereas the Fe=O stretch in ³**8**_{eq} is at 849.9 cm⁻¹. The difference is thus just 1.6 cm⁻¹ and it shows the negligible effect of the spin state on the Fe=O stretching frequency. This explains, why the experimental Fe=O stretching frequency cannot be correlated with the iron(IV)-oxo spin state.⁶⁷

The nitrate cleavage approach to preparation of [(PyTACN)Fe^{IV}(O)(CF₃COO)]⁺ (**9**) provides, similarly as in the case of **8**, IRPD spectrum distinct from the spectrum of **9** generated from solution (Figure 45a). Comparison of the two spectra (black vs. red trace) shows, that some peaks present in the red spectrum (transfer from solution) are also present in the red spectrum, but not the other way. Therefore, we suppose that the red spectrum corresponds to only one isomer, whereas the black spectrum is a mixture. To obtain the spectrum of the other (main) component in the black spectrum, we subtracted from it 30 % of the red spectrum. Details of this subtraction are shown in Figure 46. The major differences between the spectra of these pure components are located in the range 1130–1180 cm⁻¹. Comparison with the theoretical B3LYP spectra (Figure 45b) shows that the observed bands correspond to the C–F vibrations of the trifluoroacetate. These vibrations are influenced by the spin state of the complex. B3LYP predicts, that the lowest-energy C–F stretching band of triplet complexes **9**_{ax/eq} is red shifted with respect to the corresponding band of the quintet complexes **9**_{ax/eq}. Also, less pronounced blue shifts are predicted for the C=O vibration and the other C–F vibrations. Therefore the experimental spectra can be explained under the assumption that the red spectrum (ions generated by the nitrate cleavage) belongs to quintet complexes and the blue spectrum to mostly triplet complexes, with a 30 % admixture of the quintet isomer. Again, assuming that the DFT is relatively good at prediction of the relative energies of isomers of the same multiplicity, we assign the red spectrum of ⁵**9**_{ax} and the blue spectrum to ³**9**_{eq}.

The mechanism explaining the formation these complexes is that the ³**6** coordinates CF₃COO⁻ ions during the electrospray process. If trifluoroacetate coordinates to the equatorial position, it leads to ⁵**9**_{ax} – the more stable spin-isomer with the oxo in the axial position. Alternatively, the coordination of the anion to the axial position leads to the

formation of ${}^3\mathbf{9}_{\text{eq}}$. This line of reasoning also explains why nitrate coordinated complexes $\mathbf{8}$ are obtained from the oxidized solution in a similar ratio of ${}^3\mathbf{8}_{\text{eq}}$ to ${}^5\mathbf{8}_{\text{ax}}$.

Table 2. Relative energies at 0 K (kcal mol⁻¹), selected bond distances (Å), dihedral angles (degrees), NBO charges and spin densities and locations of NO₂ group stretching vibrations of δ_{eq} and δ_{ax} spin isomers.

| method | isomer | $E_{\text{rel}}^{\text{OK}}$ | dist. Fe=O | dist. Fe-O' | dist. O-N | dist. N-O'' | dist. N-O''' | dihedral angle OFeON | NBO charge Fe | NBO charge O | NBO charge NO ₃ | NBO spin dens. Fe | NBO spin dens. O | NBO spin dens. | $\tilde{\nu}$ symm. NO ₂ | $\tilde{\nu}$ antisymm. NO ₂ |
|-------------------------|------------------------|------------------------------|------------|-------------|-----------|-------------|--------------|----------------------|---------------|--------------|----------------------------|-------------------|------------------|----------------|-------------------------------------|---|
| B3LYP/ 6-311++G** | $^5\delta_{\text{ax}}$ | 0.8 | 1.622 | 1.906 | 1.375 | 1.211 | 1.212 | 6.1 | 0.90 | -0.40 | -0.53 | 2.70 | 0.75 | 0.21 | 1309 | 1647 |
| | $^3\delta_{\text{ax}}$ | 2.7 | 1.628 | 1.925 | 1.359 | 1.214 | 1.218 | 22.9 | 0.54 | -0.34 | -0.54 | 1.05 | 0.96 | 0.00 | 1307 | 1620 |
| | $^5\delta_{\text{eq}}$ | 1.6 | 1.619 | 1.937 | 1.373 | 1.211 | 1.213 | 16.3 | 0.91 | -0.41 | -0.55 | 2.71 | 0.74 | 0.19 | 1306 | 1639 |
| B3LYP-D3/ 6-311++G** | $^3\delta_{\text{eq}}$ | 0.0 | 1.625 | 1.921 | 1.360 | 1.215 | 1.216 | 44.1 | 0.53 | -0.35 | -0.53 | 1.04 | 0.96 | -0.01 | 1303 | 1619 |
| | $^5\delta_{\text{ax}}$ | 1.1 | 1.621 | 1.907 | 1.374 | 1.210 | 1.213 | 8.0 | 0.90 | -0.41 | -0.53 | 2.70 | 0.74 | 0.22 | 1309 | 1646 |
| | $^3\delta_{\text{ax}}$ | 2.8 | 1.629 | 1.924 | 1.361 | 1.215 | 1.217 | 16.4 | 0.53 | -0.34 | -0.55 | 1.04 | 0.97 | 0.00 | 1308 | 1621 |
| B3LYP-D3/ def2-TZVP | $^5\delta_{\text{eq}}$ | 2.0 | 1.616 | 1.936 | 1.374 | 1.211 | 1.213 | 16.6 | 0.92 | -0.42 | -0.55 | 2.71 | 0.73 | 0.20 | 1306 | 1643 |
| | $^3\delta_{\text{eq}}$ | 0.0 | 1.625 | 1.915 | 1.355 | 1.214 | 1.220 | 65.7 | 0.52 | -0.35 | -0.53 | 1.03 | 0.95 | 0.00 | 1304 | 1612 |
| | $^5\delta_{\text{ax}}$ | 0.0 | 1.618 | 1.903 | 1.372 | 1.207 | 1.209 | 7.7 | 0.90 | -0.39 | -0.53 | 2.69 | 0.73 | 0.22 | 1311 | 1647 |
| B97/ 6-311++G** | $^3\delta_{\text{ax}}$ | 2.9 | 1.626 | 1.923 | 1.359 | 1.211 | 1.214 | 16.2 | 0.46 | -0.32 | -0.54 | 1.07 | 0.94 | 0.00 | 1311 | 1623 |
| | $^5\delta_{\text{eq}}$ | 1.2 | 1.614 | 1.930 | 1.373 | 1.206 | 1.210 | 17.2 | 0.91 | -0.41 | -0.54 | 2.70 | 0.71 | 0.21 | 1309 | 1646 |
| | $^3\delta_{\text{eq}}$ | 0.3 | 1.622 | 1.913 | 1.353 | 1.211 | 1.216 | 65.7 | 0.45 | -0.32 | -0.52 | 1.06 | 0.93 | 0.00 | 1307 | 1615 |
| M06/ 6-311++G** | $^5\delta_{\text{ax}}$ | 0.0 | 1.637 | 1.903 | 1.402 | 1.213 | 1.214 | 6.7 | 0.79 | -0.40 | -0.45 | 2.60 | 0.78 | 0.29 | 1260 | 1618 |
| | $^3\delta_{\text{ax}}$ | 8.3 | 1.643 | 1.913 | 1.382 | 1.219 | 1.220 | 31.7 | 0.41 | -0.32 | -0.48 | 1.10 | 0.95 | -0.02 | 1252 | 1583 |
| | $^5\delta_{\text{eq}}$ | 1.1 | 1.633 | 1.927 | 1.402 | 1.212 | 1.215 | 16.0 | 0.79 | -0.41 | -0.46 | 2.60 | 0.76 | 0.29 | 1258 | 1616 |
| M06-D3/ 6-311++G** | $^3\delta_{\text{eq}}$ | 3.7 | 1.639 | 1.911 | 1.384 | 1.217 | 1.220 | 54.5 | 0.41 | -0.33 | -0.47 | 1.12 | 0.94 | -0.02 | 1253 | 1587 |
| | $^5\delta_{\text{ax}}$ | 0.0 | 1.617 | 1.898 | 1.360 | 1.200 | 1.202 | 6.4 | 0.92 | -0.43 | -0.53 | 2.82 | 0.64 | 0.21 | 1368 | 1730 |
| | $^3\delta_{\text{ax}}$ | 13.6 | 1.624 | 1.914 | 1.346 | 1.204 | 1.207 | 20.9 | 0.51 | -0.35 | -0.54 | 1.09 | 0.93 | -0.01 | 1364 | 1698 |
| M06L-D3/ 6-311++G** | $^5\delta_{\text{eq}}$ | 0.6 | 1.614 | 1.924 | 1.360 | 1.200 | 1.203 | 16.9 | 0.93 | -0.44 | -0.54 | 2.83 | 0.63 | 0.19 | 1364 | 1725 |
| | $^3\delta_{\text{eq}}$ | 11.0 | 1.620 | 1.904 | 1.343 | 1.205 | 1.208 | 61.6 | 0.50 | -0.35 | -0.52 | 1.09 | 0.92 | 0.00 | 1362 | 1693 |
| | $^5\delta_{\text{ax}}$ | 0.0 | 1.617 | 1.898 | 1.360 | 1.200 | 1.202 | 6.3 | 0.92 | -0.43 | -0.53 | 2.82 | 0.64 | 0.21 | 1368 | 1730 |
| mPW1PW91/ 6-311++G** | $^3\delta_{\text{ax}}$ | 13.6 | 1.624 | 1.913 | 1.345 | 1.204 | 1.207 | 21.2 | 0.51 | -0.35 | -0.54 | 1.09 | 0.93 | -0.01 | 1365 | 1699 |
| | $^5\delta_{\text{eq}}$ | 2.3 | 1.614 | 1.924 | 1.360 | 1.199 | 1.203 | 17.5 | 0.93 | -0.44 | -0.55 | 2.83 | 0.63 | 0.19 | 1364 | 1727 |
| | $^3\delta_{\text{eq}}$ | 10.8 | 1.620 | 1.904 | 1.342 | 1.204 | 1.208 | 61.6 | 0.50 | -0.35 | -0.52 | 1.09 | 0.92 | 0.00 | 1362 | 1693 |
| OPBE/ 6-311++G** | $^5\delta_{\text{ax}}$ | 0.0 | 1.633 | 1.901 | 1.385 | 1.207 | 1.208 | 7.2 | 0.92 | -0.45 | -0.49 | 2.73 | 0.68 | 0.26 | 1320 | 1700 |
| | $^3\delta_{\text{ax}}$ | 6.0 | 1.641 | 1.911 | 1.363 | 1.211 | 1.216 | 34.6 | 0.56 | -0.36 | -0.51 | 1.07 | 0.95 | -0.01 | 1317 | 1667 |
| | $^5\delta_{\text{eq}}$ | 0.2 | 1.629 | 1.928 | 1.383 | 1.207 | 1.209 | 15.3 | 0.93 | -0.45 | -0.50 | 2.73 | 0.67 | 0.25 | 1319 | 1695 |
| OPBE/ def2-TZVP | $^3\delta_{\text{ax}}$ | 2.0 | 1.636 | 1.919 | 1.365 | 1.221 | 1.227 | 70.8 | 0.55 | -0.36 | -0.51 | 1.07 | 0.94 | 0.00 | 1320 | 1669 |
| | $^5\delta_{\text{ax}}$ | 0.0 | 1.608 | 1.900 | 1.354 | 1.203 | 1.205 | 6.6 | 0.89 | -0.40 | -0.54 | 2.76 | 0.70 | 0.20 | 1367 | 1711 |
| | $^3\delta_{\text{ax}}$ | 3.4 | 1.614 | 1.910 | 1.342 | 1.206 | 1.209 | 20.1 | 0.50 | -0.34 | -0.54 | 1.05 | 0.96 | 0.00 | 1366 | 1688 |
| PBE/ 6-311++G** | $^5\delta_{\text{eq}}$ | 0.6 | 1.605 | 1.932 | 1.352 | 1.204 | 1.206 | 17.8 | 0.90 | -0.40 | -0.56 | 2.77 | 0.70 | 0.17 | 1363 | 1704 |
| | $^3\delta_{\text{eq}}$ | 0.8 | 1.611 | 1.903 | 1.341 | 1.207 | 1.208 | 45.1 | 0.49 | -0.34 | -0.53 | 1.04 | 0.96 | -0.01 | 1361 | 1687 |
| | $^5\delta_{\text{ax}}$ | 0.0 | 1.620 | 1.892 | 1.377 | 1.208 | 1.208 | 4.7 | 0.80 | -0.38 | -0.44 | 2.61 | 0.78 | 0.29 | 1319 | 1698 |
| PBE-D3/ 6-311++G** | $^3\delta_{\text{ax}}$ | 3.7 | 1.626 | 1.905 | 1.360 | 1.213 | 1.215 | 31.3 | 0.40 | -0.30 | -0.47 | 1.11 | 0.94 | -0.03 | 1314 | 1665 |
| | $^5\delta_{\text{eq}}$ | 0.8 | 1.616 | 1.921 | 1.376 | 1.208 | 1.209 | 13.4 | 0.80 | -0.39 | -0.44 | 2.61 | 0.77 | 0.30 | 1316 | 1692 |
| | $^3\delta_{\text{eq}}$ | 0.0 | 1.623 | 1.909 | 1.362 | 1.210 | 1.216 | 44.0 | 0.38 | -0.31 | -0.45 | 1.12 | 0.94 | -0.03 | 1315 | 1673 |
| PBE-D3/ 6-311++G** | $^5\delta_{\text{ax}}$ | 0.0 | 1.618 | 1.886 | 1.377 | 1.207 | 1.207 | 4.3 | 0.78 | -0.35 | -0.43 | 2.63 | 0.76 | 0.29 | 1314 | 1690 |
| | $^3\delta_{\text{ax}}$ | 4.4 | 1.624 | 1.905 | 1.358 | 1.211 | 1.214 | 31.7 | 0.31 | -0.27 | -0.45 | 1.15 | 0.92 | -0.03 | 1310 | 1658 |
| | $^5\delta_{\text{eq}}$ | 1.0 | 1.615 | 1.913 | 1.376 | 1.206 | 1.208 | 14.2 | 0.78 | -0.36 | -0.43 | 2.63 | 0.75 | 0.30 | 1311 | 1686 |
| PBE-D3/ 6-311++G** | $^3\delta_{\text{eq}}$ | 1.1 | 1.622 | 1.910 | 1.361 | 1.208 | 1.214 | 43.1 | 0.29 | -0.27 | -0.43 | 1.16 | 0.92 | -0.04 | 1311 | 1668 |
| | $^5\delta_{\text{ax}}$ | 8.7 | 1.644 | 1.902 | 1.405 | 1.218 | 1.219 | 6.5 | 0.74 | -0.39 | -0.44 | 2.51 | 0.81 | 0.31 | 1255 | 1613 |
| | $^3\delta_{\text{ax}}$ | 4.0 | 1.651 | 1.913 | 1.389 | 1.223 | 1.225 | 34.2 | 0.40 | -0.33 | -0.48 | 1.06 | 0.93 | 0.00 | 1250 | 1585 |
| PBE-D3/ 6-311++G** | $^5\delta_{\text{eq}}$ | 9.8 | 1.639 | 1.930 | 1.404 | 1.217 | 1.219 | 14.4 | 0.74 | -0.40 | -0.44 | 2.51 | 0.79 | 0.32 | 1254 | 1609 |
| | $^3\delta_{\text{eq}}$ | 0.0 | 1.647 | 1.915 | 1.393 | 1.222 | 1.223 | 47.5 | 0.39 | -0.34 | -0.46 | 1.06 | 0.93 | 0.00 | 1251 | 1590 |
| | $^5\delta_{\text{ax}}$ | 9.1 | 1.643 | 1.903 | 1.404 | 1.218 | 1.219 | 7.0 | 0.74 | -0.40 | -0.44 | 2.51 | 0.80 | 0.31 | 1255 | 1613 |
| PBE-D3/ 6-311++G** | $^3\delta_{\text{ax}}$ | 4.4 | 1.652 | 1.911 | 1.388 | 1.223 | 1.225 | 31.6 | 0.39 | -0.33 | -0.48 | 1.05 | 0.94 | 0.00 | 1250 | 1585 |
| | $^5\delta_{\text{eq}}$ | 10.4 | 1.638 | 1.930 | 1.405 | 1.217 | 1.219 | 15.3 | 0.75 | -0.41 | -0.44 | 2.52 | 0.79 | 0.32 | 1253 | 1611 |
| | $^3\delta_{\text{eq}}$ | 0.0 | 1.647 | 1.912 | 1.391 | 1.222 | 1.224 | 51.0 | 0.38 | -0.34 | -0.46 | 1.06 | 0.93 | 0.00 | 1251 | 1589 |

^aDesignation of the O atoms in the nitrate ligand:

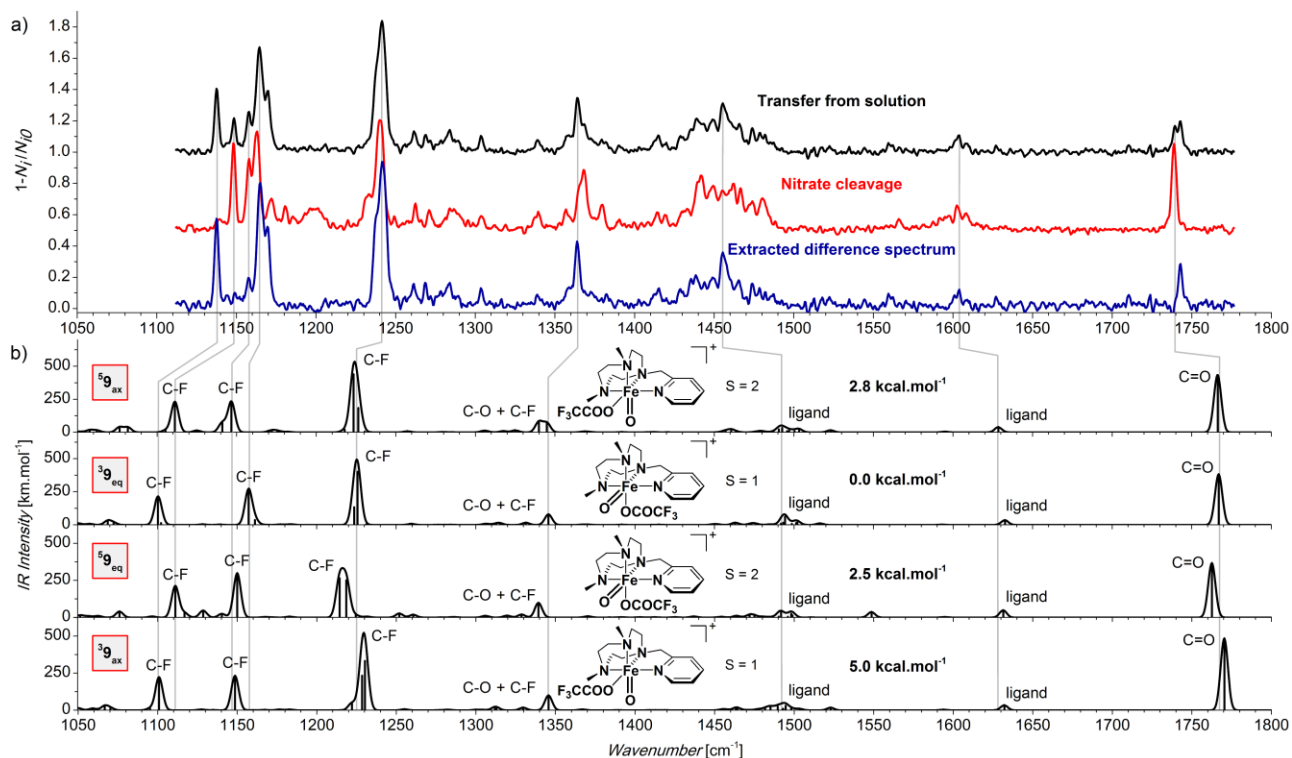


Figure 45. (a) IRPD spectra of the $[(\text{PyTACN})\text{Fe}^{\text{IV}}(\text{O})(\text{CF}_3\text{COO})]^+$ (**9**) isomers generated by ligand exchange from the solution of $[(\text{PyTACN})\text{Fe}^{\text{IV}}(\text{O})(\text{CH}_3\text{CN})]^{2+}$ (the upper trace), generated in the gas phase from $[(\text{PyTACN})\text{Fe}^{\text{III}}(\text{NO}_3)(\text{CF}_3\text{COO})]^+$ by the nitrate cleavage (the middle trace) and the extracted difference spectrum (the lowest trace). (b) Theoretically predicted spectra of various isomers at the B3LYP-D3/BS1 level of theory scaled by 0.99. Energies are calculated at the CASPT2 level with DFT zero-point energy corrections.

Table 3. Relative CASPT2 energies^a of [(PyTACN)Fe^{IV}(O)(X)]⁺ spin isomers.

| $E_{\text{rel}}^{\text{tot}}(\text{kcal mol}^{-1}).(E_{\text{rel}}^{\text{0K}}(\text{kcal mol}^{-1}))$ | | | |
|--|---------------------------------|----------------------------|------------------------|
| Complex | X | Energy CASPT2 ^a | Energy B3LYP |
| ³ 7 _{eq} | CF ₃ SO ₃ | 0.0 (1.1) | 0.0 (0.0) |
| ³ 7 _{ax} | CF ₃ SO ₃ | 2.3 (3.6) | 3.3 (3.1) |
| ⁵ 7 _{eq} | CF ₃ SO ₃ | 0.1 (0.0) | 2.0 (3.2) |
| ⁵ 7 _{ax} | CF ₃ SO ₃ | 1.5 (1.4) | 3.0 (4.3) |
| ³ 8 _{eq} | NO ₃ | 0.0 (0.0) | 0.0 (0.0) |
| ³ 8 _{ax} | NO ₃ | 2.6 (2.4) | 2.6 (2.8) |
| ⁵ 8 _{eq} | NO ₃ | 2.1 (1.5) ^b | 3.0 (3.6) ^b |
| ⁵ 8 _{ax} | NO ₃ | 0.4 (0.0) | 0.7 (1.1) |
| ³ 9 _{eq} | CF ₃ COO | 0.0 (0.0) | 0.0 (0.0) |
| ³ 9 _{ax} | CF ₃ COO | 5.2 (5.0) | 4.7 (4.5) |
| ⁵ 9 _{eq} | CF ₃ COO | 3.0 (2.5) | 3.9 (3.4) |
| ⁵ 9 _{ax} | CF ₃ COO | 3.5 (2.8) | 4.0 (3.3) |
| ³ 10 _{eq} | ClO ₄ | 1.0 (2.6) | 0.0 (0.0) |
| ³ 10 _{ax} | ClO ₄ | 3.2 (4.9) | 3.3 (3.2) |
| ⁵ 10 _{eq} | ClO ₄ | 0.0 (0.0) | 1.6 (3.2) |
| ⁵ 10 _{ax} | ClO ₄ | 3.7 (4.7) | 2.1 (2.7) |

^aCalculations were performed by CASPT2(12,9)/ANO-RCC at geometries optimized at B3LYP-D3 level of theory as described in section 2.6. The numbers in brackets are the CASPT2 energies corrected by zero-point vibrational energy calculated with the B3LYP-D3 functional.

^bThis energy corresponds to the conformer with NO₃ rotated above pyridine, which is not the minimum energy conformer – the minimum for ⁵8_{eq} is at 2.5 (2.0) kcal mol⁻¹.

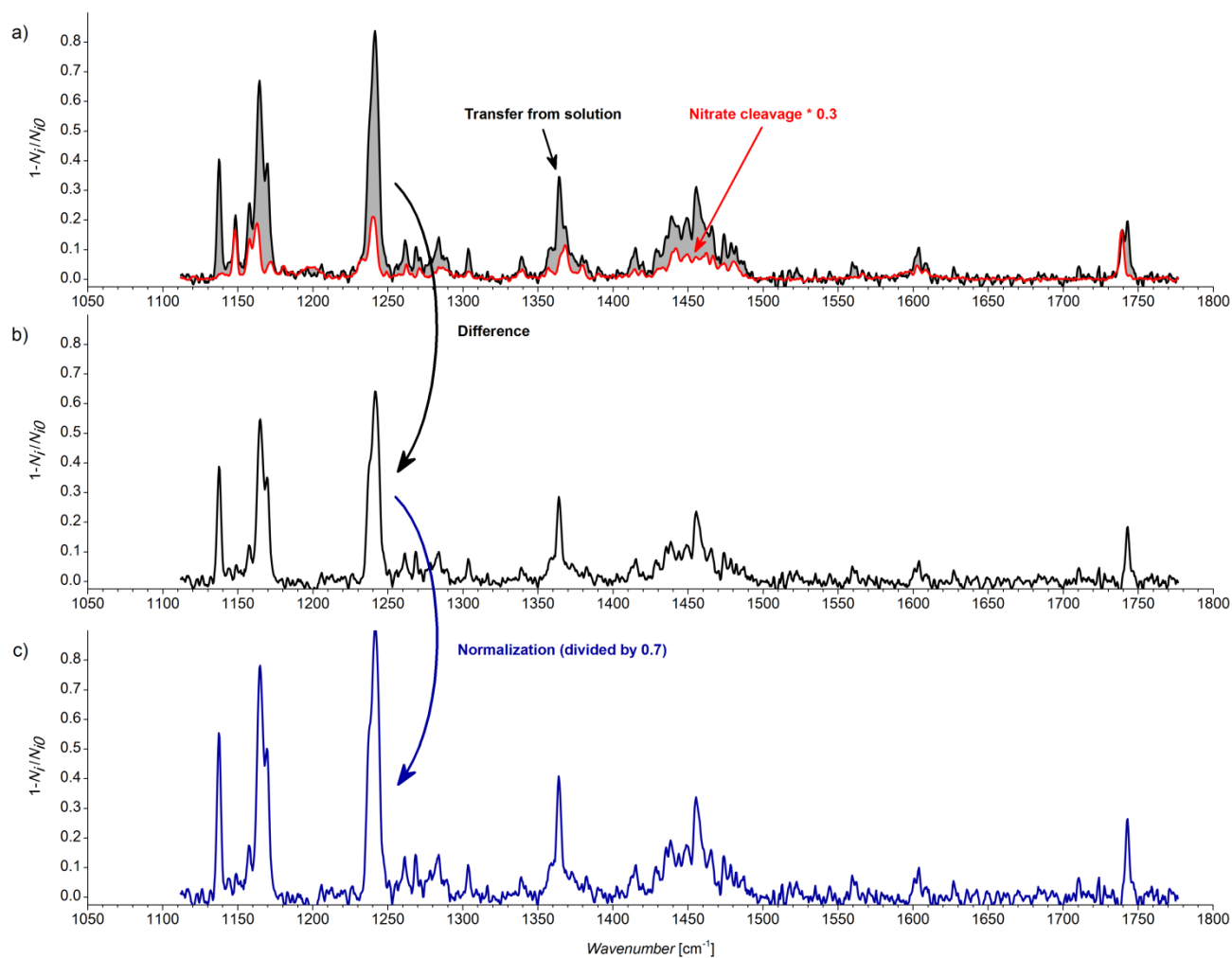
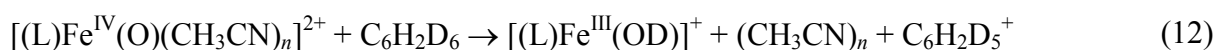
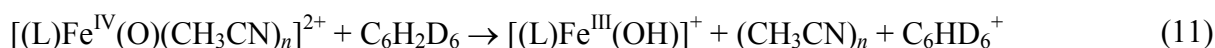


Figure 46. The spectrum of the $[(\text{PyTACN})\text{Fe}^{\text{IV}}(\text{O})(\text{CF}_3\text{COO})]^+$ (**9**) ions obtained by spraying the PyTACN iron(IV)-oxo solution containing trifluoroacetate ((a), black trace) consists of a mixture of two isomers as can be told from the observation of the same peaks which are present also in spectrum of **9** by the nitrate cleavage in the gas phase ((a), red trace). Therefore, the latter was multiplied by maximum possible number (in this case: 0.3), which after subtraction (b) did not give any negative peaks. The difference spectrum was then normalized to obtain the final spectrum (c) of the other isomer.

3.4. Gas-Phase Reactivity

Having well-characterized iron(IV)-oxo complexes in hand, I tested their reactivity in HAT reaction with a prototypical substrate – 1,4-cyclohexadiene-1,2,3,4,5,6-d₆, that features relatively weak C–H bond. It also enabled me to measure the intramolecular kinetic isotope effect of the HAT from its allylic position. First, I tested reactivity of iron(IV)-oxo dicationic complexes (**1**, **4** and **6**, Figure 49a,c,e, Entries 1,3,5 in Table 4). I observed hydride/D⁻ transfer instead of the more common HAT/DAT (Equations (11) and (12)). The driving force of this reaction is the possibility of charge separation, and such reactions are quite common feature in doubly charged ions.²²⁹ It is also highly, exothermic, which leads to the loss of ACN ligand in **1** and **6**, where it is present. I did not observe any OAT reactivity. The reactivity pattern, where doubly charged ions are not formed is most likely an artifact of the gas-phase chemistry, where the lack of solvation destabilizes doubly charged products.



The total reactivity of iron(IV)-oxo dications in the gas phase can be ordered as **6** (PyTACN ligand) > **1** (TMC ligand) >> **4** (N4Py ligand) (Entries 5, 1 and 3 in Table 4). This order is different from the reactivities of iron(IV)-oxo species in solution with DHA (with weak C–H bonds), which are in order PyTACN ≈ N4Py > TMC (Figure 48). These differences may arise from a solvent effect or from the presence of anions.

To find out, whether the reactivity differences between the gas phase and the condensed phase may be caused by coordination of anions in solution, I measured reactivity of the three complexes featuring a triflate counterion (**2**, **5**, **7**, Entries 2,4,6, in Table 4, Figure 49b,d,f). These singly charged complexes follow the HAT/DAT reaction channel as well as OAT channel. OAT channel shows intermolecular KIE 1 in reaction with 1,4-cyclohexadiene-1,2,3,4,5,6-d₆ (against 1,4-cyclohexadiene), indicating that the reaction rate of the OAT channel does not depend on the C–H bond cleavage. Considering the two possible ways that arrive at the OAT product ions shown in Figure 47, HAT followed by OH rebound and double bond epoxidation, we can see that only the epoxidation of the double bond is consistent with the observed KIE, because it does not involve C–H bond cleavage step. This means that the OAT reaction corresponds to the epoxidation of the double bond.

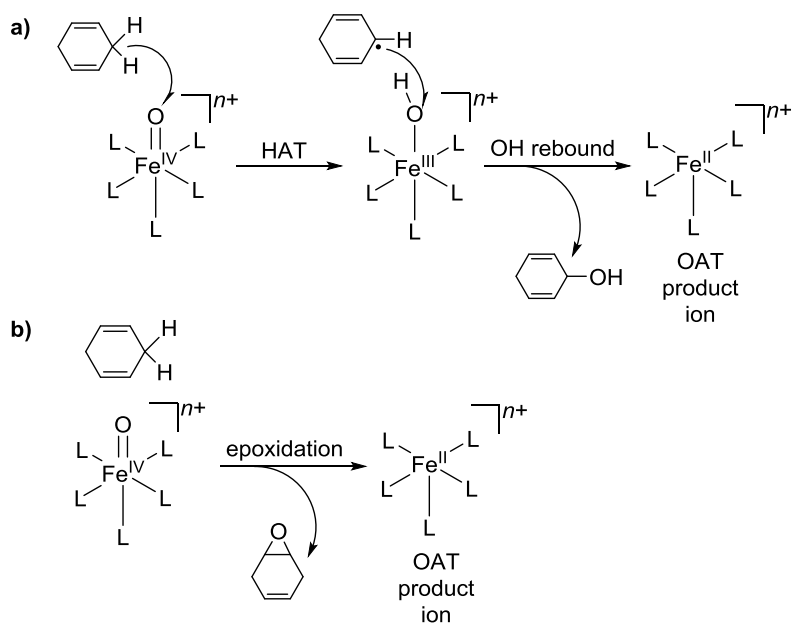


Figure 47. (a) HAT followed by OH rebound and (b) epoxidation of the double bond can explain the formation of product ion corresponding to OAT in reaction of an iron(IV)-oxo complex with 1,4-cyclohexadiene.

Somewhat surprisingly, the total reactivities of monocations **5** (N4Py ligand) and **7** (PyTACN ligand) are of the same order of magnitude as those of their respective dications **4** and **6**. This contrasts with the complex **2** (TMC ligand), which is unreactive. This most likely reflects the different binding of the triflate ligand. The *cis*-coordinated triflate (with respect to the oxo group) in complex **7** influences the reactivity only slightly (50 % decrease; Entry 5 vs. 6 in Table 4). The same holds true for complex **5**, where the triflate is not coordinated to the iron center at all (Entry 3 vs. 4 in Table 4). In complex **2**, the binding of the triflate anion is in the *trans*-position with respect to the oxo group, which is probably beyond its large influence on the observed reactivity. Therefore, the formation of the triflate-coordinated complexes **2** out of the acetonitrile-containing **1** can affect the overall reactivity of the TMC complexes by decreasing a number of the reactive species **1** in solution. The same process should not significantly influence the reactivity of the complexes with N4Py and PyTACN ligands. It can thus explain the observed reactivity trend in the condensed phase (Figure 48).

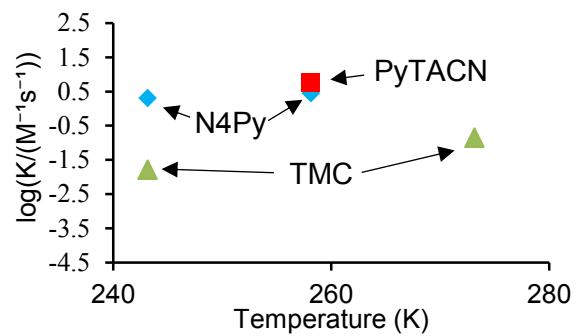


Figure 48. Plot of reactivity of various iron(IV)-oxo species with 9,10-dihydroanthracene in acetonitrile against temperature. Data were taken from Refs 54, 137 and 154.

Table 4. Reactivities of $[(L)Fe^{IV}(O)(X)]^{2+/+}$ complexes with 1,4-cyclohexadiene-1,2,3,4,5,6- d_6 in the gas phase.^a

| Entry | L/X | from ^a | Total reactivity ^b | Branching [%] HAT:DAT:OAT | KIE |
|-------|---|-------------------|-------------------------------|------------------------------|--------------------|
| 1 | TMC/ACN (1) | sol. | 360 ± 190 | 72:28: 0 ^c | 2.5 ± 0.6 |
| 2 | TMC/CF ₃ SO ₃ (2) | sol. | <3 | - | - |
| | 2 + <i>unlabeled CHD</i> | sol. | <2 | - | - |
| 3 | N4Py/- (4) | sol. | 10 ± 6 | 85:15: 0 ^{c,d} | 5.7 ± 2.1 |
| 4 | N4Py/CF ₃ SO ₃ (5) | sol. | | | 3.7 ± 0.4 ; |
| | 5 + <i>unlabeled CHD</i> | sol. | 5 ± 2 | 56:15:29 | (6.8) ^e |
| | | sol. | 8 ± 2 | 73:-:27 | - |
| 5 | PyTACN/ACN (6) | sol. | 900 ± 400 | 79:21: 0 ^c | 3.8 ± 0.5 |
| 6 | PyTACN/CF ₃ SO ₃ (7) | sol. | 454 ± 11 | 56:16:28 | 3.5 ± 0.3 |
| | 7 + <i>unlabeled CHD</i> | sol. | 550 ± 50 | 77:-:23 | - |
| 7 | PyTACN/CF ₃ SO ₃ (7) | frag. | 187 ± 46^f | 56:13:31 | 4.3 ± 0.2 |
| 8 | PyTACN/NO ₃ (8) | sol. | 100 ± 8 | 78:14: 8 | 5.6 ± 0.1 |
| 9 | PyTACN/NO ₃ (8) | frag. | 195 ± 10 | 74:16:10 | 4.6 ± 0.3 |
| 10 | PyTACN/CF ₃ COO (9) | sol. | 67 ± 13 | 76:14: 9 | 5.4 ± 1.4 |
| 11 | PyTACN/CF ₃ COO (9) | frag. | 238 ± 52 | 72:16:12 | 4.5 ± 0.2 |
| 12 | PyTACN/ClO ₄ (10) | sol. | 260 | 63:17:20 | 3.7 |
| 13 | PyTACN/ClO ₄ (10) | frag. | 261 ± 12 | 59:16:25 | 3.7 ± 0.3 |

^aThe $[(PyTACN)Fe^{IV}(O)(X)]^{2+/+}$ complexes were generated by oxidation in solution and transferred by ESI to the gas phase (denoted as sol.) or by a fragmentation of their iron(III) nitrate precursors during the electrospray process (denoted as frag.)

^bTotal reactivity (sum of the rate constants for HAT, DAT, and OAT) is given relative to the reactivity of $[(PyTACN)Fe^{IV}(O)(NO_3)]^+$ transferred from the solution, which was determined to be $(8.4 \pm 3.1) \times 10^{-12} \text{ cm}^3 \text{ s}^{-1}$ (Table 5) and is set as 100 here.

^cFor dications, we observe a transfer of H^-/D^- instead of HAT and DAT (Equations (11) and (12)). Note that for **1** and **6** the H^-/D^- transfer is associated with elimination of acetonitrile

^dI have observed also the electron transfer channel (7 % with respect to the total reactivity). We assume that this channel is due to a reaction with an impurity.

^eThe measured KIE is affected by a presence of an isobaric impurity (m/z 588) which undergoes a Coulomb explosion to ions with m/z 586 and m/z 590. After subtraction of this impurity we obtain a KIE of 6.8.

^fNote that this number is hampered by the fact that we worked with a mixture of **7** with unreactive Fe^{II} complexes with oxidized ligand.

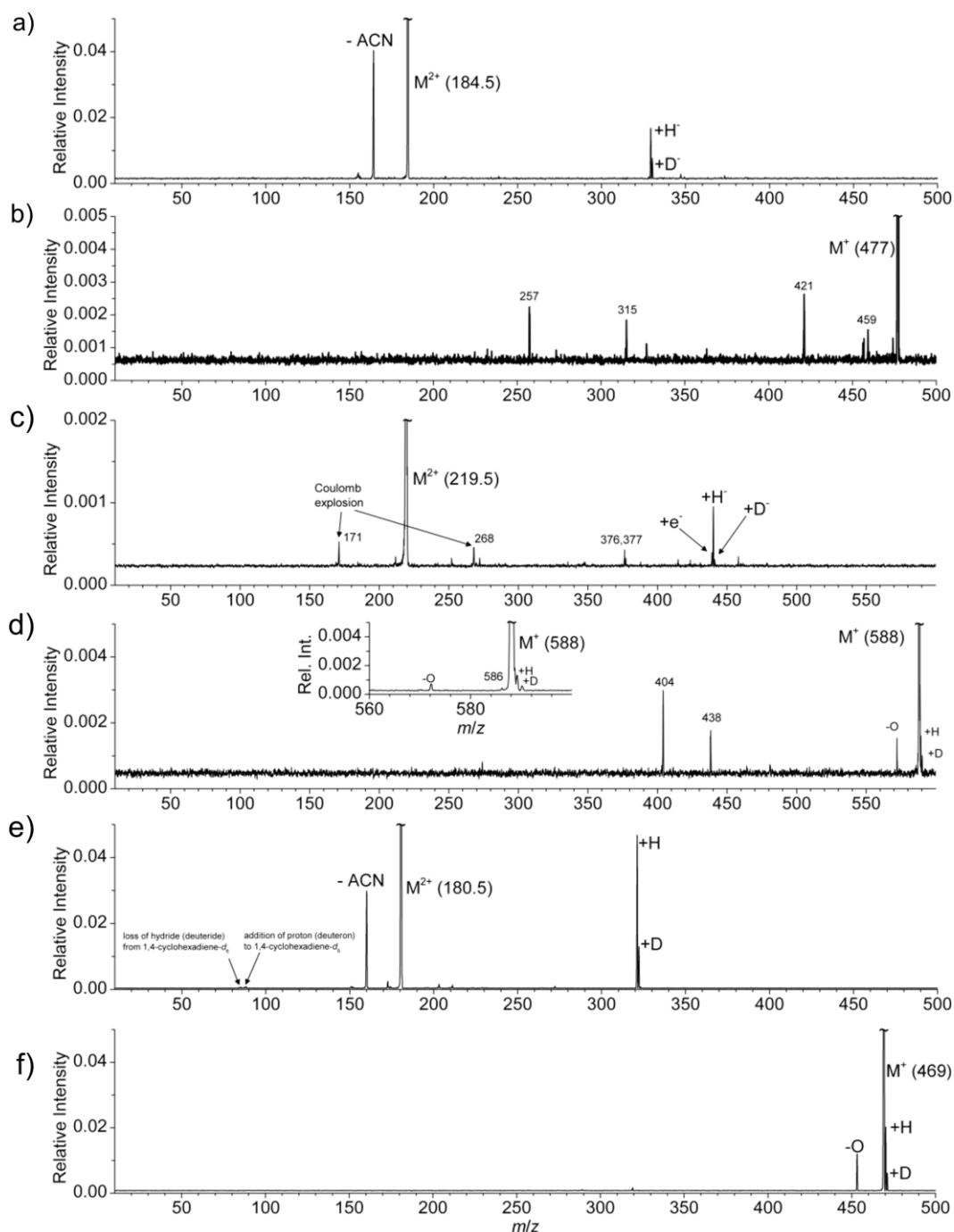


Figure 49. Mass spectrum of reactions at nominally zero collision energy: (a) $[(\text{TMC})\text{Fe}^{\text{IV}}(\text{O})(\text{ACN})]^{2+}$ (**1**) with 0.1 mTorr of 1,4-cyclohexadiene-1,2,3,4,5,6- d_6 , (b) $[(\text{TMC})\text{Fe}^{\text{IV}}(\text{O})(\text{OTf})]^+$ (**2**) with 0.3 mTorr of 1,4-cyclohexadiene-1,2,3,4,5,6- d_6 , (c) $[(\text{N4Py})\text{Fe}^{\text{IV}}(\text{O})]^+$ (**4**) with 0.1 mTorr of 1,4-1,2,3,4,5,6-cyclohexadiene- d_6 , (d) $[(\text{N4Py})\text{Fe}^{\text{IV}}(\text{O})(\text{OTf})]^+$ (**5**) 0.3 mTorr of with 1,4-cyclohexadiene-1,2,3,4,5,6- d_6 , (e) $[(\text{PyTACN})\text{Fe}^{\text{IV}}(\text{O})(\text{ACN})]^{2+}$ (**6**) with 0.1 mTorr of 1,4-cyclohexadiene-1,2,3,4,5,6- d_6 , (f) $[(\text{PyTACN})\text{Fe}^{\text{IV}}(\text{O})(\text{OTf})]^+$ (**7**) with 0.1 mTorr of 1,4-cyclohexadiene-1,2,3,4,5,6- d_6 . Asterisks denote products of reaction with background impurities.

To assess the effect of the spin state, I compared the reactivity of triplet/quintet complexes ${}^3\mathbf{8}_{\text{eq}}/{}^5\mathbf{8}_{\text{ax}}$, and ${}^3\mathbf{9}_{\text{eq}}/{}^5\mathbf{9}_{\text{ax}}$ (Table 4). I also determined the absolute reaction rates for the ${}^3\mathbf{8}_{\text{eq}}/{}^5\mathbf{8}_{\text{ax}}$ pair (Table 5). Apart from the spin state, the differences between the complexes may be attributed to the relative orientation of the Fe=O group and the pyridine ring. It was previously shown that the orientation of the oxo ligand perpendicular to the plane of the pyridine ligand can lead to increased reactivity.²³⁰ In section 3.3, we have also shown that the orientation of the oxo ligand perpendicular to the plane of the pyridine ligand stabilizes the quintet state. It was also previously reported that a change of the ligand *trans* to the oxo unit from an aliphatic amine to pyridine can lead to differences in reactivities for isospin iron complexes of an order of magnitude.²²⁸ However, in the PyTACN scaffold the ligand *trans* to the unit ligand is always aliphatic amine (irrespective of the studied stereoisomer; axial or equatorial). Therefore, the difference in the *trans* ligand cannot be the reason for the observed differences in reactivity between the stereoisomers of **8** and **9**.²³¹

Here, I will focus on discussing only the isomers of **8**; the situation for **9** is identical. As in other monocationic complexes, I observed two reaction channels: HAT from the allylic position of 1,4-cyclohexadiene and OAT (Figure 50). The reaction cross section is largest at nominally zero collision energy, which is characteristic of exothermic reactions proceeding via the formation of a collisional complex (Figure 50c).²³² The OAT channel does not show any isotope effect (for non-deuterated/deuterated cyclohexadiene), which confirms that it is an epoxidation reaction of the double bond and not HAT followed by OH rebound. Intramolecular KIEs for the HAT reaction are above 4 for both quintet and triplet complexes. This suggests that the mechanism involves the metal center, because abstraction by oxygen radical should have KIE value below 2.⁸⁹ Finally, both HAT and OAT reaction rates are slower for the triplet complexes, confirming their lower reactivity.

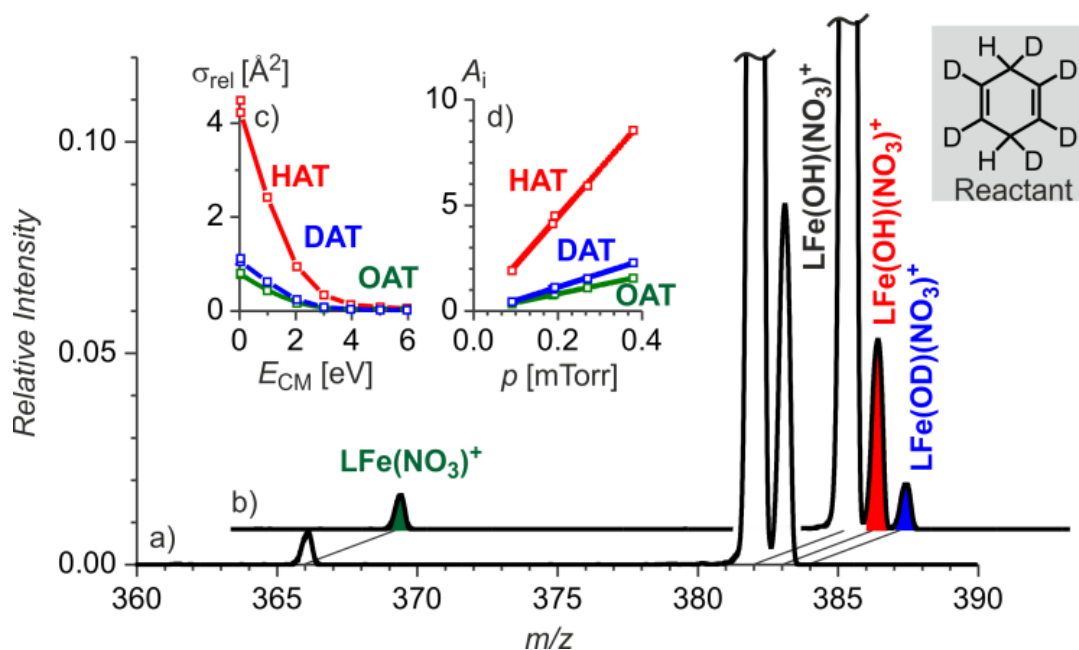


Figure 50. Mass spectra corresponding to the reaction of **8** (m/z 382, generated by in-source fragmentation) with (a) 1,4-cyclohexadiene and (b) 1,4-cyclohexadiene-1,2,3,4,5,6- d_6 ($p = 0.2$ mTorr). (c) Collision-energy dependence (center-of-mass) of the cross-sections σ and (d) pressure dependence of the relative cross section A of HAT, DAT, and OAT in the reaction with 1,4-cyclohexadiene-1,2,3,4,5,6- d_6 (A_i is defined as $-\ln(1 - \Sigma I_n / (\Sigma I_n + I_p))(I_i / \Sigma I_n)$, where I_n and I_p are intensities of the fragments and the parent, respectively).

Table 5. Experimental absolute reaction rates^a for HAT and OAT reactions of **8 with 1-4-cyclohexadiene-1,2,3,4,5,6- d_6 and 1,4-cyclohexadiene (*unlabeled CHD*).**

| Entry | L/X | from ^a | k_{HAT} (10^{-12} $\text{cm}^3 \text{s}^{-1}$) | k_{OAT} (10^{-12} $\text{cm}^3 \text{s}^{-1}$) | KIE |
|----------------|---|-------------------|---|---|-----------------|
| 1 | PyTACN/ NO_3 (8) | sol. | 6 ± 3 | 0.9 ± 0.4 | 4.13 ± 0.08 |
| | 8 + <i>unlabeled CHD</i> | sol. | 12 ± 3 | 0.9 ± 0.3 | |
| 2 | PyTACN/ NO_3 (8) | frag. | 9.9 ± 1.3 | 1.66 ± 0.19 | 4.07 ± 0.12 |
| | 8 + <i>unlabeled CHD</i> | frag. | 18.5 ± 1.2 | 1.61 ± 0.13 | |
| 3 ^b | $^3\mathbf{8}_{\text{eq}}$ | | 3.6 | 0.4 | |
| | $^3\mathbf{8}_{\text{eq}}$ + <i>unlabeled CHD</i> | | 7.9 | 0.5 | |
| 4 ^b | $^5\mathbf{8}_{\text{ax}}$ | | 13.3 | 2.3 | |
| | $^5\mathbf{8}_{\text{ax}}$ + <i>unlabeled CHD</i> | | 24.2 | 2.2 | |

^aAbsolute reaction rates were determined against the known reaction of $[\text{Fe}^{\text{III}}\text{O}]^+$ with CH_4 , see Section 2.4, Figures 17, 18 and 19.

^bThe reactivities of $^3\mathbf{8}_{\text{eq}}$ and $^5\mathbf{8}_{\text{ax}}$ were calculated assuming that the ions transferred from solution and the ions generated in the gas phase were present in the ratio 0.75:0.25 and 0.35:0.65, respectively.

^cRatio between the reaction rates of $^5\mathbf{8}_{\text{ax}}$ and $^3\mathbf{8}_{\text{eq}}$.

I have also measured reactivities of **7** and **10** generated in the gas phase by the nitrate cleavage. As mentioned above, for complex **10** this method leads to the ions with identical spectral characteristics as the ions transferred from the oxidized solution. In agreement, the reactivities of the ions generated in both ways are identical. We can easily rationalize this result based on the quantum chemical calculations. The perchlorate ligand preferentially occupies the axial position of the complex in both spin states (i.e. the oxo group is always in the equatorial position – ${}^3\mathbf{10}_{\text{eq}}$ and ${}^5\mathbf{10}_{\text{eq}}$ are the preferred spin-isomers). The CASPT2 calculations predict that the quintet state isomer ${}^5\mathbf{10}_{\text{eq}}$ is preferred in the gas-phase. Regardless, whether we generate the ${}^5\mathbf{10}_{\text{eq}}$ quintet in the gas phase or transfer the ${}^3\mathbf{10}_{\text{eq}}$ triplet state from the solution, we expect that due to the fast spin-isomerization at the iron center, we always detect the preferred spin-isomer (i.e. ${}^5\mathbf{10}_{\text{eq}}$).

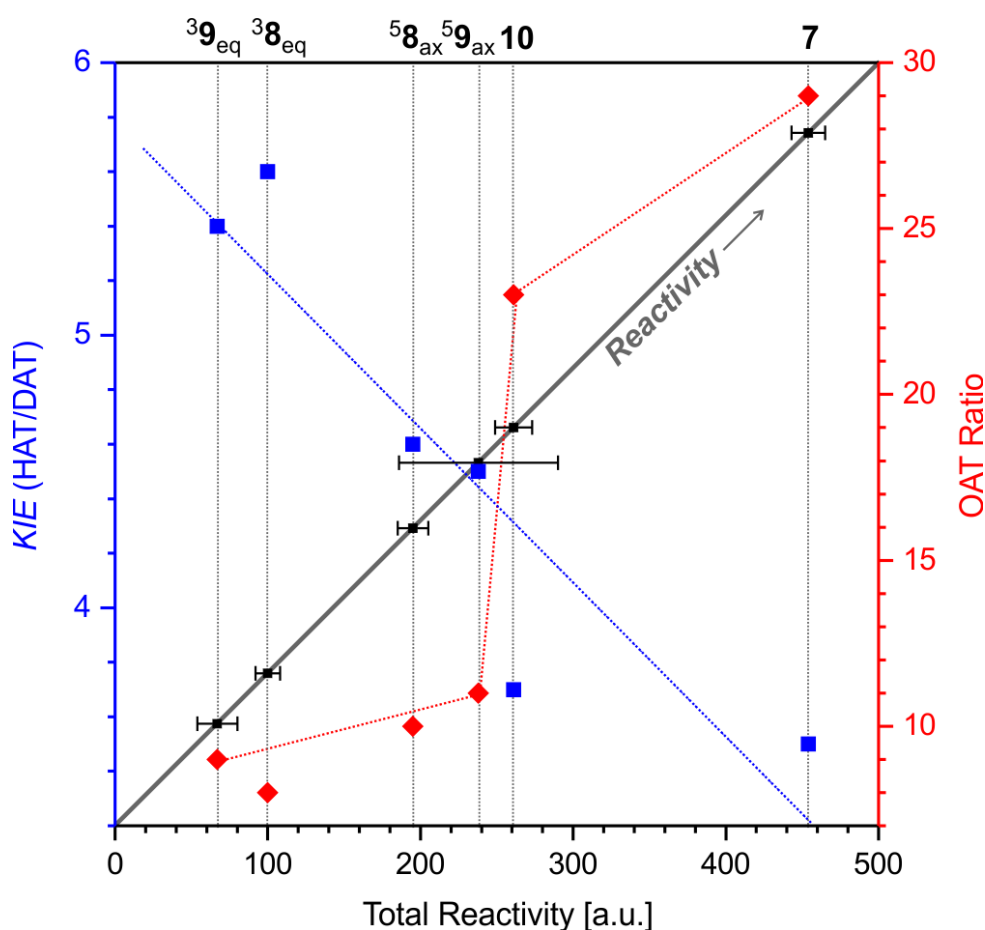


Figure 51. Comparison of gas-phase reactivity of complexes **7–10** with 1,4-cyclohexadiene-1,2,3,4,5,6- d_6 (see also Table 4). The error bars denote the standard deviation of the total reactivities. The dotted lines serve as a guide for eyes.

For the triflate-bound complex **7**, the reactivity of the ions generated by the gas-phase nitrate cleavage significantly drops. This is also in accordance with our spectroscopic experiments that showed that these ions are contaminated by the isomers with oxidized ligand. Triflate, similarly to perchlorate, always occupies the axial position. We have therefore the same situation as for **10**. We generate a mixture of $^3\mathbf{7}_{\text{eq}}$ and $^5\mathbf{7}_{\text{eq}}$ that rapidly spin-isomerizes to the preferred spin-state in the gas phase (the CASPT2 calculations predict both of the spin-isomers to be essentially at the same energy). We rationalize the drop in reactivity for the complexes generated by the nitrate cleavage by the large reactivity of the triflate complexes (compare with Table 4). The gas-phase generated ions are initially formed with a large excess of internal energy. Under the same conditions, we are able to cool the less reactive ions (**8**, **9**, and **10**) by collisional cooling with the sheath gas (N_2) before they undergo the internal oxidation. For complex **7**, the internal oxidation proceeds probably much faster and therefore a substantial amount of ions self-oxidizes before we are able to cool them to a low temperature.

Comparison of all PyTACN complexes **7–10** (Entries 6–13 in Table 4) is shown in Figure 51. The reactivities decrease in the following order: $\mathbf{7} > \mathbf{10} > ^5\mathbf{9}_{\text{ax}} > ^5\mathbf{8}_{\text{ax}} > ^3\mathbf{8}_{\text{eq}} > ^3\mathbf{9}_{\text{eq}}$. We could not spectroscopically assign the spin-isomers of **7** and **10**, however, based on CASPT2 calculations, they are most likely equatorial quintets. The quintet spin-isomers of **8** and **9** are more reactive than their triplet analogs. With the increasing reactivity the kinetic isotope effect for HAT clearly decreases. Further, the relative abundance of the OAT channel positively correlates with the total reactivity and it seems to be is much more sensitive to the nature of the anion ligand (**7** and **10** vs **8** and **9**) than to the spin-state of the complex.

3.5. Conclusions

We used helium tagging IR spectroscopy to characterize a set of benchmark iron(IV)-oxo complexes. We used ^{18}O labeling to determine their Fe=O stretching vibration frequencies. Moreover, by comparing the ligand vibrations, we could determine the spin state of studied iron(IV)-oxo complexes, when we had access to both spin isomers. Results show that the effect of the spin state on the Fe=O stretching frequency is negligible and the solvation by acetonitrile produces an average red-shift of 9 cm^{-1} . Furthermore, I performed reactivity studies of the complexes in different ligand geometry, charge state and spin state with 1,4-cyclohexadiene. I prepared two closely related isomers $^3\mathbf{8}_{\text{eq}}$ and $^5\mathbf{8}_{\text{ax}}$ that mainly differ in their spin state and enabled me to see the spin state effect directly – the quintet complexes were

about three times more reactive than their triplet counterparts. The effect of ligand variation (ACN vs anionic ligand) varies greatly by the relative position of the anion with respect to the iron-oxo unit. The greatest influence on reactivity was observed, when the anion was *trans* to the oxo unit. Therefore, the effect of the counterions present in solution must be carefully assessed, as the speciation can seriously affect reactivity of iron(IV)-oxo complexes in solution.

CHAPTER 4. Iron(III)-Oxo Complexes in the Gas Phase

This chapter is based on publication (3) as referenced in Prohlášení (Declaration) on page i.

4.1. Introduction

In the previous chapter, I established the link between the gaseous and condensed phase iron(IV)-oxo intermediates and showed that IRPD spectroscopy could be used to get relevant spectroscopic data for these compounds. However, using gas-phase techniques, we can also study compounds that cannot be prepared in solution. We decided to study iron(III)-oxo compounds that are products of one electron reduction of iron(IV)-oxo compounds. We were interested, whether the additional electron causes weakening of the iron-oxo bond and possibly makes these compounds more reactive (Figure 52).

We decided to study iron(III)-oxo compounds with different denticity of ligands (Figure 53), namely tetragonal $[(N4Py)Fe^{III}(O)]^+$ (**11**), trigonal $[(TPA)Fe^{III}(O)]^+$ (**12**), trigonal $[(TQA)Fe^{III}(O)]^+$ (**13**) and tetragonal $[(TMC)Fe^{III}(O)]^+$. The oxygen in **14** can be either *syn* or *anti* to the four TMC methyl groups (**14_{syn}**, **14_{anti}**).^{45, 233} I prepared the iron(III)-oxo complexes in the gas phase either by nitrate cleavage method from $[(L)Fe^{II}(ONO_2)]^+$ precursors (Equation (1) on page 18) or by one-electron reduction of $[(L)Fe^{IV}(O)]^{2+}$ complexes in collisions with tetrakis(dimethylamino)ethylene (Equation (2) on page 21). I also screened these complexes for reactivity with various substrates.

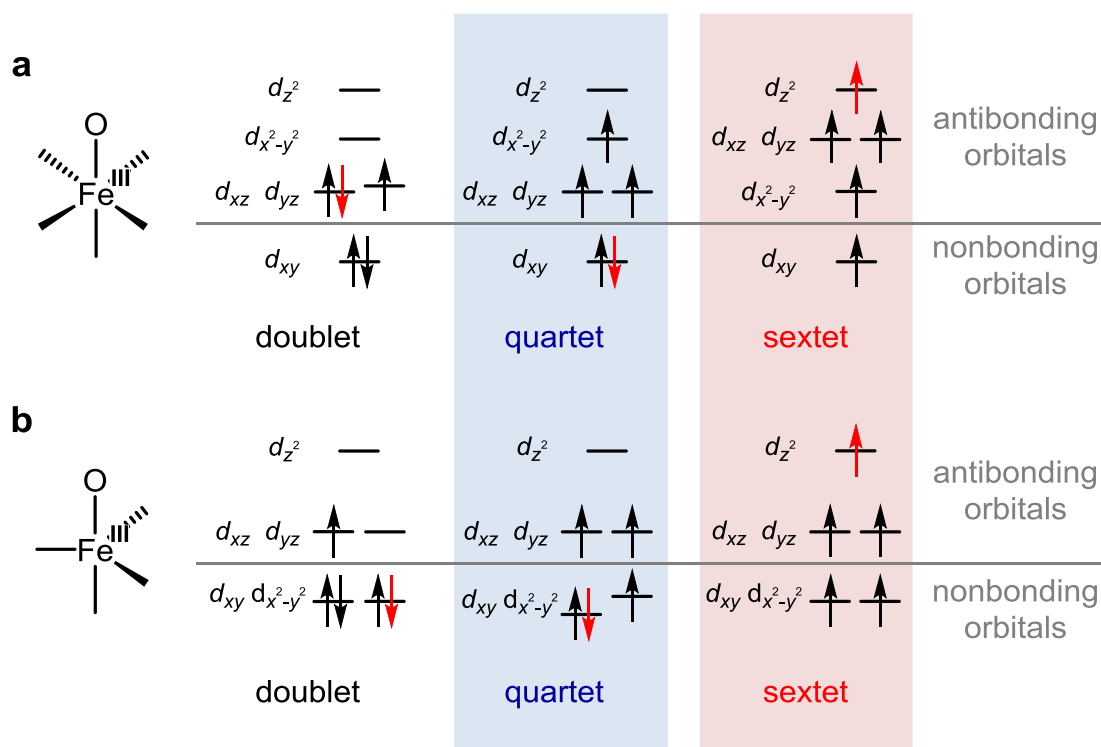


Figure 52. Possible electronic configurations of tetragonal (a) and trigonal (b) terminal iron(III)-oxo complexes. The reversed ordering between $d_{x^2-y^2}$ and d_{xz}/d_{yz} orbitals (a, sextet) results from my DFT calculations. The energy level splitting of d_{xz}/d_{yz} and $d_{xy}/d_{x^2-y^2}$ orbitals results from the Jahn-Teller distortion. The red arrow indicate the "added" electron from iron(IV)-oxo species.

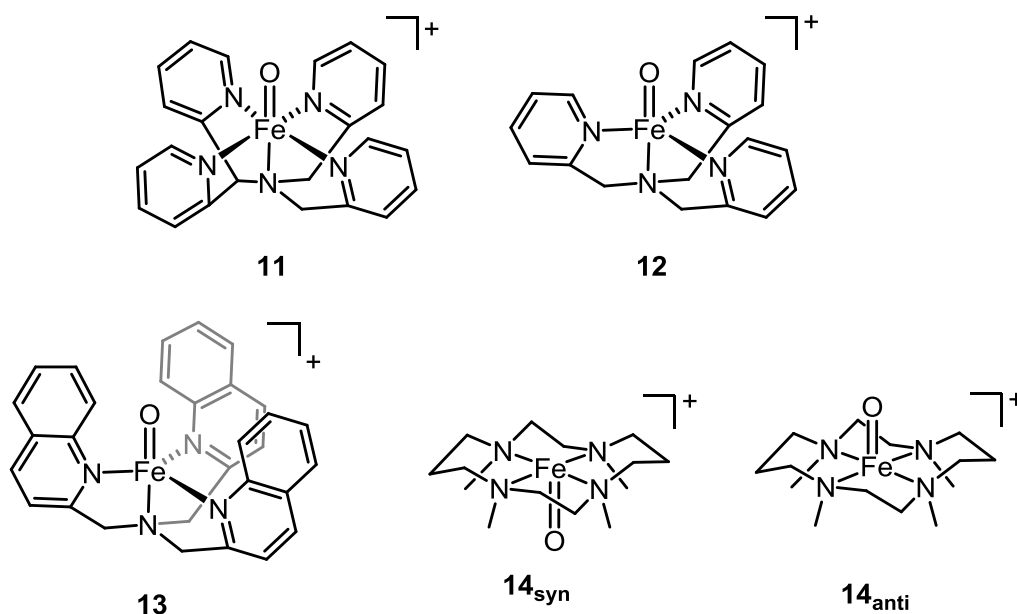


Figure 53. Studied iron(III)-oxo complexes.

4.2. IR and Vis Spectra of Iron(III)-Oxo Complexes

I prepared the tetragonal complex $[(\text{N4Py})\text{Fe}^{\text{III}}(\text{O})]^+$ (**11**) by the nitrate cleavage from $[(\text{N4Py})\text{Fe}^{\text{II}}(\text{NO}_3)]^+$ and it displays the Fe–O stretching vibration at 851 cm^{-1} , which shifts to 815 cm^{-1} with ^{18}O labeling (Figure 54a). The same species was also obtained by the TDAE reduction of the iron related iron(IV)-oxo complex $[(\text{N4Py})\text{Fe}^{\text{IV}}(\text{O})]^{2+}$ (**4**) and the spectrum of **11** prepared by this method is shown in Figure 54c. Unexpectedly, the Fe–O stretching frequency in **11** is only 2 cm^{-1} red shifted with respect to **4** (Figure 30). This suggests that the electron occupancies of the d orbitals with the Fe–O antibonding character (d_{xz} , d_{yz} and d_z^2) are identical for **11** and **4**. The only electronic configuration where their occupancies do not change is the quartet state (Figure 52a, middle panel). In this case, the electron goes in the ligand σ -antibonding $d_{x^2-y^2}$ orbital. Note that N4Py ligand vibrations in Figure 54a are also best matching with the DFT prediction for the quartet state in Figure 54b. We confirmed this assignment by measurement of the electronic absorption spectrum of **11** (Figure 55a). The spectrum shows intense absorption with a maximum at 450 nm and a broad band between 580 and 610 nm. This band structure agreed with theoretical TD-DFT prediction for the quartet state (Figure 55f). According to the TD-DFT, these intense transitions correspond to metal-to-ligand charge transfers (MLCT) from a doubly occupied d_{xy} orbital to π^* orbitals of pyridine rings. The quartet state is also consistent with the DFT energetics, because even though the B3LYP functional predicts the ground state of **11** as sextet, the quartet state is only 0.8 kcal mol^{-1} higher, well within the accuracy of DFT methods.

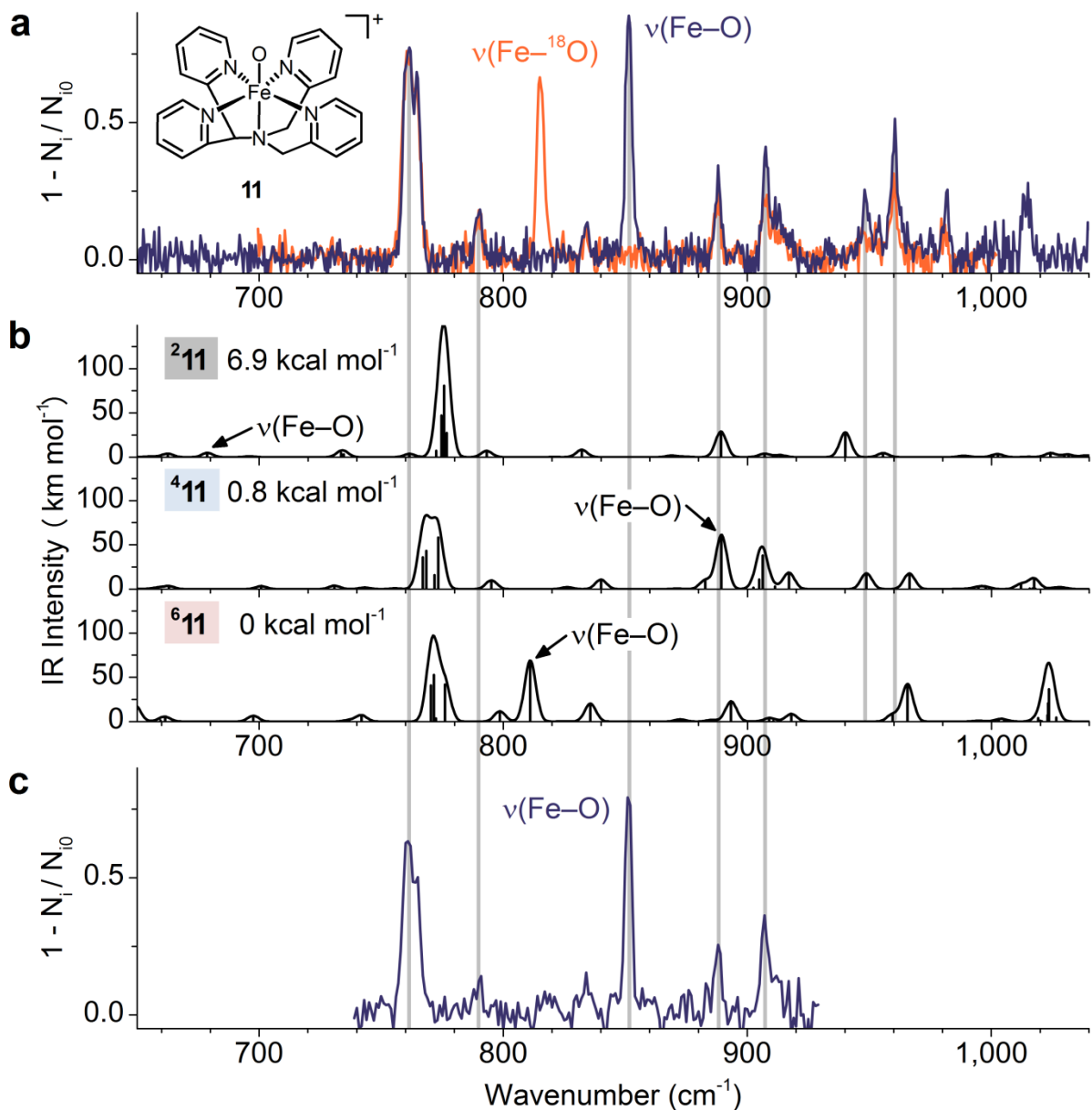


Figure 54. (a) IRPD spectrum of **11**. Blue and orange traces correspond to ^{16}O and ^{18}O labeling of the oxo ligand, respectively. (b) Theoretically predicted IR spectra calculated at B3LYP-D3/6-311+G** level of theory, broadened with Gaussians (FWHM 5 cm^{-1}). Theoretical vibrational frequencies were scaled by 0.99. The relative DFT energies include zero-point energy corrections at the same level of theory. (c) IRPD spectrum of **11** prepared by one-electron reduction of the corresponding iron(IV)-oxo complex in the gas phase by tetrakis(dimethylamino)ethylene.

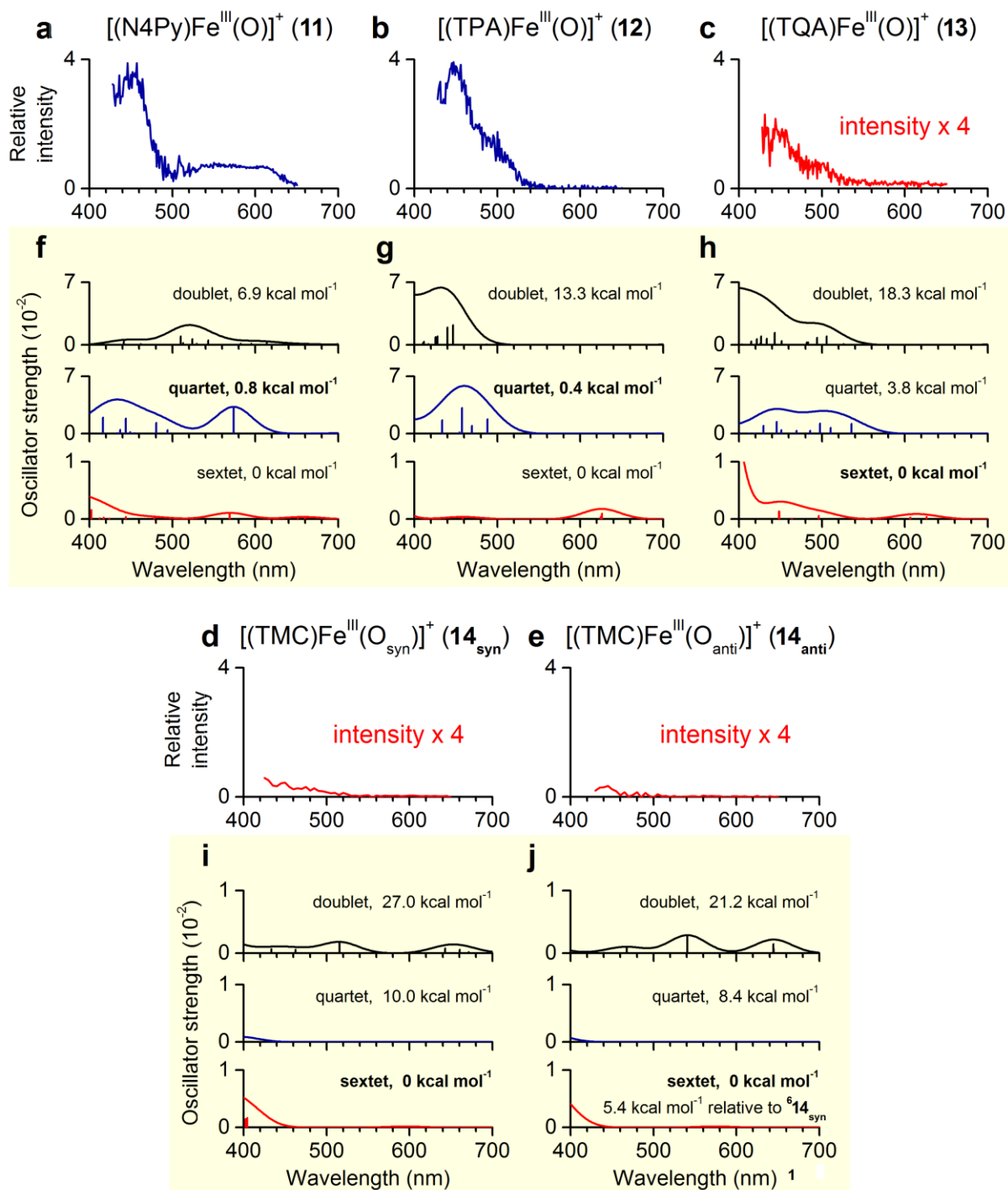


Figure 55. (a–e) Experimental visible photodissociation spectra of complexes **11**–**14** measured at 3 K and (f–j) theoretical TD-DFT spectra of complexes **11**–**14**. The assigned ground states are highlighted in bold. The relative DFT energies include zero-point energy corrections.

The Fe–O band of the "trigonal" (it is more precise to talk about trigonal symmetry of the ligand) complex [(TPA)Fe^{III}(O)]⁺ (**12**) is located at 856 cm⁻¹ and shifts to 820 cm⁻¹ with ¹⁸O labeling (Figure 56a). It is at a quite similar position to complex **11**, despite the different denticity of their supporting ligands. The IR spectrum best matches the spectrum predicted for the quartet state (Figure 56b). The DFT calculations again suggest that the quartet and sextet states of **12** are almost isoenergetic, whereas the doublet spin state is much higher in energy and can be thus excluded. The experimental vis spectrum (Figure 55b) shows a strong absorption band at 450 nm with a shoulder at 500 nm. This is best reproduced, again with the TD-DFT prediction for the quartet state (Figure 55g). TD-DFT predicts, that the observed bands correspond to MLCT transitions from a d_{xy} orbital to π* orbitals of the pyridine rings, similarly to **11**. Moreover, while we measured the IR spectrum, we found additional electronic transition in the IR range (Figure 57). This absorption ranges from 1650 to 4000 cm⁻¹ and peaks around 2200 cm⁻¹. Such absorption is predicted in the TD-DFT calculations of the quartet state at 4300 cm⁻¹ and corresponds to a spin-allowed d-d transition, which is not present in the sextet state (note that TD-DFT calculations also predicted the other quartet-state complex, **11**, to feature a similar d-d transition located at 10800 cm⁻¹, however, this frequency range is not accessible with our current IR laser setup). To sum up, IR and vis data show, consistently with DFT and TD-DFT predictions, that the ground state of **12** is a quartet, with Fe–O band position and vis spectrum similar to **11**.

The position of the Fe–O stretching band in the second trigonal complex [(TQA)Fe^{III}(O)]⁺ (**13**) is 777 cm⁻¹ (746 cm⁻¹ with ¹⁸O labeling; Figure 58a). This is a sizeable decrease in frequency by ~75 cm⁻¹ from the quartet complexes **11** and **12**. Therefore, the occupation of the Fe–O antibonding orbitals must have changed and the spin state must be either doublet or sextet. The doublet state, however, lies 17.6 kcal mol⁻¹ higher than the sextet state according to my DFT calculations. Also, the band at 970 cm⁻¹, which is characteristic for the sextet state (Figure 58c and similar in Figure 56c), is present. These observations are consistent with the sextet state as the ground state of **13**, in which all d orbitals, including the Fe–O σ*-antibonding d_z² orbital, are singly occupied (Figure 52a, right panel). Hence, the formal Fe–O bond order in the sextet state decreases to 1.5. The sextet ground state assignment also matches the visible spectrum (Figure 55c). First, the absorption intensity of **13** is approximately eight times lower than that of complex **12**, which corroborates the theoretical prediction for a sextet state (Figure 55h). Second, the absorption spectrum displays two maxima at 450 and 500 nm and a weak but reproducible broad absorption at

longer wavelengths. According to TD-DFT, the observed absorptions correspond to predominantly spin-forbidden d-d transitions, which causes their low intensity. Together, our data support the sextet state assignment for complex **13**. The difference in the spin state from **12** is likely caused by the interaction between the quinoline hydrogens with the iron-oxo unit.

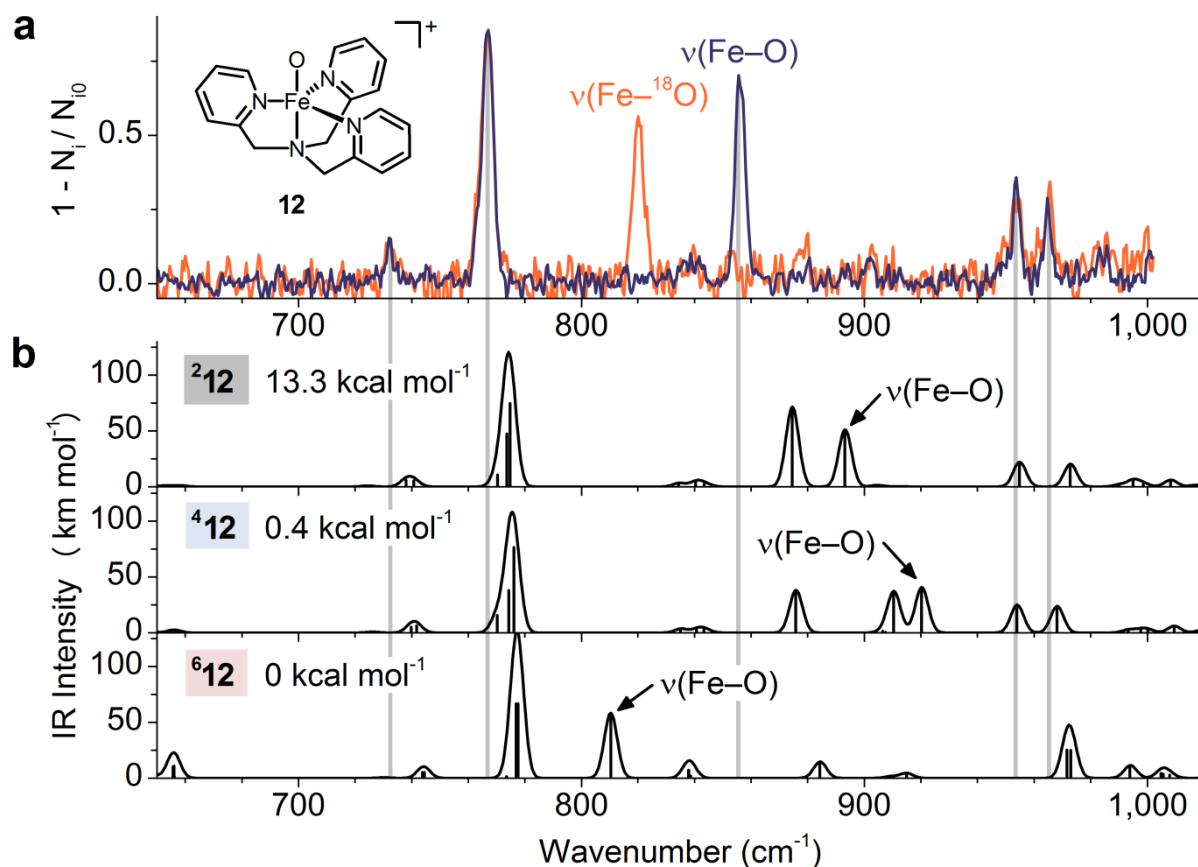


Figure 56. (a) IRPD spectrum of **12**. Blue and orange traces correspond to ¹⁶O and ¹⁸O labeling of the oxo ligand, respectively. (b) Theoretically predicted IR spectra calculated at B3LYP-D3/6-311+G** level of theory, broadened with Gaussians (FWHM 5 cm⁻¹). Theoretical vibrational frequencies were scaled by 0.99. The relative DFT energies include zero-point energy corrections. Please note, that in this case, DFT wrongly predicts the ground state of **12**, which we assigned as quartet based on experimental data.

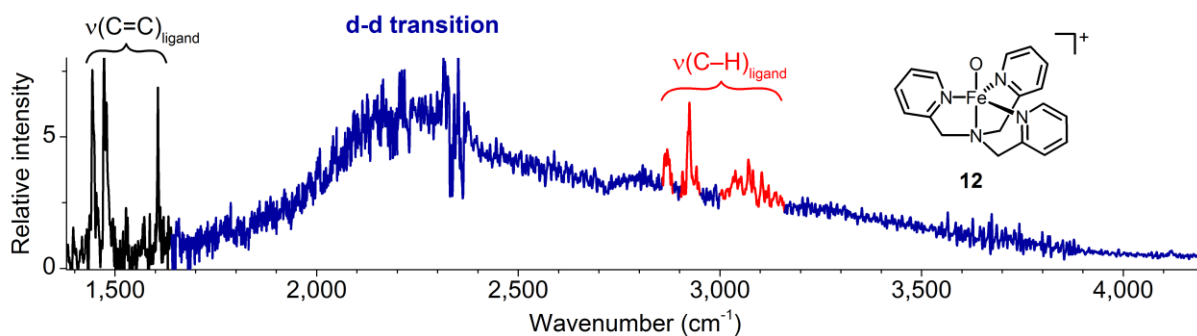


Figure 57. (a) IRPD spectrum of spectrum of **12** measured at 3 K in infrared region containing an electronic d-d transition. The spectrum also contains C=C and C-H stretching vibrations of the TPA ligand. The latter vibrations (highlighted in red) are superimposed on the electronic absorption band.

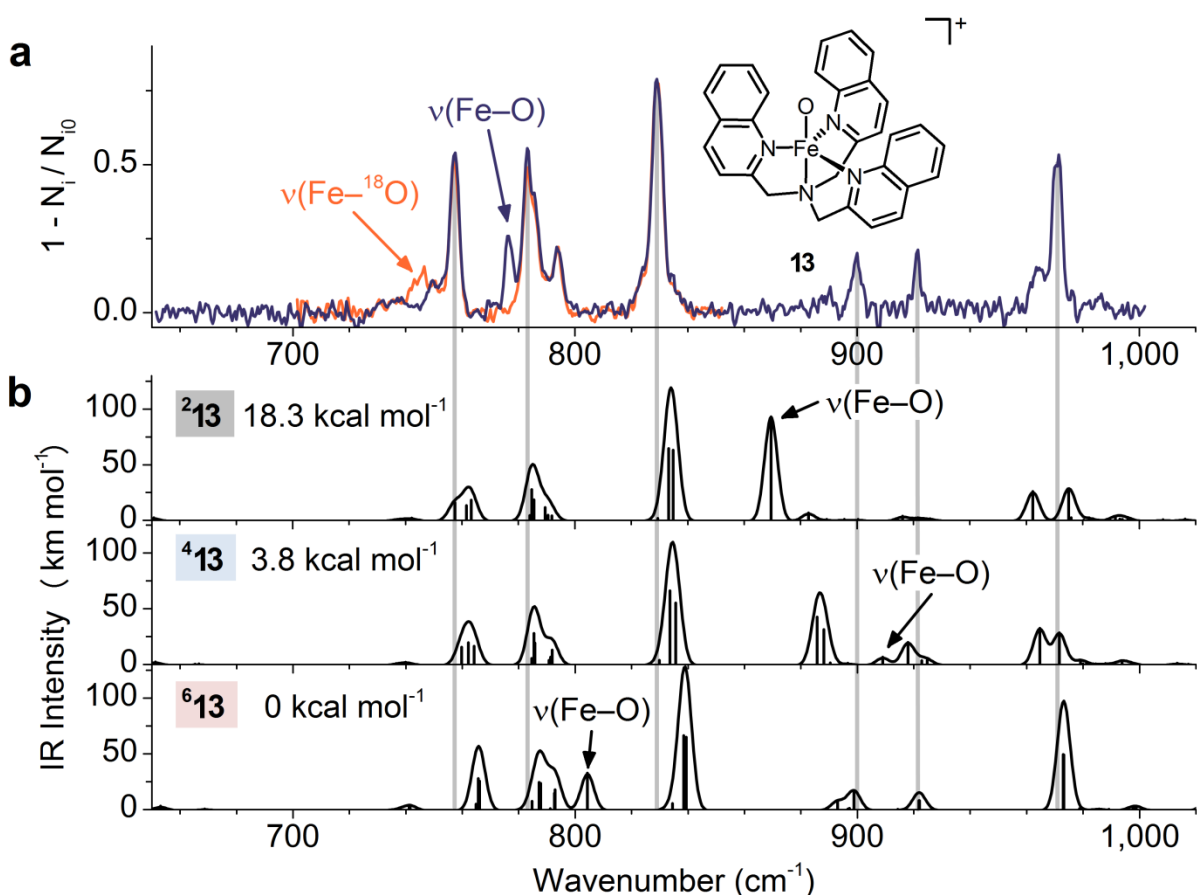


Figure 58. (a) IRPD spectrum of **13**. Blue and orange traces correspond to ^{16}O and ^{18}O labeling of the oxo ligand, respectively. (b) Theoretically predicted IR spectra calculated at B3LYP-D3/6-311+G** level of theory, broadened with Gaussians (FWHM 5 cm^{-1}). Theoretical vibrational frequencies were scaled by 0.99. The relative DFT energies include zero-point energy corrections.

Lastly, we also studied the tetragonal [(TMC)Fe^{III}(O)]⁺ (**14**) complexes. These are iron(III)-oxo complexes with the TMC ligands, where the four methyl groups are either *syn* or *anti* to the oxo ligand. We prepared both of them, as evidenced by the distinct spectra obtained from the nitrate cleavage and the TDAE reduction (compare panels a and c in Figure 59).

In the nitrate cleavage method, the iron(II) precursor of **14**_{syn} most likely bears the nitrate ligand at the *syn* face to the four methyl groups, as found in all five known crystal structures of [(TMC)Fe^{II}(X)]⁺ complexes reported thus far.^{60,234–238} Accordingly, the oxo ligand was expected to be bound to the *syn* face as well. The experimental spectrum of **14**_{syn} supports this prediction. The predictions for the *anti* isomer feature strong C–H deformation bands at about 990 cm⁻¹ (Figure 59c). This is indeed confirmed by the spectrum of **14**_{anti}, prepared by one-electron reduction (and the expulsion of acetonitrile from the built-up internal energy) of the corresponding iron(IV)-oxo complex (the iron(IV)-oxo is known to be *anti*, when prepared by our oxidation method).⁴⁵

We anticipated that the vacant axial coordination site would make the σ*-antibonding d_z² orbital energetically accessible in TMC complexes and enable the sextet ground state configuration, despite tetragonal symmetry. Indeed, we observed the Fe–O bands at 797 cm⁻¹ and at 769 cm⁻¹ for **14**_{syn} and for **14**_{anti}, respectively (Figure 59a,c). These bands shifted to 763 cm⁻¹ and 732 cm⁻¹ with ¹⁸O labeling. Accordingly, my DFT calculations predicted a sextet ground state for **14**_{syn} and **14**_{anti}, with the quartet and doublet states being more than 8 kcal mol⁻¹ higher in energy. Furthermore, the weak absorption in the vis spectra of **14**_{syn} and **14**_{anti} is inconsistent with the doublet states. (cf. Figure 55d,e with Figure 55i,j). However, vis spectra do not exclude neither quartet, nor sextet state. We assign sextet ground states to **14**_{syn} and **14**_{anti} based on Fe–O frequencies and on relative energetic stabilities, in comparison with other spin states.

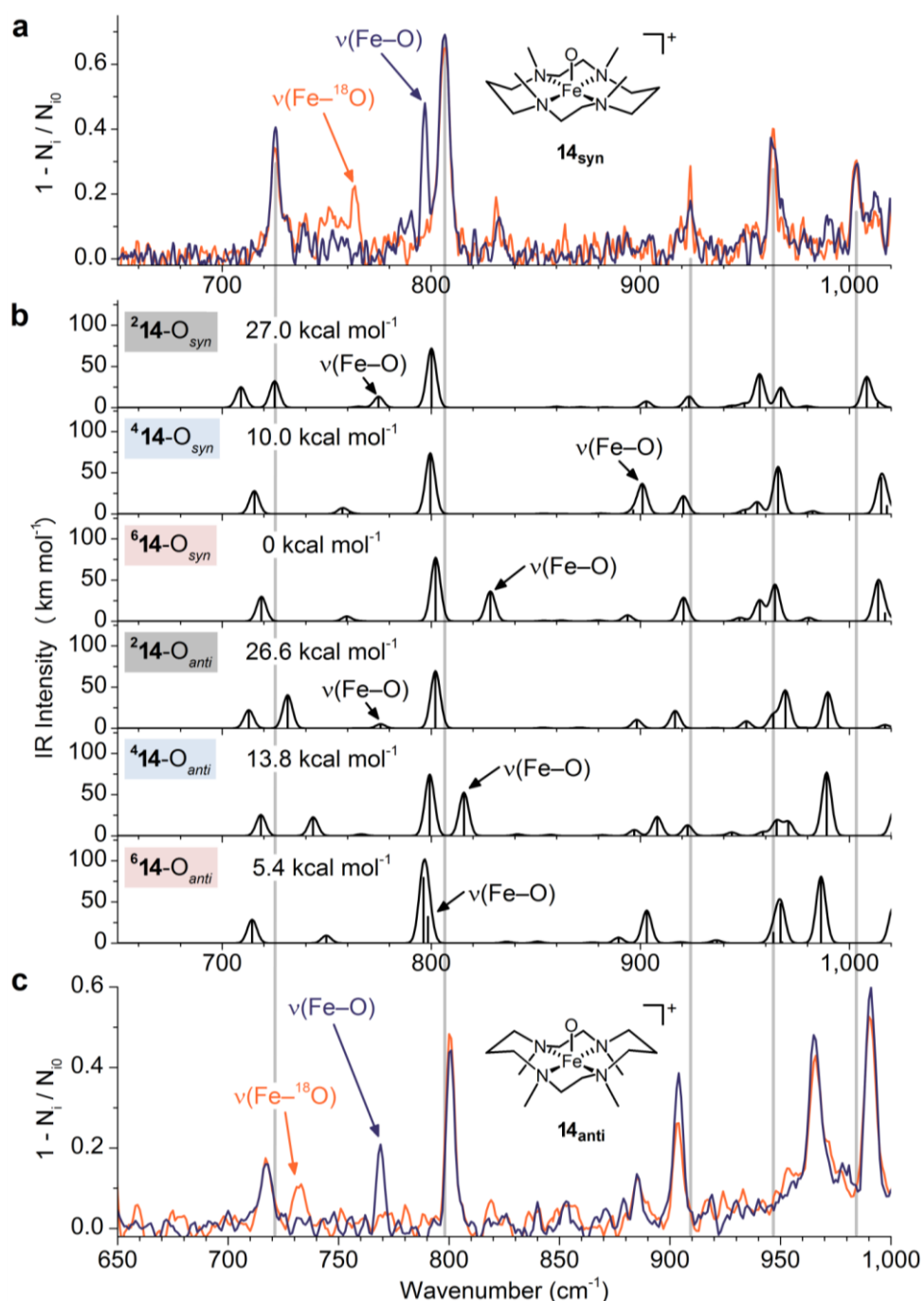


Figure 59. (a) IRPD spectrum of $\mathbf{14}_{syn}$; region between 700 and 850 cm^{-1} was measured with 2x longer irradiation time compared to the rest of the spectrum. Blue and orange traces correspond to ^{16}O and ^{18}O labeling of the oxo ligand, respectively. (b) Theoretically predicted IR spectra calculated at B3LYP-D3/6-311+G** level of theory, broadened with Gaussians (FWHM 5 cm^{-1}). Theoretical vibrational frequencies were scaled by 0.99. The relative DFT energies include zero-point energy corrections. (c) IRPD spectrum of $\mathbf{14}_{anti}$, which was prepared by one-electron reduction of the corresponding iron(IV)-oxo complex in the gas phase by tetrakis(dimethylamino)ethylene.

4.3. Effect of the Hydrogen Bonding

In section 3.3 we established, that the Fe–O vibrations in the iron(IV)-oxo complexes in the gas phase, are not unaffected by their spin state and similar results were also observed by others in solution.^{65,66,67} This is readily rationalized by looking at the electronic configuration of quintet vs. triplet iron(IV)-oxo complexes: whereas the configuration of triplet complexes is $(d_{xy})^2 (d_{xz})^1 (d_{yz})^1$, the configuration of quintet complexes is $(d_{xy})^2 (d_{xz})^1 (d_{yz})^1 (d_{x^2-y^2})^1$. They only differ in occupancy of the organic ligand σ^* -antibonding $d_{x^2-y^2}$ orbital and not in occupancies of the Fe–O antibonding d_{xz} , d_{yz} , or d_z^2 orbitals.

On contrary, as we showed in the previous section, the Fe–O stretching frequency in iron(III)-oxo complexes is mostly determined by their spin state. The Fe–O stretching frequencies of the studied quartet complexes **11**, **12** were in the same range ($\sim 850\text{ cm}^{-1}$) as for the iron(IV)-oxo complexes, as they only differ from the in the occupancy of Fe–O nonbonding d_{xy} or $d_{x^2-y^2}$ orbitals from quintet/triplet iron(IV)-oxo complexes, respectively. However, the sextet state complexes **13**, **14_{syn/anti}** showed weakened Fe–O bond, because the added electron was placed into the Fe–O antibonding d_z^2 orbital. Therefore, their Fe–O stretching frequencies were around 70 cm^{-1} red shifted with respect to iron(IV)-oxo complexes. These results are summarized in Table 6. Nevertheless, the Fe–O frequencies of the sextet complexes **13**, **14_{syn}** and **14_{anti}** are still blue-shifted by $\sim 100\text{ cm}^{-1}$ in comparison with Borovik's sextet complex $[(\text{H}_3\text{buea})\text{Fe}^{\text{III}}(\text{O})]^{2-}$ (671 cm^{-1}).⁴¹ Therefore, we suspected that this additional shift must result from the three hydrogen bonds to the Fe–O group formed by the amide N–H groups of the H₃buea ligand.²³⁹

Table 6. The Fe–O vibrational frequencies (ν) of iron(IV)-oxo and iron(III)-oxo complexes.

| Supporting ligand | $\nu(\text{Fe}^{\text{IV}}\text{-O})$ (cm^{-1}) ^a [¹⁸ O labeling shift] (spin state) | $\nu(\text{Fe}^{\text{III}}\text{-O})$ (cm^{-1}) ^a [¹⁸ O labeling shift] (spin state) |
|---|--|---|
| N4Py (1) | 853 [-34] ($S = 1$) <i>841 [-35]</i> ¹³⁸ | 851 [-36] ($S = 3/2$) |
| TPA (2) | 833 [-34] ²⁴⁰ ($S = 1$) ^b | 856 [-36] ($S = 3/2$) |
| TQA (3) | <i>838 [-35]</i> ⁵⁶ ($S = 2$) ^b | 777 [-31] ($S = 5/2$) |
| TMC _{syn} (4_{syn}) | <i>856 [-36]</i> ²³³ ($S = 1$) ^b | 797 [-34] ($S = 5/2$) |
| TMC _{anti} (4_{anti}) | 848 [-34] ($S = 1$) <i>834 [-34]</i> ^{60,b} | 769 [-37] ($S = 5/2$) |
| H ₃ buea | 798 [-33] ²⁴¹ ($S = 2$) | <i>671 [-26]</i> ($S = 5/2$) ⁴¹ |

^aValues in italics were recorded in solution, spin states are given in parentheses.

^bIn solution, the complex likely has additional acetonitrile ligand.

To assess the effect of hydrogen bonding, we took advantage of the spontaneous formation of water adducts in the cold trap of the ISORI instrument and prepared complexes of **11**, **12** and **13** with a single water molecule in the ion trap. Figure 60a,c,e shows the IRPD spectra of singly hydrated complexes **11**•H₂O, **12**•H₂O and **13**•H₂O, respectively. We also attempted to generate **14**•H₂O, but we were unable to generate a sufficient number of helium-tagged ions to measure the IRPD spectrum. There are multiple possible binding modes for the water molecule. In the case A, the water molecule would either be only loosely bound to the complex (like the triflate in **5**), or coordinated to iron center via oxygen atom. In such a case, the neither O–H group of the water molecule would be significantly affected and we should observe two O–H stretches around 3700 cm^{-1} . In the case B, the water can be hydrogen-bonded to the Fe–O unit (no other hydrogen bond acceptors are present in complexes **11**–**13**). In this case, we should see only one O–H stretch around 3700 cm^{-1} and one O–H stretch red-shifted and possibly broadened^{242,243} due to hydrogen bonding. In the case C, the water would be deprotonated by the Fe–O unit, forming iron(III)-hydroxide. The resulting OH⁻ anion could coordinate to any vacant coordination sites on the iron center. This would result in IR spectrum similar to case A, except for the fact, that one of the hydrogen would be bound to the oxygen from the iron-oxo unit. Therefore, one of the O–H stretches should shift with the ¹⁸O labeling of the Fe–O unit.

Comparison of spectra of **11**•H₂O with that of **11** (Figure 60a,b) reveals the presence of one additional free O–H band located at 3705 cm^{-1} that does not shift upon ¹⁸O labeling of

the Fe–O unit and a broad band around 3000 cm⁻¹. We attribute this broad band to the O–H stretching vibration of the hydrogen-bonded water molecule. Such red shift in O–H stretching vibration indicates a strong interaction between the water molecule and the Fe–O unit. We can therefore see, that the iron(III)-oxo complex **11** forms hydrogen bond to the water molecule through the Fe–O unit. This behavior is also shown in complex **12** (Figure 60c,d). The hydrogen bond also affects the Fe–O stretching vibrations in both complexes. The Fe–O stretching frequency red-shifts from 851 cm⁻¹ (**11**) to 787 cm⁻¹ (**11**•H₂O; $\Delta = -64$ cm⁻¹) and from 856 cm⁻¹ (**12**) to 787 cm⁻¹ (**12**•H₂O; $\Delta = -69$ cm⁻¹). These Fe–O stretching frequencies are close to the Fe–O stretching frequencies observed in sextet complexes **13**, **14**_{syn} and **14**_{anti}. Therefore, we measured their visible spectra, which are good indicators of the spin state (cf. Figure 55). The vis spectra of both hydrated complexes **11**•H₂O and **12**•H₂O (Figure 61) show a twentyfold decrease in absorption intensity compared with **11** and **12**, respectively. These results suggest a change in the spin state of **11** and **12** upon hydrogen bonding with water. Accordingly, my DFT calculations show that the hydrogen bond in **11**•H₂O and **12**•H₂O stabilizes the sextet over the quartet states (energies are shown Figure 61). A similar effect of hydrogen bonding on the spin state was previously reported for an iron(III) porphyrin chlorido complex.²⁴⁴ Thus, hydrogen bonding changes the spin state of **11** and **12** from quartet to sextet.

The higher stabilization of the sextet states of iron(III)-oxo complexes **11**•H₂O and **12**•H₂O by hydrogen bonding can be rationalized theoretically.²⁴⁵ Natural population analysis²²⁷ of **11**–**14** shows that the Fe–O bond is more polarized (oxygen carries a larger negative charge) in the sextet than in the quartet states (Table 7). Therefore, the complexes form stronger hydrogen bonds in the sextet states and are more energetically stabilized by hydration than in the quartet states. The difference in stabilization by hydrogen bonding is sufficient to change the ground spin state of **11** and **12** due to small energy differences between the quartet and the sextet states.

The Fe–O stretching frequencies of **11**•H₂O and **12**•H₂O (787 cm⁻¹) are located between the Fe–O stretching frequencies of **13**, **14**_{syn} and **14**_{anti} (777 cm⁻¹, 797 cm⁻¹, 769 cm⁻¹). This indicates that the major factor influencing the Fe–O frequency, in **11**•H₂O and **12**•H₂O, is the spin state change. We can thus still only speculate, whether the shift of additional 100 cm⁻¹ in [(H₃buea)Fe^{III}(O)]²⁻ complex,^{41,239} which has an Fe–O vibrational frequency of 671 cm⁻¹, is caused by the highly electron-donating ligand or the presence of geometrically enforced additional hydrogen bonds.

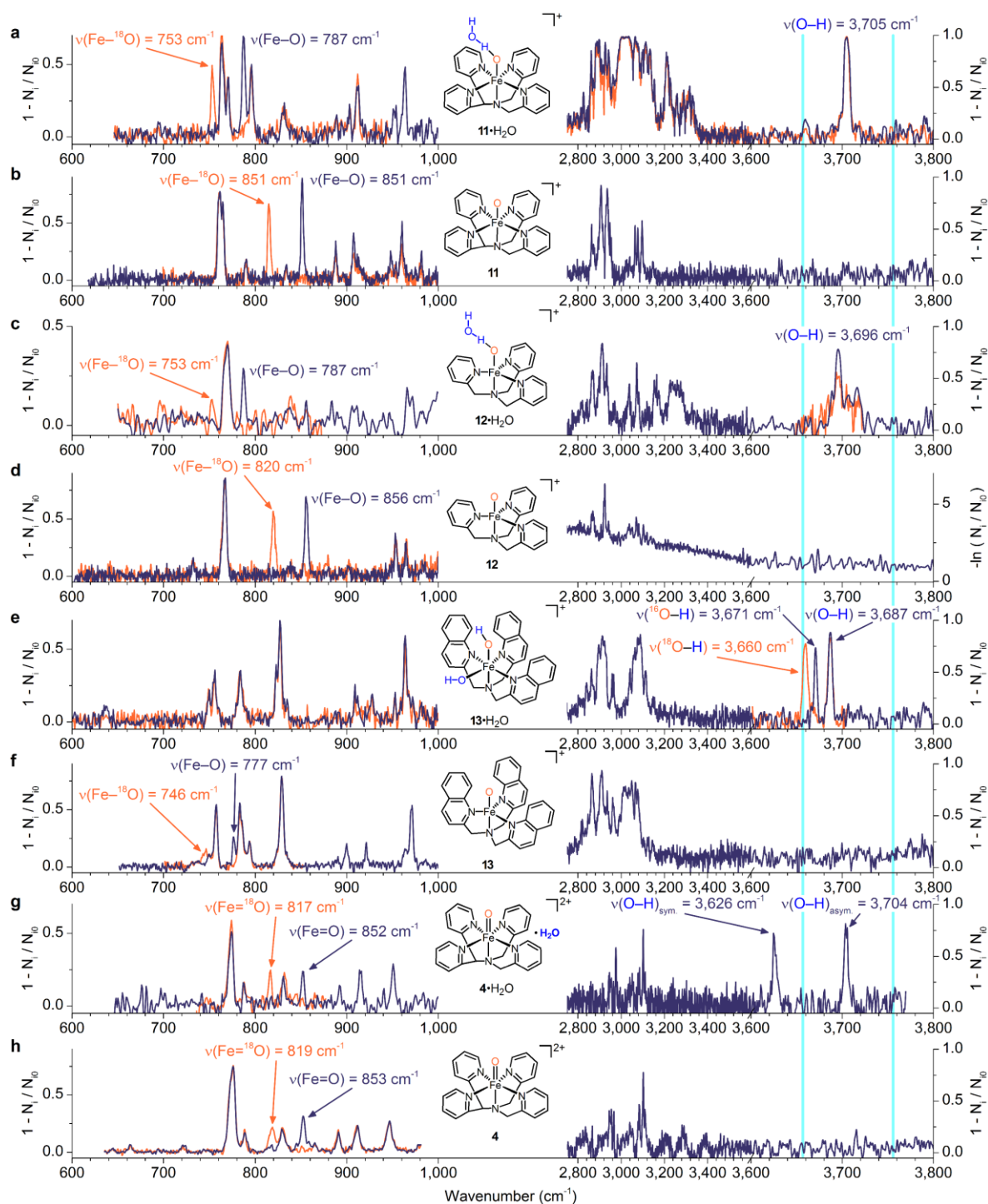


Figure 60. Comparison of infrared photodissociation spectra between singly-hydrated complexes (a) $11 \cdot \text{H}_2\text{O}$, (c) $12 \cdot \text{H}_2\text{O}$, (e) $13 \cdot \text{H}_2\text{O}$ and (g) $4 \cdot \text{H}_2\text{O}$ and non-hydrated complexes (b) **11**, (d) **12**, (f) **13** and (h) **4**. Orange traces correspond to ^{18}O labeling of the oxo ligand. Two light blue lines represent the frequency of symmetric (3657 cm^{-1}) and antisymmetric (3756 cm^{-1}) free O–H vibrations of water vapor (taken from Ref. 246). Please note, that the spectrum of **4** is slightly blue-shifted ($\sim 1\text{-}2 \text{ cm}^{-1}$) due to inaccurate calibration of the laser.

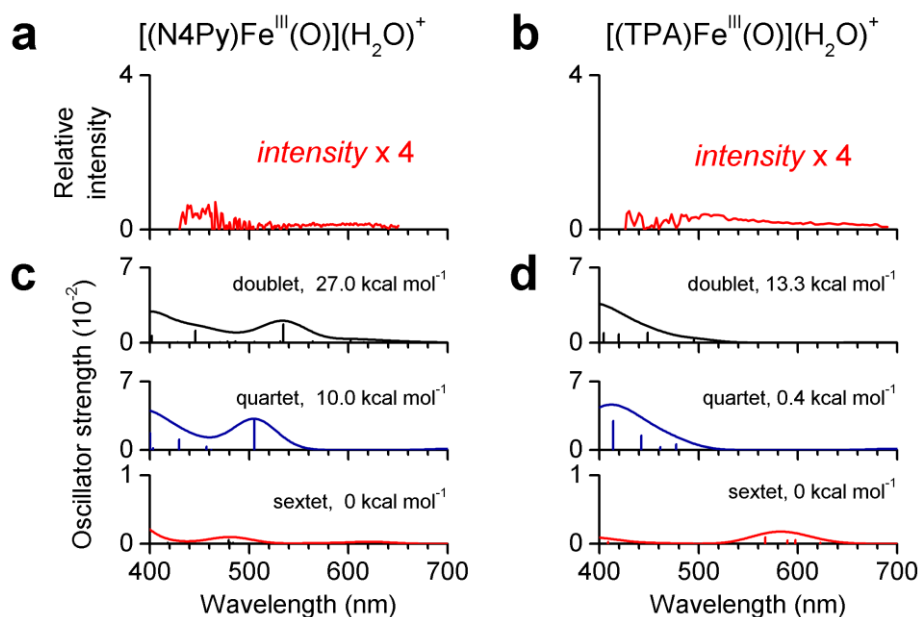


Figure 61. Experimental visible photodissociation spectra of (a) **11**•H₂O and (b) **12**•H₂O measured at 3 K. Theoretical TD-DFT spectra (c) **11**•H₂O and (d) **12**•H₂O. We assigned the ground states of both **11**•H₂O and **12**•H₂O as sextets based on the absorption profiles and intensities and relative energetic stabilities. The relative DFT energies include zero-point energy corrections.

Table 7. Natural charges in complexes 11–14 calculated at B3LYP-D3/6-311+G level.**

| Complex | quartet state | | sextet state | |
|---------------------------|---------------|----------|--------------|----------|
| | charge Fe | charge O | charge Fe | charge O |
| 11 | 0.67 | -0.58 | 1.00 | -0.77 |
| 12 | 0.75 | -0.57 | 1.07 | -0.74 |
| 13 | 0.85 | -0.64 | 1.16 | -0.82 |
| 14 _{syn} | 0.94 | -0.67 | 1.15 | -0.85 |
| 14 _{anti} | 0.85 | -0.75 | 1.11 | -0.87 |

The formation of water complex of **13** would be a suitable test to see the effect of the hydrogen bonding separate from the effect of the spin state change induced by the hydrogen bonding, because **13** is, unlike **11** and **12**, already in the sextet state. However, IRPD spectra of **13**•H₂O show two free O–H stretching bands at 3671 cm⁻¹ and 3687 cm⁻¹ (Figure 60e), one of which shifts with the ¹⁸O labeling of the Fe–O unit by -11 cm⁻¹, consistent with the prediction for O–H diatomic oscillator (-12 cm⁻¹). Moreover, no Fe–O stretching vibration is seen in **13**•H₂O. All these results are consistent with the formation of iron(III)-dihydroxo complex. Note that partial formation of such dihydroxo complex might be also occurring in

the spectrum of **12**•H₂O. The Fe–OH vibrations are not present in the spectrum because their frequencies lie outside the range of our laser system (i.e. below 595 cm⁻¹).

We also tested the effects of water solvation on the iron(IV)-oxo complex **4**. The infrared spectrum of **4**•H₂O (Figure 60g) shows two free O–H stretching vibrations at 3,626 cm⁻¹ and 3704 cm⁻¹. Moreover, we observe the Fe–O stretch of the iron(IV)-oxo unit at unchanged position from **4**. Therefore, the water molecule does not interact with the iron(IV)-oxo unit, as can be expected due to its weaker basicity compared to the iron(III)-oxo unit. The slight red shifts of both O–H bands with respect to the free water molecule (3657 and 3756 cm⁻¹)²⁴⁶ are typical for water molecule interacting with charged species.²⁴⁷ The absence of hydrogen bonding to iron(IV)-oxo unit is in line with the previous findings on the protonation of iron(IV)-oxo complexes.^{36,248}

4.4. Gas-Phase Reactivity

Finally, I studied the reactivity of the prepared iron(III)-oxo complexes. Specifically, I was interested how the one-electron reduction changes the propensity of the iron-oxo complexes to HAT. In section 3.4, I showed that gaseous iron(IV)-oxo complexes react with 1,4-cyclohexadiene by HAT from the allylic position (BDE(C–H) = 76 kcal mol⁻¹).²⁴⁹ I decided to compare complexes bearing the N4Py ligand: **11** and **5**, because they have the same first coordination sphere as well as the overall charge. Complex **5** reacts with 1,4-cyclohexadiene by HAT to form a cyclohexadienyl radical or by oxygen atom transfer (OAT) resulting in epoxidation of the C=C bond (Figure 62a, red trace). In contrast, studied iron(III)-oxo complexes **11–14_{syn}** do not react with 1,4-cyclohexadiene at all (Figure 62b, red trace, Figure 63a – the observed reaction products are all results of reactions with impurities that could not be cleared from the collision cell).

Reduction of iron(IV)-oxo complexes should, however, result in larger basicity.²⁵² Therefore, I tested the reactivity of **11–14_{syn}** with acetic acid in the gas phase and observed efficient addition reaction (Figure 64). The reaction likely involves a proton transfer resulting in a ion pair between acetate and iron(III)-oxo complex (Equation (13)). Dication-anion separation will never happen in low-energy collisions in the gas phase because of large energy requirements. Alternative path would be electron transfer to form iron(II)-hydroxo complex and acetoxy radical, but oxidation of acetate anion is not easy. However, thiolates are much easier to oxidize.²⁵⁰ Therefore, I investigated the reaction of iron(III)-oxo complexes with ethanethiol. I note in passing that I also investigated reactions of **11** with

H₂O, MeOH, CHCl₃, CO₂ and EtOAc, but did not see any reactivity. We expected that we might observe proton transfer reaction followed by electron transfer (PT-ET²⁵¹⁻²⁵³ reaction; Equation (14)). Formally, the PT-ET reaction appears as a hydrogen atom transfer, but the homolytic cleavage of the S–H bond appears to be energetically inaccessible for the studied complexes, because the BDE(S–H) of 87 kcal mol⁻¹ in ethanethiol is larger than the BDE(C–H) in cyclohexadiene.²⁵⁴ I observed the formal hydrogen atom transfer reactivity with ethanethiol for all studied iron(III)-oxo complexes (Figure 62b, black trace, Figure 63b; differences in reactivity are discussed below). In comparison, iron(IV)-oxo complex **5** shows no HAT or PT-ET reactivity towards ethanethiol, but only OAT (Figure 62a, black trace). These results demonstrate basicity of iron(III)-oxo complexes; despite being positively charged gaseous complexes, they still mediate reactions initiated by their protonation and resemble the proton-coupled electron transfer (PCET) mechanism proposed for the reaction between gaseous Al₂O₂⁺ and methane.⁸⁷

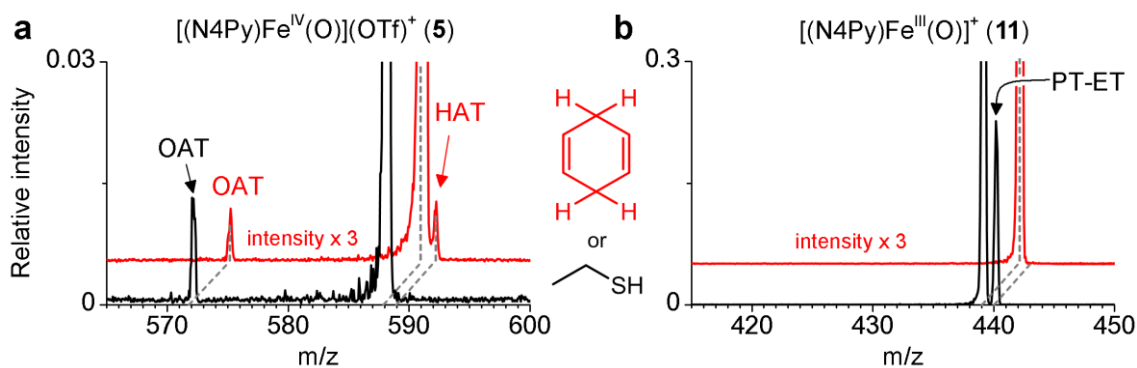


Figure 62. Product mass spectra of gas-phase reactions of (a) iron(IV)-oxo complex **5** and (b) iron(III)-oxo complex **11** with ethanethiol (black traces) and 1,4-cyclohexadiene (red traces) at 0.2 mTorr pressure.

The exact reactivity of iron(III)-oxo complex with ethanethiol depends on the ligand (Figure 63, Table 8): whereas **11** and **14_{syn}** react predominantly by PT-ET mechanism (**11** reacts about 100 times faster than **14_{syn}**), complexes **12** and **13** show a competition of this channel with the formal addition reaction pathway, like observed with acetic acid. The lack of reactivity in complex **14_{syn}**, which also has a free coordination site on the iron, shows the

importance of deprotonation in this addition reaction (in the case of **14_{syn}** the thiolate could not coordinate to the iron, because the free site is at the other end of the molecule). Reactions of **12** and **13** thus follow predominantly the same pathway as the reaction of **13** with water in the cold trap discussed above, where we characterized the iron(III)-dihydroxo product by IRPD spectroscopy (Figure 60e).

Table 8. Relative cross sections^a of reactions of complexes 11–14_{syn} and 5 with ethanethiol at nominally zero collision energy.

| ion\product | M+1 (HAT) [KIE ^b] | M+62 (addition) [KIE ^b] | M+45 EtS) | (-O + M-16 (OAT) |
|---|----------------------------------|---|--------------|---------------------|
| [(N4Py)Fe ^{III} (O)] ⁺ (11) | 100 ± 12 [2.1 ± 0.4] | - | - | - |
| [(TPA)Fe ^{III} (O)] ⁺ (12) | 20 ± 4 | 210 ± 5 | 7 ± 2 | - |
| [(TQA)Fe ^{III} (O)] ⁺ (13) | 17 ± 2 [1.7 ± 0.2] | 110 ± 20 [1.4 ± 0.2] | 17 ± 5 | - |
| [(TMC)Fe ^{III} (O) _{syn}] ⁺ (14_{syn}) | 1 ± 0.1 | - | - | - |
| [(N4Py)Fe ^{IV} (O)](OTf) ⁺ (5) ^c | - | - | - | 5 ± 1 |
| [(N4Py)Fe ^{IV} (O)](OTf) ⁺ (5) ^{c,d} | 1.04 ± 0.16 | - | - | 0.6 ± 0.4 |

^aThe relative cross sections were measured at zero collision energy. Scan time was set 10 s, measurements were carried out at pressures 0.2 mTorr in the octopole collision cell and repeated on two different days. The relative cross section σ_i for i -th reaction channel corresponding to the reaction $P \rightarrow F_1 + F_2 + \dots + F_n$ was determined as $\sigma_i^{\text{rel}} = A \cdot \ln(1 - \sum I_n / (\sum I_n + I_p)) \cdot I_n / \sum I_n$, where I_n is the intensity of the n -th product ion F_n , I_p is the intensity of the parent ion, A is a normalizing factor (the reactivity of **11** with was set to 100).

^bIntermolecular kinetic isotope effects (KIEs) for the reactions with ethanethiol were obtained from competition experiments with EtSH/EtSD mixture. The EtSH/EtSD mixture was obtained by isotope exchange of EtSH with D₂O (approximately 1:1 mass ratio) and separation of the organic layer. The exact EtSH/EtSD ratio in the collision cell was determined from the ligand exchange reaction with [(Me₃P)Au(ACN)]⁺ or [(IPr)Au(MeOH)]⁺ ions (IPr = 1,3-bis(2,6-diisopropylphenyl)imidazol-2-ylidene), where we assumed a kinetic isotope effect of 1.

^cCross sections measured on a single day.

^dReaction with 1,4-cyclohexadiene.

I also determined intermolecular kinetic isotope effects in reactions of **11** and **13** with a mixture of EtSD and EtSH. The KIE of the PT-ET reaction of **11** is 2.1 ± 0.4. Similarly, KIEs of the PT-ET reaction and the proton transfer/recombination reaction of **13** are 1.7 ± 0.2 and 1.4 ± 0.2, respectively. The slightly smaller KIE in the proton transfer/recombination

reaction pathway may be caused by interfering association reaction with a KIE 1. In comparison, the KIEs observed in HAT reactions of iron(IV)-oxo complexes with 1,4-cyclohexadiene are typically above 3 (Table 4). Therefore, the observed KIEs further support the proton transfer and not the hydrogen atom transfer as the rate-limiting step in the studied reactions of iron(III)-oxo complexes with ethanethiol.

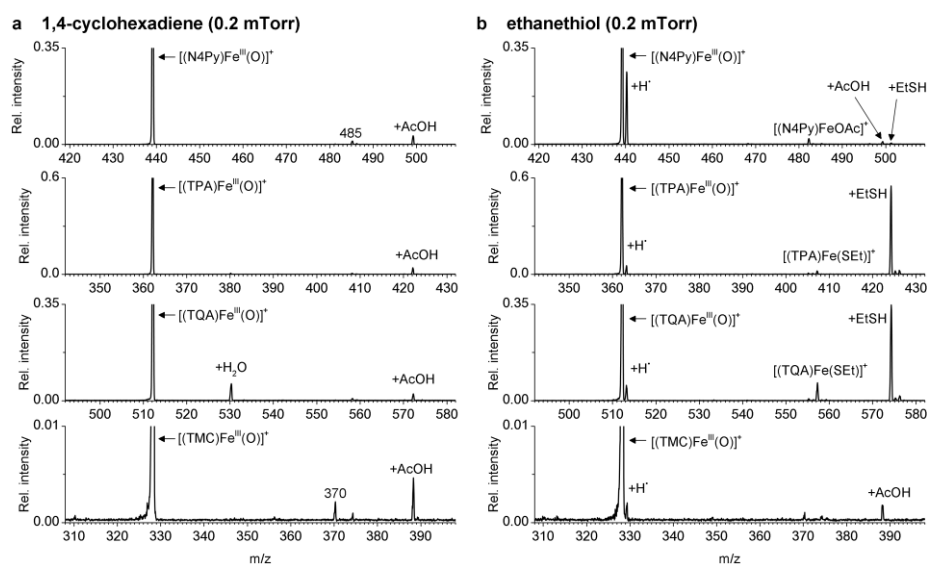


Figure 63. Mass spectra of reaction products of iron(III)-oxo complexes **11–14_{syn}** with (a) 1,4-cyclohexadiene (all reaction product ions come from reactions with impurities in the collision cell) and (b) ethanethiol at nominally zero collision energy. The pressure of the reactant gas in the octopole collision cell was 0.2 mTorr, the scan time was 10 seconds and the manifold temperature was 70°C. Kinetic energy distributions were measured by retarding potential analysis. Typical FWHM of the kinetic energy distributions of reactants was 1 eV_{lab}.

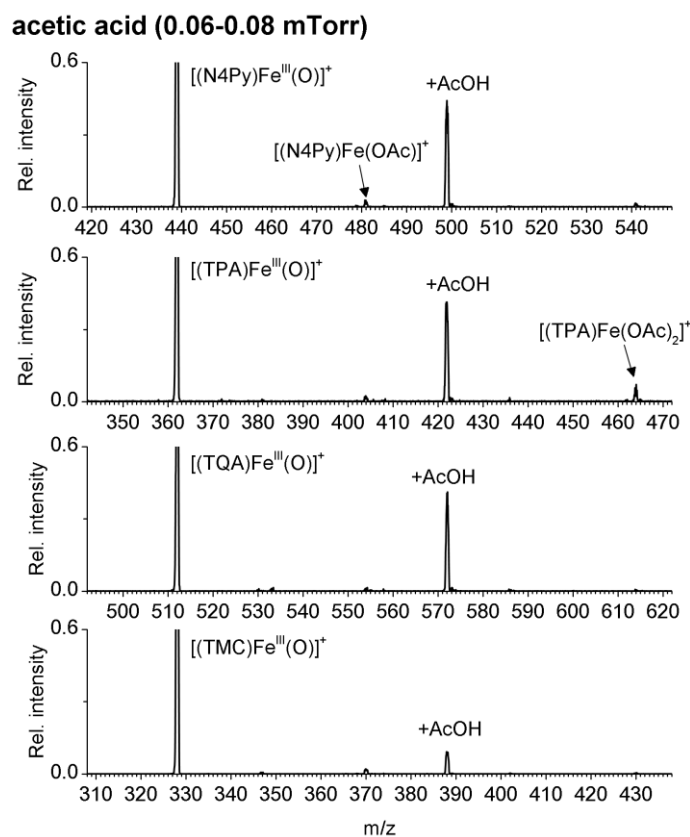


Figure 64. Mass spectra of reaction products of iron(III)-oxo complexes **11–14**_{syn} with gaseous acetic acid. The collision cell potential was set to the potential of the transfer quadrupole, which typically corresponds to nominally zero-collision energy to within 0.2 V. The pressure of the reactant gases was 0.06–0.08 mTorr, the scan time was 10 seconds and the manifold temperature was 70°C.

4.5. Correlation of the Fe–O Stretching Frequencies and Bond Lengths

Finally, I summarized the Fe–O stretching frequencies and the Fe–O bond distances in the reported iron(IV) and iron(III)-oxo complexes. I included data points, where both bond length and Fe–O frequency were known. I also included the recently reported tetragonal d^5 cobalt-oxo complex by Nam group¹²⁹ and d^6 cobalt-oxo by Anderson group.¹³² To this, I also added our values from the gas phase with the B3LYP-calculated bond lengths. Figure 65 shows the trends that I discussed previously - the lack of correlation of the spin state with the Fe=O bond parameters in the iron(IV)-oxo complexes (compare light blue with the dark blue points) and the clustering of the iron(III)-oxo complexes based on their spin state (two groups of red points). The figure also shows, that the B3LYP predictions of the bond lengths are likely to be correct (Fe=O frequencies are usually predicted unreliably, see the DFT spectra predictions shown in section 3.2).

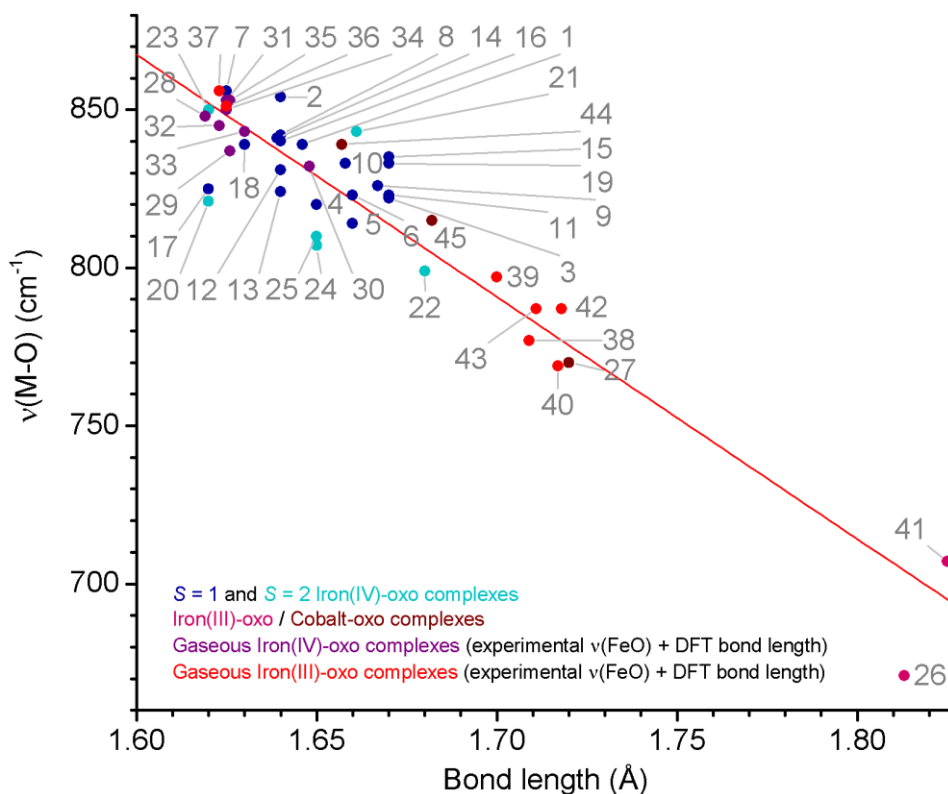


Figure 65. Correlation between M–O bond lengths and vibrational frequencies in iron-oxo and cobalt-oxo complexes. The experimental data and complex names were taken from Refs. 65,240 (iron-oxo complexes) and Refs. 129,132 (cobalt-oxo complexes). The figure includes frequencies of iron-oxo complexes measured in the gas phase plotted against the Fe–O bond lengths calculated at B3LYP functional and triple zeta basis sets. The linear fit is $\tilde{\nu}(\text{M-O}) = 2093 - 766 r(\text{M-O})$ ($R^2 = 0.88$). If only the complexes, where both $\tilde{\nu}(\text{M-O})$ and $r(\text{M-O})$ are known experimentally are included, it is $\tilde{\nu}(\text{M-O}) = 2099 - 770 r(\text{M-O})$ ($R^2 = 0.85$). The individual data points are: $[\text{Fe}^{\text{IV}}(\text{O}_{\text{anti}})(\text{TMC})(\text{MeCN})]^{2+}$ (1), $[\text{Fe}^{\text{IV}}(\text{O}_{\text{anti}})(\text{TMC})(\text{CF}_3\text{COO})]^+$ (2), $[\text{Fe}^{\text{IV}}(\text{O}_{\text{anti}})(\text{TMC})(\text{NCO})]^+$ (3), $[\text{Fe}^{\text{IV}}(\text{O}_{\text{anti}})(\text{TMC})(\text{NCS})]^+$ (4), $[\text{Fe}^{\text{IV}}(\text{O}_{\text{anti}})(\text{TMC})(\text{N}_3)]^+$ (5), $[\text{Fe}^{\text{IV}}(\text{O}_{\text{anti}})(\text{TMC})(\text{CN})]^+$ (6), $[\text{Fe}^{\text{IV}}(\text{O}_{\text{syn}})(\text{TMC})(\text{MeCN})]^{2+}$ (7), $[\text{Fe}^{\text{IV}}(\text{O})(\text{TBC})(\text{MeCN})]^{2+}$ (8), $[\text{Fe}^{\text{IV}}(\text{O})(\text{TMCPy})(\text{MeCN})]^{2+}$ (9), $[\text{Fe}^{\text{IV}}(\text{O})(\text{TMCdma})]^{2+}$ (10), $[\text{Fe}^{\text{IV}}(\text{O})(\text{TMCdma} - \text{H})]^+$ (11), $[\text{Fe}^{\text{IV}}(\text{O})(\text{TMCSO}_2)]^+$ (12), $[\text{Fe}^{\text{IV}}(\text{O})(\text{Me}_2\text{EBC})(\text{MeCN})]^{2+}$ (13), $[\text{Fe}^{\text{IV}}(\text{O})(\text{N4Py})]^{2+}$ (14), $[\text{Fe}^{\text{IV}}(\text{O})(\text{Bn-TPEN})]^{2+}$ (15), $[\text{Fe}^{\text{IV}}(\text{O})(\text{BisPi1})]^{2+}$ (16), $[\text{Fe}^{\text{IV}}(\text{O})(\text{BisPi2})]^{2+}$ (17), $[\text{Fe}^{\text{IV}}(\text{O})(\text{Me}_2\text{TACN-Py}_2)]^{2+}$ (18), $[\text{Fe}^{\text{IV}}(\text{O})(\text{TPA})(\text{MeCN})]^{2+}$ (19), TauD-J (20), $[\text{Fe}^{\text{IV}}(\text{O})(\text{TMG}_3\text{tren})]^{2+}$ (21), $[\text{Fe}^{\text{IV}}(\text{O})(\text{H}_3\text{buea})]^-$ (22), $[\text{Fe}^{\text{IV}}(\text{O})(\text{tpa}^{\text{Ph}})]^-$ (23), $[\text{Fe}^{\text{IV}}(\text{O})(\text{TMG}_2\text{dien})(\text{MeCN})]^{2+}$ (24), $[\text{Fe}^{\text{IV}}(\text{O})(\text{TMG}_2\text{dien})(\text{Cl})]^+$ (25), $[\text{Fe}^{\text{III}}(\text{O})(\text{H}_3\text{Buea})]^{2-}$ (26), $[\text{Co}^{\text{IV}}(\text{O})(13\text{-TMC})]^{2+}$ (27), $[\text{Fe}^{\text{IV}}(\text{O}_{\text{anti}})(\text{TMC})(\text{MeCN})]^{2+}$ (28), $[\text{Fe}^{\text{IV}}(\text{O}_{\text{anti}})(\text{TMC})(\text{OTf})]^+$ (29), $[\text{Fe}^{\text{IV}}(\text{O}_{\text{anti}})(\text{TMC})(\text{N}_3)]^+$ (30), $[\text{Fe}^{\text{IV}}(\text{O})(\text{N4Py})]^{2+}$ (31), $[\text{Fe}^{\text{IV}}(\text{O})(\text{N4Py})](\text{OTf})^+$ (32), $[\text{Fe}^{\text{IV}}(\text{O}_{\text{eq}})(\text{PyTACN})(\text{MeCN})]^{2+}$ (33), $[\text{Fe}^{\text{IV}}(\text{O}_{\text{eq}})(\text{PyTACN})(\text{NO}_3)]^{2+}$ (34), $[\text{Fe}^{\text{IV}}(\text{O}_{\text{eq}})(\text{PyTACN})(\text{CF}_3\text{COO})]^{2+}$ (35), $[\text{Fe}^{\text{III}}(\text{O})(\text{N4Py})]^+$ (36), $[\text{Fe}^{\text{III}}(\text{O})(\text{TPA})]^+$ (37), $[\text{Fe}^{\text{III}}(\text{O})(\text{TQA})]^+$ (38), $[\text{Fe}^{\text{III}}(\text{O}_{\text{syn}})(\text{TMC})]^+$ (39), $[\text{Fe}^{\text{III}}(\text{O}_{\text{anti}})(\text{TMC})]^+$ (40), $[(\text{N4Py})\text{Fe}^{\text{III}}-\text{O}-\text{Ce}^{\text{IV}}(\text{NO}_3)_4(\text{H}_2\text{O})]^+$ (41), $[\text{Fe}^{\text{III}}(\text{N4Py})(\text{O})(\text{H}_2\text{O})]^+$ (42), $[\text{Fe}^{\text{III}}(\text{TPA})(\text{O})(\text{H}_2\text{O})]^+$ (43), $[\text{Co}^{\text{III}}(\text{O})(\text{tBuIm})]$ (45).

4.6. Conclusions

In this Chapter, I used helium tagging IR and vis spectroscopy to characterize iron(III)-oxo complexes that are not stabilized by extensive hydrogen bonding. I observed both quartet and sextet state complexes, depending on the used ligand and characterized them by IR and vis spectroscopy. I used ^{18}O labeling to determine the Fe=O stretching vibration frequencies. Visible spectra, along with the inspection of the ligand vibrational spectra gave me more confidence in spin state assignment. Results show that the Fe–O stretching frequencies are mainly determined by the spin state. The Fe–O stretching frequencies of quartet complexes are essentially identical to those of iron(IV)-oxo complexes (800–850 cm^{-1}). This means that the additional electron is introduced to an orbitals without Fe–O antibonding character. On contrary, sextet complexes have their Fe–O stretching frequencies around 70 cm^{-1} lower, reflecting a decrease in the Fe–O bond order.

I also showed, that the spin state of the quartet state iron(III)-oxo complexes can be switched to sextet by coordination of single water molecule. The change is evidenced by IR and vis spectroscopy. The change is triggered by the formation of a hydrogen bond between the oxo and the water molecule and results in the red shift of the Fe–O stretching frequency by about 70 cm^{-1} . In contrast, no such shift was observed when we performed similar experiment in iron(IV)-oxo complex $[(\text{N4Py})\text{Fe}^{\text{IV}}(\text{O})]^{2+} \cdot \text{H}_2\text{O}$. This is consistent with the larger basicity of the iron(III)-oxo unit compared to the iron(IV).

This larger basicity has also important ramifications for the reactivity. The basic oxo group can detach acidic protons from thiols and trigger proton-transfer-electron transfer reactivity. Proton transfer reaction, observed as the adduct formation, was observed with carboxylic acid, whose anion is difficult to oxidize.

Finally, the presented iron(III)-oxo complexes constitute examples of d^5 oxo species that lie just at the boundary of the oxo wall.

CHAPTER 5. Summary

Biomimetic chemistry of iron intermediates has seen a huge surge in popularity since the turn of the millennium. Despite the routine use of mass spectrometry in HRMS characterization of the studied species, which are often difficult to characterize, there were only a few attempts to extend the mass-spectrometric characterization with ion spectroscopy.

I have developed methods of ion generation that allowed us to use cryogenic ion spectroscopy to obtain IR and vis spectra of iron-oxo species. Specifically, I investigated the use of nitrate cleavage to generate iron($n+1$)-oxo species from iron(n) nitrate precursors in the gas phase. I also found a way to reduce dicationic iron(IV)-oxo species to iron(III)-oxo species with tetrakis(dimethylamino)ethylene in the gas phase. I improved the overall experimental technique to make ion spectroscopic measurements of iron-oxo complexes simpler.

In chapter 3, I describe the collection of benchmark iron(IV)-oxo IRPD vibrational data, which allowed us to see the correlations between the gas phase and the condensed phase; we found, that solvation has relatively modest impact of $\sim 10\text{ cm}^{-1}$ red shift in the Fe=O stretching frequency. We also found a method to assign spin states of the complexes based on their IR spectra. We observed stereoisomers of $[(\text{PyTACN})\text{Fe}^{\text{IV}}(\text{O})(\text{NO}_3)]^+$ complexes, that differed in their spin state. This observation allowed us to conclude that the effect of the spin state on the Fe–O stretching vibration is negligible. I also compared gas-phase reactivity modes of various iron(IV)-oxo complexes and hydride transfer reactivity in dications, and HAT + OAT reactivity in monocations. The attenuation of reactivity with a coordinated counterion depended on its mode of coordination, with the biggest influence seen in *trans* position to oxo unit.

In chapter 4, I used gas phase techniques to prepare and characterize iron(III)-oxo species with different amine ligands. We observed iron(III)-oxo complexes in the quartet and sextet spin states assigned by combination of IRPD and visPD spectroscopies. We also studied the effect of hydrogen bonding, and found, that the spin state of quartet iron(III)-oxo complexes can be changed to sextet. Finally, I measured reactivity of iron(III)-oxo complexes in the gas phase with various substrates and I found that they act as both bases and oxidants. I discovered the efficient HAT reaction with ethanethiol that likely has a PT-ET mechanism.

To sum up, my work has helped to establish IRPD/visPD spectroscopy as a method for vibrational and electronic characterization of biomimetic iron complexes.

References

- (1) Holland, H. D. The oxygenation of the atmosphere and oceans. *Phil. Trans. R. Soc. B* **2006**, *361*, 903–915.
- (2) Lyons, T. W.; Reinhard, C. T.; Planavsky, N. J. The rise of oxygen in Earth's early ocean and atmosphere. *Nature* **2014**, *506*, 307–315.
- (3) Borden, W. T.; Hoffmann, R.; Stuyver, T.; Chen, B. Dioxygen: What Makes This Triplet Diradical Kinetically Persistent? *J. Am. Chem. Soc.* **2017**, *139*, 9010–9018.
- (4) *Iron Containing Enzymes: Versatile Catalysts of Hydroxylation Reactions in Nature*; de Visser, S. P., Kumar, D., Eds.; RSC Publishing: Cambridge, U.K., 2011.
- (5) Hernandez-Ortega, A.; Quesne, M. G.; Bui, S.; Heyes, D. J.; Steiner, R. A.; Scrutton, N. S.; de Visser, S. P. Catalytic Mechanism of Cofactor-Free Dioxygenases and How They Circumvent SpinForbidden Oxygenation of Their Substrates. *J. Am. Chem. Soc.* **2015**, *137*, 7474–7487.
- (6) Schröder, D.; Shaik, S.; Schwarz, H.; Two-State Reactivity as a New Concept in Organometallic Chemistry. *Acc. Chem. Res.* **2000**, *33*, 139–145.
- (7) Behr, M. J.; Harrenga, A.; Kannt, A. CYTOCHROME C OXIDASE: Structure and Spectroscopy. *Annu. Rev. Biophys. Biomol. Struct.* **1998**, *27*, 329–356.
- (8) Yoshikawa, S.; Shimada, A. Reaction Mechanism of Cytochrome *c* Oxidase. *Chem. Rev.* **2015**, *115*, 1936–1989.
- (9) Guengerich, F. P. Common and Uncommon Cytochrome P450 Reactions Related to Metabolism and Chemical Toxicity. *Chem. Res. Toxicol.* **2001**, *14*, 611–650.
- (10) Guengerich, F. P. Mechanisms of Cytochrome P450-Catalyzed Oxidations *ACS Catal.* **2018**, *8*, 10964–10976.
- (11) Meunier, B.; de Visser, S. P.; Shaik, S. Mechanism of Oxidation Reactions Catalyzed by Cytochrome P450 Enzymes. *Chem. Rev.* **2004**, *104*, 3947–3980.
- (12) Danielson P. B. The cytochrome P450 superfamily: biochemistry, evolution and drug metabolism in humans. *Curr. Drug Metab.* **2002**, *3*, 561–97.
- (13) Rendic, S.; Guengerich, F. P. Survey of Human Oxidoreductases and Cytochrome P450 Enzymes Involved in the Metabolism of Xenobiotic and Natural Chemicals. *Chem. Res. Toxicol.* **2015**, *28*, 38–42.
- (14) Rittle, J.; Green, M. T. Cytochrome P450 compound I: capture, characterization, and C-H bond activation kinetics. *Science* **2010**, *330*, 933–937.
- (15) Groves, J. T.; McClusky, G. A. Aliphatic Hydroxylation via Oxygen Rebound. Oxygen Transfer Catalyzed by Iron. *J. Am. Chem. Soc.* **1976**, *98*, 859–861.
- (16) Huang, X.; Groves, J. T. Oxygen Activation and Radical Transformations in Heme Proteins and Metalloporphyrins. *Chem. Rev.* **2018**, *118*, 2491–2553.
- (17) Solomon, E. I.; Brunold, T. C.; Davis, M. I.; Kemsley, J. N.; Lee, S.-K.; Lehner, N.; Neese, F.; Skulan, A. J.; Yang, Y.-S.; Zhou, J. Geometric and Electronic Structure/Function Correlations in Non-Heme Iron Enzymes. *Chem. Rev.* **2000**, *100*, 235–349.
- (18) Solomon, E. I.; Light, K. M.; Liu, L. V.; Srncic, M.; Wong, S. D. Geometric and Electronic Structure Contributions to Function in Non-heme Iron Enzymes. *Acc. Chem. Res.* **2013**, *46*, 2725–2739.
- (19) Abu-Omar, M. M.; Loaiza, A.; Hontzeas, N. Reaction Mechanisms of Mononuclear Non-Heme Iron Oxygenases. *Chem. Rev.* **2005**, *105*, 2227–2252.
- (20) Price, J. C.; Barr, E. W.; Tirupati, B.; Bollinger, J. M., Jr.; Krebs, C. The First Direct Characterization of a High-Valent Iron Intermediate in the Reaction of an α -Ketoglutarate-Dependent Dioxygenase: A High-Spin Fe(IV) Complex in Taurine/ α -Ketoglutarate Dioxygenase (TauD) from *Escherichia coli*. *Biochemistry* **2003**, *42*, 7497–7508.

- (21) Bollinger, J. M., Jr.; Krebs, C. Stalking intermediates in oxygen activation by iron enzymes: motivation and method. *J. Inorg. Biochem.* **2006**, *100*, 586–605.
- (22) Krebs, C.; Galonić Fujimori, D.; Walsh, C. T.; Bollinger, J. M., Jr. Non-Heme Fe(IV)–Oxo Intermediates. *Acc. Chem. Res.* **2007**, *40*, 484–492.
- (23) Gorres K. L.; Raines R. T. Prolyl 4-hydroxylase. *Crit. Rev. Biochem. Mol. Biol.* **2010**, *45*, 106–124.
- (24) Trewick, S. C.; Henshaw, T. F.; Hausinger, R. P.; Lindahl, T.; Sedgwick, B. Oxidative demethylation by *Escherichia coli* AlkB directly reverts DNA base damage. *Nature* **2002**, *419*, 174–178.
- (25) Fitzpatrick, P. F. Tetrahydropterin-dependent amino acid hydroxylases. *Annu. Rev. Biochem.* **1999**, *68*, 355–381.
- (26) Ensley B. D.; Gibson D.T. Naphthalene Dioxygenase: Purification and Properties of a Terminal Oxygenase Component. *J. Bacteriol.* **1983**, *155*, 505–511.
- (27) Wolfe, M. D.; Lipscomb, J. D. Hydrogen peroxide-coupled cis-diol formation catalyzed by naphthalene 1,2-dioxygenase. *J. Biol. Chem.* **2003**, *278*, 829–835.
- (28) Regulus, P.; Duroux, B.; Bayle, P.-A.; Favier, A.; Cadet, J.; Ravanat, J.-L. Oxidation of the sugar moiety of DNA by ionizing radiation or bleomycin could induce the formation of a cluster DNA lesion. *Proc. Natl. Acad. Sci. U. S. A.* **2007**, *104*, 14032–14037.
- (29) Regulus, P.; Duroux, B.; Bayle, P.-A.; Favier, A.; Cadet, J.; Ravanat, J.-L. Oxidation of the sugar moiety of DNA by ionizing radiation or bleomycin could induce the formation of a cluster DNA lesion. *Proc. Natl. Acad. Sci. U. S. A.* **2007**, *104*, 14032–14037.
- (30) Proshlyakov, D. A.; Henshaw, T. F.; Monterosso, G. R.; Ryle, M. J.; Hausinger, R. P. Direct Detection of Oxygen Intermediates in the Non-Heme Fe Enzyme Taurine/R-Ketoglutarate Dioxygenase. *J. Am. Chem. Soc.* **2004**, *126*, 1022–1023.
- (31) Riggs-Gelasco, P. J.; Price, J. C.; Guyer, R. B.; Brehm, J. H.; Barr, E. W.; Bollinger, J. M., Jr.; Krebs, C. EXAFS Spectroscopic Evidence for an FeO Unit in the Fe(IV) Intermediate Observed during Oxygen Activation by Taurine:R-Ketoglutarate Dioxygenase. *J. Am. Chem. Soc.* **2004**, *126*, 8108–8109.
- (32) Scheidt, W. R.; Durbin, S. M.; Sage, J. T. Nuclear resonance vibrational spectroscopy – NRVs. *J. Inorg. Biochem.* **2005**, *99*, 60–71.
- (33) Scheidt, W. R.; Li, J.; Sage, T. J. What Can Be Learned from Nuclear Resonance Vibrational Spectroscopy: Vibrational Dynamics and Hemes. *Chem. Rev.* **2017**, *117*, 12532–12563.
- (34) Wong, S. D.; Srncic, M.; Matthews, M. L.; Liu, L. V.; Kwak, Y.; Park, K.; Bell, C. B., III; Alp, E. E.; Zhao, J.; Yoda, Y.; Kitao, S.; Seto, M.; Krebs, C.; Bollinger, J. M., Jr.; Solomon, E. I. Elucidation of the Fe(IV)=O intermediate in the catalytic cycle of the halogenase SyrB2. *Nature* **2013**, *499*, 320–323.
- (35) Kwon, H.; Basran, J.; Casadei, C. M.; Fielding, A. J.; Schrader, T.; Ostermann, A.; Devos, J.; M.; Aller, P.; Blakeley, M. P.; Moody, P. C. E.; Raven, E. L. Direct visualization of a Fe(IV)–OH intermediate in a heme enzyme. *Nat. Commun.* **2016**, *7*, 13445.
- (36) Casadei C. M.; Gumiero A.; Metcalfe C. L.; Murphy E. J.; Basran J.; Concilio M. G.; Teixeira S. C.; Schrader T. E.; Fielding A. J.; Ostermann A.; Blakeley M. P.; Raven E. L.; Moody P. C. Heme enzymes. Neutron cryo-crystallography captures the protonation state of ferryl heme in a peroxidase. *Science* **2014**, *345*, 193–197.
- (37) Meharena, Y. T.; Doukov, T.; Li, H.; Soltis, M.; Poulos, T. L. Crystallographic and Single Crystal Spectral Analysis of the Peroxidase Ferryl Intermediate. *Biochemistry* **2010**, *49*, 2984–2986.
- (38) Karlin, K. D. Model offers intermediate insight. *Nature* **2010**, *463*, 168–169.
- (39) Costas, M.; Mehn, M. P.; Jensen, M. P.; Que, L., Jr. Oxygen Activation at Mononuclear Nonheme Iron: Enzymes, Intermediates, and Models. *Chem. Rev.* **2004**, *104*, 939–986.
- (40) Company, A.; Lloret-Fillol, J.; Costas, M. Small Molecule Models for Nonporphyrinic Iron and Manganese Oxygenases. In *Comprehensive Inorganic Chemistry II*; Reedijk, J., Poepelmeier, K., Eds.; Elsevier: Oxford, 2013; Vol. 3, pp 487–564.

- (41) MacBeth, C. E.; Golombek, A. P.; Young, V. G.; Yang, C.; Kuczera, K.; Hendrich, M. P.; Borovik, A. S. O₂ Activation by Nonheme Iron Complexes: A Monomeric Fe(III)-Oxo Complex Derived From O₂. *Science* **2000**, *289*, 938–941.
- (42) Cook, S. A.; Borovik, A. S. Molecular Designs for Controlling the Local Environments around Metal Ions. *Acc. Chem. Res.* **2015**, *48*, 2407–2414.
- (43) Matson, E. M.; Park, Y. J.; Fout, A. R. Facile Nitrite Reduction in a Non-heme Iron System: Formation of an Iron(III)-Oxo. *J. Am. Chem. Soc.* **2014**, *136*, 17398–17401.
- (44) Grapperhaus, C. A.; Mienert, B.; Bill, E.; Weyhermüller, T.; Wieghardt, K. Mononuclear (Nitrido)iron(V) and (Oxo)iron(IV) Complexes via Photolysis of [(cyclam-acetato)Fe^{III}(N₃)]⁺ and Ozonolysis of [(cyclam-acetato)Fe^{III}(O₃SCF₃)]⁺ in Water/Acetone Mixtures. *Inorg. Chem.* **2000**, *39*, 5306–5317.
- (45) Rohde, J.-U.; In, J.-H.; Lim, M. H.; Brennessel, W. W.; Bukowski, M. R.; Stubna, A.; Münck, E.; Nam, W.; Que L., Jr. Crystallographic and Spectroscopic Characterization of a Nonheme Fe(IV)=O Complex. *Science* **2003**, *299*, 1037–1039.
- (46) Lubben, M.; Meetsma, A.; Wilkinson, E. C.; Feringa, B.; Que, L., Jr. Nonheme Iron Centers in Oxygen Activation: Characterization of an Iron(III) Hydroperoxide Intermediate. *Angew. Chem. Int. Ed. Engl.* **1995**, *34*, 1512–1514.
- (47) Kaizer, J.; Klinker, E. J.; Oh, N. Y.; Rohde, J.-U.; Song, W. J.; Stubna, A.; Kim, J.; Münck, E.; Nam, W. Nonheme Fe^{IV}O Complexes That Can Oxidize the C–H Bonds of Cyclohexane at Room Temperature. *J. Am. Chem. Soc.* **2004**, *126*, 472–473.
- (48) Klinker, E. J.; Kaizer, J.; Brennessel, W. W.; Woodrum, N. L.; Cramer, C. J.; Que, L., Jr. Structures of Nonheme Oxoiron(IV) Complexes from X-ray Crystallography, NMR Spectroscopy, and DFT Calculations. *Angew. Chem. Int. Ed.* **2005**, *44*, 3690.
- (49) Pestovsky, O.; Stoian, S.; Bominaar, E. L.; Shan, X.; Münck, E.; Que, L., Jr.; Bakac, A. Aqueous Fe^{IV}=O: Spectroscopic Identification and Oxo-Group Exchange. *Angew. Chem. Int. Ed.* **2005**, *44*, 6871–6874.
- (50) Ye, S.; Geng, C.-Y.; Shaik, S.; Neese, F. Electronic structure analysis of multistate reactivity in transition metal catalyzed reactions: the case of C–H bond activation by non-heme iron(IV)–oxo cores. *Phys. Chem. Chem. Phys.* **2013**, *15*, 8017–8030.
- (51) Bryliakov, K. P.; Talsi, E. P. Active sites and mechanisms of bioinspired oxidation with H₂O₂, catalyzed by non-heme Fe and related Mn complexes. *Coord. Chem. Rev.* **2014**, *276*, 73–96.
- (52) Shaik, S.; Chen, H.; Janardanan, D. Exchange-enhanced reactivity in bond activation by metal-oxo enzymes and synthetic reagents. *Nat. Chem.* **2011**, *3*, 19–27.
- (53) Janardanan, D.; Wang, Y.; Schyman, P.; Que, L., Jr.; Shaik, S. Fundamental Role of Exchange-Enhanced Reactivity in C–H Activation by S=2 Oxoiron(IV) Complexes. *Angew. Chem. Int. Ed.* **2010**, *49*, 3342–3345.
- (54) England, J.; Martinho, M.; Farquhar, E. R.; Frisch, J. R.; Bominaar, E. L.; Münck, E.; Que, L., Jr. A Synthetic High-Spin Oxoiron(IV) Complex: Generation, Spectroscopic Characterization, and Reactivity. *Angew. Chem. Int. Ed.* **2009**, *48*, 3622–3626.
- (55) Lim, M. H.; Rohde, J. U.; Stubna, A.; Bukowski, M. R.; Costas, M.; Ho, R. Y. N.; Münck, E.; Nam, W.; Que, L., Jr. An Fe^{IV}=O complex of a tetradentate tripodal nonheme ligand. *Proc. Natl. Acad. Sci. U. S. A.* **2003**, *100*, 3665–3670.
- (56) Biswas, A. N.; Puri, M.; Meier, K. K.; Oloo, W. N.; Rohde, G. T.; Bominaar, E. L.; Münck, E.; Que, L., Jr. Modeling TauD-J: A High-Spin Nonheme Oxoiron(IV) Complex with High Reactivity toward C–H Bonds. *J. Am. Chem. Soc.* **2015**, *137*, 2428–2431.

- (57) Seo, M. S.; Kim, N. H.; Cho, K.-B.; So, J. E.; Park, S. K.; Clemancey, M.; Garcia-Serres, R.; Latour, J.-M.; Shaik, S.; Nam, W. A mononuclear nonheme iron(IV)-oxo complex which is more reactive than cytochrome P450 model compound I. *Chem. Sci.* **2011**, *2*, 1039–1045.
- (58) Srncic, M.; Wong, S. D.; England, J.; Que, L., Jr.; Solomon, E. I. π -Frontier molecular orbitals in $S = 2$ ferryl species and elucidation of their contributions to reactivity. *Proc. Natl. Acad. Sci. U. S. A.* **2012**, *109*, 14326–14331.
- (59) Ye, S.; Kupper, C.; Meyer, S.; Andris, E.; Navrátil, R.; Krahe, O.; Mondal, B.; Atanasov, M.; Bill, E.; Roithová, J.; Meyer, F.; Neese, F. Magnetic Circular Dichroism Evidence for an Unusual Electronic Structure of a Tetracarbene–Oxoiron(IV) Complex. *J. Am. Chem. Soc.* **2016**, *138*, 14312–14325.
- (60) Sastri, C. V.; Park, M. J.; Ohta, T.; Jackson, T. A.; Stubna, A.; Seo, M. S.; Lee, J.; Kim, J.; Kitagawa, T.; Munck, E.; Que, L., Jr.; Nam, W. Axial Ligand Substituted Nonheme Fe^{IV}=O Complexes: Observation of Near-UV LMCT Bands and Fe=O Raman Vibrations. *J. Am. Chem. Soc.* **2005**, *127*, 12494–12495.
- (61) Rohde, J.-U.; Stubna, A.; Bominaar, E. L.; Munck, E.; Nam, W.; Que, L., Jr. Nonheme Oxoiron(IV) Complexes of Tris(2-pyridylmethyl)amine with cis-Monoanionic Ligands. *Inorg. Chem.* **2006**, *45*, 6435–6445.
- (62) Planas, O.; Clemancey, M.; Latour, J.-M.; Company, A.; Costas, M. Structural modeling of iron halogenases: synthesis and reactivity of halide-iron(IV)-oxo compounds. *Chem. Commun.* **2014**, *50*, 10887–10890.
- (63) Ye, S.; Kupper, C.; Meyer, S.; Andris, E.; Navrátil, R.; Krahe, O.; Mondal, B.; Atanasov, M.; Bill, E.; Roithová, J.; Meyer, F.; Neese, F. Magnetic Circular Dichroism Evidence for an Unusual Electronic Structure of a Tetracarbene–Oxoiron(IV) Complex. *J. Am. Chem. Soc.* **2016**, *138*, 14312–14325.
- (64) Bell, C. B., III; Wong, S. D.; Xiao, Y.; Klinker, E.; Tenderholt, A. L.; Smith, M. C.; Rohde, J.-U.; Que, L., Jr.; Cramer, S. P.; Solomon, E. I. A Combined NRVs and DFT Study of Fe^{IV}=O Model Complexes: A Diagnostic Method for the Elucidation of Non-Heme Iron Enzyme Intermediates. *Angew. Chem. Int. Ed.* **2008**, *47*, 9071–9074.
- (65) Klein, J. E. M. N.; Que, L., Jr. Biomimetic High-Valent Mononuclear Nonheme Iron-Oxo Chemistry. In *Encyclopedia of Inorganic and Bioinorganic Chemistry*; Scott, R. A., Ed.; John Wiley: Chichester, U.K., 2016, DOI: 10.1002/9781119951438.eibc2344.
- (66) Hohenberger, J.; Ray, K.; Meyer, K. The biology and chemistry of high-valent iron–oxo and iron–nitrido complexes. *Nat. Commun.* **2012**, *3*, 720.
- (67) McDonald, A. R.; Que, L., Jr. High-valent nonheme iron-oxo complexes: Synthesis, structure, and spectroscopy. *Coord. Chem. Rev.* **2013**, *257*, 414–428.
- (68) Ray, K.; Pfaff, F. F.; Wang, B.; Nam, W. Status of Reactive Non-Heme Metal–Oxygen Intermediates in Chemical and Enzymatic Reactions. *J. Am. Chem. Soc.* **2014**, *136*, 13942–13958.
- (69) Nam, W. High-Valent Iron(IV)–Oxo Complexes. *Acc. Chem. Res.* **2007**, *40*, 522–531.
- (70) Nam, W. Synthetic Mononuclear Nonheme Iron–Oxygen Intermediates. *Acc. Chem. Res.* **2015**, *48*, 2415–2423.
- (71) Nam, W.; Lee, Y.-M.; Fukuzumi, S. Tuning Reactivity and Mechanism in Oxidation Reactions by Mononuclear Nonheme Iron(IV)-Oxo Complexes. *Acc. Chem. Res.* **2014**, *47*, 1146–1154.
- (72) Puri, M.; Que, L. Toward the Synthesis of More Reactive $S = 2$ Non-Heme Oxoiron(IV) Complexes. *Acc. Chem. Res.* **2015**, *48*, 2443–2452.
- (73) Engelmann, X.; Monte-Perez, I.; Ray, K. Oxidation Reactions with Bioinspired Mononuclear Non-Heme Metal–Oxo Complexes. *Angew. Chem. Int. Ed.* **2016**, *55*, 7632–7649.
- (74) Que, L.; Tolman, W. B. Biologically inspired oxidation catalysis. *Nature* **2008**, *455*, 333–340.
- (75) Chen, M. S.; White, M. C. A Predictably Selective Aliphatic C–H Oxidation Reaction for Complex Molecule Synthesis. *Science* **2007**, *318*, 783–787.

- (76) Osberger, T. J.; Rogness, D. C.; Kohrt, J. T.; Stepan, A.; White, M. C. Oxidative diversification of amino acids and peptides by small-molecule iron catalysis. *Nature* **2016**, *537*, 214–219.
- (77) Nanjo, T.; de Lucca, E. C.; White, M. C. Remote, Late-Stage Oxidation of Aliphatic C–H Bonds in Amide-Containing Molecules. *J. Am. Chem. Soc.* **2017**, *139*, 14586–14591.
- (78) Mas-Ballesté, R.; Que, L. Iron-Catalyzed Olefin Epoxidation in the Presence of Acetic Acid: Insights into the Nature of the Metal-Based Oxidant. *J. Am. Chem. Soc.* **2007**, *129*, 15964–15972.
- (79) Cussó, O.; Garcia-Bosch, I.; Ribas, X.; Lloret-Fillol, J.; Costas, M. Asymmetric Epoxidation with H₂O₂ by Manipulating the Electronic Properties of Non-heme Iron Catalysts. *J. Am. Chem. Soc.* **2013**, *135*, 14871–14878.
- (80) Theron, R.; Yang, W.; Yunker, L. P. E.; Hesketh, A. V.; Pernik, I.; Weller, A. S.; McIndoe, J. S. Simultaneous Orthogonal Methods for the Real-Time Analysis of Catalytic Reactions. *ACS Catal.* **2016**, *6*, 6911–6917.
- (81) McLuckey, S. A.; Wells, J. M. Mass Analysis at the Advent of the 21st Century. *Chem. Rev.* **2001**, *101*, 571–606.
- (82) To, W. P.; Chow, T. W.-S.; The, C.-W.; Guan, X.; Huang, J.-S.; Che, C.-M. Water oxidation catalysed by iron complex of *N,N'*-dimethyl-2,11-diaza[3,3](2,6)pyridinophane. Spectroscopy of iron–oxo intermediates and density functional theory calculations. *Chem. Sci.* **2015**, *6*, 5891–5903.
- (83) Hitomi, Y.; Arakawa, K.; Funabiki, T.; Kodera, M. An Iron(III)–Monoamidate Complex Catalyst for Selective Hydroxylation of Alkane C–H Bonds with Hydrogen Peroxide. *Angew. Chem. Int. Ed.* **2012**, *51*, 3448–3452.
- (84) Hong, S.; Pfaff, F. F.; Kwon, E.; Wang, Y.; Seo, M.-S.; Bill, E.; Ray, K.; Nam, W. Spectroscopic Capture and Reactivity of a Low-Spin Cobalt(IV)-Oxo Complex Stabilized by Binding Redox-Inactive Metal Ions. *Angew. Chem. Int. Ed.* **2014**, *53*, 10403–10407.
- (85) Prat, I.; Mathieson, J. S.; Güell, M.; Ribas, X.; Luis, J. M.; Cronin, L.; Costas, M. Observation of Fe(V)=O using variable-temperature mass spectrometry and its enzyme-like C–H and C=C oxidation reactions. *Nat. Chem.* **2011**, *3*, 788–793.
- (86) Roithová, J.; Schröder, D. Selective Activation of Alkanes by Gas-Phase Metal Ions. *Chem. Rev.* **2010**, *110*, 1170–1211.
- (87) Li, J.; Zhou, S.; Zhang, J.; Schlangen, M.; Weiske, T.; Usharani, D.; Shaik, S.; Schwarz, H. Electronic Origins of the Variable Efficiency of Room-Temperature Methane Activation by Homo- and Heteronuclear Cluster Oxide Cations [XYO₂]⁺ (X, Y = Al, Si, Mg): Competition between Proton-Coupled Electron Transfer and Hydrogen-Atom Transfer. *J. Am. Chem. Soc.* **2016**, *138*, 7973–7981.
- (88) Schwarz, H.; Shaik, S.; Li, J. Electronic Effects on Room-Temperature, Gas-Phase C–H Bond Activations by Cluster Oxides and Metal Carbides: The Methane Challenge. *J. Am. Chem. Soc.* **2017**, *139*, 17201–17212.
- (89) Schwarz, H. Chemistry with Methane: Concepts Rather than Recipes. *Angew. Chem. Int. Ed.* **2011**, *50*, 10096–10115.
- (90) Schröder, D.; Schwarz, H. FeO[⊕] Activates Methane. *D. Angew. Chem. Int. Ed. Engl.* **1990**, *29*, 1433–1434.
- (91) Shaik, S.; Danovich, D.; Fielder, A.; Schröder, D.; Schwarz, H. Two-State Reactivity in Organometallic Gas-Phase Ion Chemistry. *Helv. Chim. Acta* **1995**, *78*, 1393–1407.
- (92) Schwarz, H. On the spin-forbiddance of gas-phase ion–molecule reactions: a fruitful intersection of experimental and computational studies. *Int. J. Mass Spectrom.* **2004**, *237*, 75–105.
- (93) Harvey, J. N.; Poli, R.; Smith, K. M. Understanding the reactivity of transition metal complexes involving multiple spin states. *Coord. Chem. Rev.* **2003**, *238–239*, 347–361.
- (94) Shaik, S.; Hirao, H.; Kumar, D. Reactivity of High-Valent Iron–Oxo Species in Enzymes and Synthetic Reagents: A Tale of Many States. *Acc. Chem. Res.* **2007**, *40*, 532–542.

- (95) Schröder, D.; Schwarz, H. Gas-phase activation of methane by ligated transition-metal cations. *Proc. Natl. Acad. Sci. U. S. A.* **2008**, *105*, 18114–18119.
- (96) Chiavarino, B.; Cipollini, R.; Crestoni, M. E.; Fornarini, S.; Lanucara, F.; Lapi, A. Probing the Compound I-like Reactivity of a Bare High-Valent Oxo Iron Porphyrin Complex: The Oxidation of Tertiary Amines. *J. Am. Chem. Soc.* **2008**, *130*, 3208–3217.
- (97) Sainna, M. A.; Kumar, S.; Kumar, D.; Fornarini, S.; Crestoni, M. E.; de Visser, S. P. A comprehensive test set of epoxidation rate constants for iron(IV)–oxo porphyrin cation radical complexes. *Chem. Sci.* **2015**, *6*, 1516–1529.
- (98) Donald, W. A.; McKenzie, C. J.; O'Hair, R. A. J. C–H Bond Activation of Methanol and Ethanol by a High-Spin Fe^{IV}O Biomimetic Complex. *Angew. Chem. Int. Ed.* **2011**, *50*, 8379–8383.
- (99) Andris, E.; Navrátil, R.; Jašík, J.; Sabenya, G.; Costas, M.; Srnec, M.; Roithová, J. Detection of Indistinct Fe–N Stretching Bands in Iron(V) Nitrides by Photodissociation Spectroscopy. *Chem. Eur. J.* **2018**, *24*, 5078–5081.
- (100) Schröder, D.; Schwarz, H.; Aliaga-Alcalde, N.; Neese, F. Fragmentation of the (Cyclam-acetato)iron Azide Cation in the Gas Phase. *Eur. J. Inorg. Chem.* **2007**, 816–821.
- (101) Schlangen, M.; Neugebauer, J.; Reiher, M.; Schöder, D.; Pitarich López, J.; Haryono, M.; Heinemann, F. W.; Grohmann, A.; Schwarz, H. Gas-Phase C-H and N-H Bond Activation by a High Valent Nitrido-Iron Dication and (NH)-Transfer to Activated Olefins. *J. Am. Chem. Soc.* **2008**, *130*, 4287–4294.
- (102) Mas-Ballesté, R.; McDonald, A. R.; Reed, D.; Usharani, D.; Schyman, P.; Milko, P.; Shaik, S.; Que, L., Jr. Intramolecular gas-phase reactions of synthetic nonheme oxoiron(IV) ions: proximity and spin-state reactivity rules. *Chem. Eur. J.* **2012**, *18*, 11747–11760.
- (103) Cooks, R. G.; Ouyang, Z.; Takats, Z.; Wiseman, J. M. Ambient Mass Spectrometry. *Science* **2006**, *311*, 1566–1570.
- (104) Xu, S.; Veach, J. J.; Oloo, W. N.; Peters, K. C.; Wang, J.; Perry, R. H.; Que, L., Jr. Detection of a Transient Fe^V(O)(OH) Species Involved in Olefin Oxidation by a Bio-Inspired Non-Haem Iron Catalyst. *Chem. Commun.* **2018**, *54*, 8701–8704.
- (105) Fu, E. W.; Dunbar, R. C. Photodissociation Spectroscopy and Structural Rearrangements in Ions of Cyclooctatetraene, Styrene, and Related Molecules. *J. Am. Chem. Soc.* **1978**, *100*, 2283–2288.
- (106) Duncan, M. A. Infrared spectroscopy to probe structure and dynamics in metal ion–molecule complexes. *Int. Rev. Phys. Chem.* **2003**, *22*, 407–435.
- (107) Baer, T.; Dunbar, R. C. Ion Spectroscopy: Where Did It Come From; Where Is It Now; and Where Is It Going? *J. Am. Soc. Mass Spectrom.* **2010**, *21*, 681–693.
- (108) Duncan, M. A. Frontiers in the Spectroscopy of Mass-Selected Molecular Ions. *Int. J. Mass Spectrom.* **2000**, *200*, 545–569.
- (109) MacAleese, L.; Maître, P. Infrared spectroscopy of organometallic ions in the gas phase: from model to real world complexes. *Mass Spectrom Rev.* **2007**, *26*, 583–605.
- (110) Roithová, J. Characterization of reaction intermediates by ion spectroscopy. *Chem Soc Rev.* **2012**, *41*, 547–559.
- (111) Jašíková, L.; Roithová, J. Infrared Multiphoton Dissociation Spectroscopy with Free-Electron Lasers: On the Road from Small Molecules to Biomolecules. *Chem. Eur. J.* **2018**, *24*, 3374–3390.
- (112) Schlemmer, S. High-Resolution Laboratory Terahertz Spectroscopy and Applications to Astrophysics. In *Frontiers and Advances in Molecular Spectroscopy*; Laane, J., Ed.; Elsevier: Amsterdam, 2018; pp 471–525.
- (113) Douberly, G. E.; Walters, R. S.; Cui, J.; Jordan, K. D.; Duncan, M. A. Infrared Spectroscopy of Small Protonated Water Clusters, H⁺(H₂O)_n (n = 2–5): Isomers, Argon Tagging, and Deuteration. *J. Phys. Chem. A* **2010**, *114*, 4570–4579.

- (114) Rizzo, T. R.; Boyarkin, O. V. Cryogenic Methods for the Spectroscopy of Large, Biomolecular Ions. *Top. Curr. Chem.* **2015**, *365*, 43–97.
- (115) Heine, N.; Fagiani, M. R.; Rossi, M.; Wende, T.; Berder, G.; Blum, V.; Asmis, K. R. Isomer-Selective Detection of Hydrogen-Bond Vibrations in the Protonated Water Hexamer. *J. Am. Chem. Soc.* **2013**, *135*, 8266–8273.
- (116) Wolk, A. B.; Leavitt, C. M.; Garand, E.; Johnson, M. A. Cryogenic Ion Chemistry and Spectroscopy. *Acc. Chem. Res.* **2014**, *47*, 202–210.
- (117) Garand, E. Spectroscopy of Reactive Complexes and Solvated Clusters: A Bottom-Up Approach Using Cryogenic Ion Traps. *J. Phys. Chem. A* **2018**, *122*, 6479–6490.
- (118) Waller, S. E.; Yang, Y.; Castracane, E.; Racow, E. E.; Kreinbihl, J. J.; Nickson, K. A.; Johnson, C. J. The Interplay between Hydrogen Bonding and Coulombic Forces in Determining the Structure of Sulfuric Acid-Amine Clusters. *J. Phys. Chem. Lett.* **2018**, *9*, 1216–1222.
- (119) Gerlich, D. Infrared spectroscopy of cold trapped molecular ions using He-tagging. *J. Chin. Chem. Soc. (Weinheim, Ger.)* **2018**, *65*, 637–653.
- (120) Roithová, J.; Gray, A.; Andris, E.; Jašík, J.; Gerlich, D. Helium Tagging Infrared Photodissociation Spectroscopy of Reactive Ions. *Acc. Chem. Res.* **2016**, *49*, 223–230.
- (121) Schulz, J.; Jašík, J.; Gray, A.; Roithová, J. Formation of Oxazoles from Elusive Gold(I) α -Oxocarbenes: A Mechanistic Study. *Chem. Eur. J.* **2016**, *22*, 9827–9834.
- (122) Menges, F. S.; Craig, S. M.; Tötsch, N.; Bloomfield, A.; Ghosh, S.; Krüger, H.-J.; Johnson, M. A. Capture of CO₂ by a Cationic Nickel(I) Complex in the Gas Phase and Characterization of the Bound, Activated CO₂ Molecule by Cryogenic Ion Vibrational Predissociation Spectroscopy. *Angew. Chem. Int. Ed.* **2016**, *55*, 1282–1285.
- (123) Duffy, E. M.; Marsh, B. M.; Voss, J. M.; Garand, E. Characterization of the Oxygen Binding Motif in a Ruthenium Water Oxidation Catalyst by Vibrational Spectroscopy. *Angew. Chem. Int. Ed.* **2016**, *55*, 4079–4082.
- (124) Gray, H. B.; Winkler, J. R. Living with Oxygen. *Acc. Chem. Res.* **2018**, *51*, 1850–1857.
- (125) Holm, R. H. Metal-Centered Oxygen Atom Transfer Reactions. *Chem. Rev.* **1987**, *87*, 1401–1449.
- (126) O'Halloran, K. P.; Zhao, C.; Ando, N. S.; Schultz, A. J.; Koetzle, T. F.; Piccoli, P. M. B.; Hedman, B.; Hodgson, K. O.; Bobyr, E.; Kirk, M. L.; Knottenbelt, S.; Depperman, E. C.; Stein, B.; Anderson, T. M.; Cao, R.; Geletii, Y. V.; Hardcastle, K. I.; Musaev, D. G.; Neiwert, W. A.; Fang, X.; Morokuma, K.; Wu, S.; Kogerler, P.; Hill, C. L. Revisiting the Polyoxometalate-Based Late-Transition-Metal-Oxo Complexes: The “Oxo Wall” Stands. *Inorg. Chem.* **2012**, *51*, 7025–7031.
- (127) Winkler, J. R.; Gray, H. B. Electronic Structures of Oxo-Metal Ions. *Struct. Bond. (Berlin)* **2012**, *142*, 17–28.
- (128) Ray, K.; Heims, F.; Pfaff, F. F. Terminal Oxo and Imido Transition-Metal Complexes of Groups 9–11. *Eur. J. Inorg. Chem.* **2013**, 3784–3807.
- (129) Wang, B.; Lee, Y.-M.; Tcho, W.-Y.; Tussupbayev, S.; Kim, S.-T.; Kim, Y.; Seo, M. S.; Cho, K.-B.; Dede, Y.; Keegan, B. C.; Ogura, T.; Kim, S. H.; Ohta, T.; Baik, M.-H.; Ray, K.; Shearer, J.; Nam, W. Synthesis and reactivity of a mononuclear non-haem cobalt(IV)-oxo complex. *Nat. Commun.* **2017**, *8*, 14839.
- (130) Spaltenstein, E. Conry, R. R.; Critchlow, S. C.; Mayer, J. M. Synthesis, Characterization, and Reactivity of a Formally Rhenium(I) Terminal Oxo Complex, NaRe(O)(RC≡CR)₂. *J. Am. Chem. Soc.* **1989**, *111*, 8741–8742.
- (131) Poverenov, E.; Efremenko, I.; Frenkel, A. I.; Ben-David, Y.; Shimon, L. J. W.; Leitun, G.; Konstantinovski, L.; Martin, J. M. L.; Milstein, D. Evidence for a terminal Pt(IV)-oxo complex exhibiting diverse reactivity. *Nature* **2008**, *455*, 1093–1096.

- (132) Goetz, M. K.; Hill, E. A.; Filatov, A. S.; Anderson J. S Isolation of a Terminal Co(III)-Oxo Complex. *J. Am. Chem. Soc.* **2018**, *140*, 13176–13180;
- (133) Mayer, J. M. PROTON-COUPLED ELECTRON TRANSFER: A Reaction Chemist's View. *Annu. Rev. Phys. Chem.* **2004**, *55*, 363–390.
- (134) Stone, K. L.; Borovik, A. S. Lessons from nature: unraveling biological C–H bond activation. *Curr. Opin. Chem. Biol.* **2009**, *13*, 114–118.
- (135) Bím, D.; Maldonado-Domínguez, M.; Rulišek, L.; Srnec, M. Beyond the classical thermodynamic contributions to hydrogen atom abstraction reactivity. *Proc. Natl. Acad. Sci. U. S. A.* **2018**, *115*, E10287–E10294.
- (136) Fukuzumi, S. Electron-transfer properties of high-valent metal-oxo complexes. *Coord. Chem. Rev.* **2013**, *257*, 1564–1575.
- (137) Sastri, C. V.; Lee, J.; Oh, K.; Lee, Y. J.; Lee, J.; Jackson, T. A.; Ray, K.; Hirao, H.; Shin, W.; Halfen, J. A.; Kim, J.; Que, L., Jr.; Shaik, S.; Nam, W. Axial ligand tuning of a nonheme iron(IV)–oxo unit for hydrogen atom abstraction. *Proc. Natl. Acad. Sci. U. S. A.* **2007**, *104*, 19181–19186.
- (138) Wang, D.; Ray, K.; Collins, M. J.; Farquhar, E. R.; Frisch, J. R.; Gomez, L.; Jackson, T. A.; Kerscher, M.; Waleska, A.; Comba, P.; Costas, M.; Que, L., Jr. Nonheme oxoiron(IV) complexes of pentadentate N5 ligands: spectroscopy, electrochemistry, and oxidative reactivity. *Chem. Sci.* **2013**, *4*, 282–291.
- (139) Lee, Y.-M.; Kotani, H.; Suenobu, T.; Nam, W.; Fukuzumi, S. Fundamental Electron-Transfer Properties of Non-heme Oxoiron(IV) Complexes. *J. Am. Chem. Soc.* **2008**, *130*, 434–435.
- (140) Nam, W.; Lee, Y.-M.; Fukuzumi, S. Tuning Reactivity and Mechanism in Oxidation Reactions by Mononuclear Nonheme Iron(IV)-Oxo Complexes. *Acc. Chem. Res.* **2014**, *47*, 1146–1154.
- (141) Nehru, K.; Seo, M. S.; Kim, J.; Nam, W. Oxidative N-Dealkylation Reactions by Oxoiron(IV) Complexes of Nonheme and Heme Ligands. *Inorg. Chem.* **2007**, *46*, 293–298.
- (142) de Visser, S. P.; Oh, K.; Han, A.-R.; Nam, W. Combined Experimental and Theoretical Study on Aromatic Hydroxylation by Mononuclear Nonheme Iron(IV)–Oxo Complexes. *Inorg. Chem.* **2007**, *46*, 4632–4641.
- (143) Morimoto, Y.; Park, J.; Suenobu, T.; Lee, Y.-M.; Nam, W.; Fukuzumi, S. Mechanistic Borderline of One-Step Hydrogen Atom Transfer versus Stepwise Sc³⁺-Coupled Electron Transfer from Benzyl Alcohol Derivatives to a Non-Heme Iron(IV)-Oxo Complex. *Inorg. Chem.* **2012**, *51*, 10025–10036.
- (144) Warren, J. J.; Tronic, T. A.; Mayer, J. M. The Thermochemistry of Proton-Coupled Electron Transfer Reagents and its Implications. *Chem. Rev.* **2010**, *110*, 6961–7001.
- (145) Brandsma, L.; van Sodingen, J.; Andringa, H. A Procedure for the Preparation of Pure 1,4-Cyclohexadiene from Benzene. *Synth. Commun.* **1990**, *20*, 2165–2168.
- (146) Zhang, J.; Grills, D. C.; Huang, K.-W.; Fujita, E.; Bullock, R. M. Carbon-to-Metal Hydrogen Atom Transfer: Direct Observation Using Time-Resolved Infrared Spectroscopy. *J. Am. Chem. Soc.* **2005**, *127*, 15684–15685.
- (147) Goldsmith, C. R.; Jonas, R. T.; Stack, T. D. P. C–H Bond Activation by a Ferric Methoxide Complex: Modeling the Rate-Determining Step in the Mechanism of Lipoxygenase. *J. Am. Chem. Soc.* **2002**, *124*, 83–96.
- (148) Bunton, C. A.; Halevi, E. A.; Llewellyn, D. R. Oxygen Exchange between Nitric Acid and Water. Part I. *J. Chem. Soc.* **1952**, 4913–4916.
- (149) Kaneko, M.; Poulson, S. R. The rate of oxygen isotope exchange between nitrate and water. *Geochim. Cosmochim. Acta* **2013**, *118*, 148–156.
- (150) Fenn, J. B. Electrospray wings for molecular elephants (Nobel lecture). *Angew. Chem. Int. Ed.* **2003**, *42*, 3871–3894.
- (151) Ducháčková, L.; Roithová, J. The Interaction of Zinc(II) and Hydroxamic Acids and a Metal-Triggered Lossen Rearrangement. *Chem. Eur. J.* **2009**, *15*, 13399–13405.

- (152) Jašíková, L.; Roithová, J. Interaction of the Gold(I) Cation $\text{Au}(\text{PMe}_3)^+$ with Unsaturated Hydrocarbons. *Organometallics* **2012**, *31*, 1935–1942.
- (153) Cole, R. B. Some tenets pertaining to electrospray ionization mass spectrometry. *J. Mass Spectrom.* **2000**, *35*, 763–772.
- (154) Company, A.; Prat, I.; Frisch, J. R.; Ballesté, R. M.; Güell, M.; Juhász, G.; Ribas, X.; Münck, E.; Luis, J. M.; Que, L., Jr.; Costas, M. Modeling the cis-Oxo-Labile Binding Site Motif of Non-Heme Iron Oxygenases: Water Exchange and Oxidation Reactivity of a Non-Heme Iron(IV)-Oxo Compound Bearing a Tripodal Tetradentate Ligand. *Chem. Eur. J.* **2011**, *17*, 1622–1634.
- (155) Bonnet, S.; Li, J.; Siegler, M. A.; von Chrzanowski, L. S.; Spek, A. L.; van Koten, G.; Klein Gebbink, R. J. M. Synthesis and Resolution of Planar-Chiral Ruthenium-Palladium Complexes with ECE' Pincer Ligands. *Chem. Eur. J.* **2009**, *15*, 3340–3343.
- (156) Schröder, D.; Roithová, J.; Schwarz, H. Electrospray ionization as a convenient new method for the generation of catalytically active iron-oxide ions in the gas phase. *Int. J. Mass Spectrom.* **2006**, *254*, 197–201.
- (157) Anbar, M.; Guttman, S. The Catalytic Effect of Chloride Ions on the Isotopic Oxygen Exchange of Nitric and Bromic Acids with Water. *J. Am. Chem. Soc.* **1961**, *83*, 4741–4745.
- (158) Erwin, K. M.; Armentrout, P. B. Translational energy dependence of $\text{Ar}^+ + \text{XY} \rightarrow \text{ArX}^+ + \text{Y}$ ($\text{XY} = \text{H}_2, \text{D}_2, \text{HD}$) from thermal to 30 eV c.m. *J. Chem. Phys.* **1985**, *83*, 166–189.
- (159) Schröder, D.; Schwarz, H.; Clemmer, D. E.; Chen, Y.; Armentrout, P. B.; Baranov, V. I.; Böhme, D. K. Activation of hydrogen and methane by thermalized FeO^+ in the gas phase as studied by multiple mass spectrometric techniques. *Int. J. Mass. Spectrom. Ion Processes* **1997**, *161*, 175–191.
- (160) Jašík, J.; Gerlich, D.; Roithová, J. Probing Isomers of the Benzene Dication in a Low-Temperature Trap. *J. Am. Chem. Soc.* **2014**, *136*, 2960–2962.
- (161) Jašík, J.; Gerlich, D.; Roithová, J. Probing Isomers of the Benzene Dication in a Low-Temperature Trap. *J. Am. Chem. Soc.* **2014**, *136*, 2960–2962.
- (162) Jašík, J.; Navrátil, R.; Němec, I.; Roithová, J. Infrared and Visible Photodissociation Spectra of Rhodamine Ions at 3 K in the Gas Phase. *J. Phys. Chem. A* **2015**, *119*, 12648–12655.
- (163) Jašík, J.; Žabka, J.; Roithová, J.; Gerlich, D. Infrared spectroscopy of trapped molecular dications below 4 K. *Int. J. Mass Spectrom.* **2013**, *354–355*, 204–210.
- (164) Jašík, J.; Gerlich, D.; Roithová, J. Two-Color Infrared Predissociation Spectroscopy of $\text{C}_6\text{H}_6^{2+}$ Isomers Using Helium Tagging. *J. Phys. Chem. A* **2015**, *119*, 2532–2542.
- (165) Rothman, L. S.; Gordon, I. E.; Babikov, Y.; Barbe, A.; Benner Chris, D.; Bernath, P. F.; Birk, M.; Bizzocchi, L.; Boudon, V.; Brown, L. R.; Campargue, A.; Chance, K.; Cohen, E.A.; Coudert, L. H.; Devi, V. M.; Drouin, B. J.; Fayt, A.; Flaud, J.-M.; Gamache, R. R.; Harrison, J. J.; Hartmann, J.-M.; Hill, C.; Hodges, J. T.; Jacquemart, D.; Jolly, A.; Lamouroux, J.; Le Roy, R. J.; Li, G.; Long, D. A.; Lyulin, O.M.; Mackie, C. J.; Massie, S. T.; Mikhailenko, S.; Müller, H. S. P.; Naumenko, O. V.; Nikitin, A. V.; Orphal, J.; Perevalov, V.; Perrin, A.; Polovtseva, E. R.; Richard, C.; Smith, M. A. H.; Starikova, E.; Sung, K.; Tashkun, S.; Tennyson, J.; Toon, G. C.; Tyuterev, V. G.; Wagner, G. The HITRAN 2012 Molecular Spectroscopic Database. *J. Quant. Spectrosc. Radiat. Transfer* **2013**, *130*, 4–50.
- (166) Savitzky, A.; Golay, M. J. E. Smoothing and Differentiation of Data by Simplified Least Squares Procedures. *Anal. Chem.* **1964**, *36*, 1627–1639.
- (167) Frisch, M. J.; Trucks, G. W.; Schlegel, H. B.; Scuseria, G. E.; Robb, M. A.; Cheeseman, J. R.; Scalmani, G.; Barone, V.; Mennucci, B.; Petersson, G. A.; Nakatsuji, H.; Caricato, M.; Li, X.; Hratchian, H. P.; Izmaylov, A. F.; Bloino, J.; Zheng, G.; Sonnenberg, J. L.; Hada, M.; Ehara, M.; Toyota, K.; Fukuda, R.; Hasegawa, J.; Ishida, M.; Nakajima, T.; Honda, Y.; Kitao, O.; Nakai, H.; Vreven, T.; Montgomery, J. A., Jr.; Peralta, J. E.; Ogliaro, F.; Bearpark, M.; Heyd, J. J.; Brothers, E.; Kudin, K. N.; Staroverov, V. N.; Keith, T.; Kobayashi, R.; Normand, J.; Raghavachari, K.; Rendell, A.; Burant, J. C.; Iyengar, S. S.;

- Tomasi, J.; Cossi, M.; Rega, N.; Millam, J. M.; Klene, M.; Knox, J. E.; Cross, J. B.; Bakken, V.; Adamo, C.; Jaramillo, J.; Gomperts, R.; Stratmann, R. E.; Yazyev, O.; Austin, A. J.; Cammi, R.; Pomelli, C.; Ochterski, J. W.; Martin, R. L.; Morokuma, K.; Zakrzewski, V. G.; Voth, G. A.; Salvador, P.; Dannenberg, J. J.; Dapprich, S.; Daniels, A. D.; Farkas, O.; Foresman, J. B.; Ortiz, J. V.; Cioslowski, J.; Fox, D. J. *Gaussian 09*, revision D.01; Gaussian, Inc.: Wallingford, CT, 2013.
- (168) Zhao, Y.; Truhlar, D. G. The M06 suite of density functionals for main group thermochemistry, thermochemical kinetics, noncovalent interactions, excited states, and transition elements: two new functionals and systematic testing of four M06-class functionals and 12 other functionals. *Theor. Chem. Acc.* **2008**, *120*, 215–241.
- (169) Perdew, J. P.; Burke, K.; Ernzerhof, M. Generalized Gradient Approximation Made Simple. *Phys. Rev. Lett.* **1996**, *77*, 3865–3868 ; Correction: *Phys. Rev. Lett.* **1997**, *78*, 1396.
- (170) Handy, N.C.; Cohen, A. J. Left-right correlation energy. *Mol. Phys.* **2001**, *99*, 403–412.
- (171) Hoe, W.-M.; Cohen, A.; Handy, N. C. Assessment of a new local exchange functional OPTX. *Chem. Phys. Lett.* **2001**, *341*, 319–328.
- (172) Miehlich, B.; Savin, A.; Stoll, H.; Preuss, H. Results obtained with the correlation energy density functionals of Becke and Lee, Yang and Parr. *Chem. Phys. Lett.* **1989**, *157*, 200–206.
- (173) Lee, C.; Yang, W.; Parr, R. G. Development of the Colle-Salvetti correlation-energy formula into a functional of the electron density. *Phys. Rev. B* **1988**, *37*, 785–789.
- (174) Vosko, S. H.; Wilk, L.; Nusair, M. Accurate spin-dependent electron liquid correlation energies for local spin density calculations: A critical analysis. *Can. J. Phys.* **1980**, *58*, 1200–1211.
- (175) Becke, A. D. Density-functional thermochemistry. III. The role of exact exchange. *J. Chem. Phys.* **1993**, *98*, 5648–5652.
- (176) Stephens, P. J.; Devlin, F. J.; Chabalowski, C. F.; Frisch, M. J. *Ab Initio* Calculation of Vibrational Absorption and Circular Dichroism Spectra Using Density Functional Force Fields. *J. Phys. Chem.* **1994**, *98*, 11623–11627.
- (177) Zhao, Y.; Truhlar, D. G. A new local density functional for main-group thermochemistry, transition metal bonding, thermochemical kinetics, and noncovalent interactions. *J. Chem. Phys.* **2006**, *125*, 194101.
- (178) Grimme, S.; Ehrlich, S.; Goerigk, L. Effect of the damping function in dispersion corrected density functional theory. *J. Comp. Chem.* **2011**, *32*, 1456–1465.
- (179) Grimme, S.; Antony, J.; Ehrlich, S.; Krieg, H. A consistent and accurate ab initio parameterization of density functional dispersion correction (DFT-D) for the 94 elements H-Pu. *J. Chem. Phys.* **2010**, *132*, 154104.
- (180) Ditchfield, R.; Hehre, W. J.; Pople, J. A. Self-Consistent Molecular Orbital Methods. 9. Extended Gaussian-type basis for molecular-orbital studies of organic molecules. *J. Chem. Phys.* **1971**, *54*, 724–728.
- (181) Ditchfield, R.; Hehre, W. J.; Pople, J. A. Self—Consistent Molecular Orbital Methods. XII. Further Extensions of Gaussian—Type Basis Sets for Use in Molecular Orbital Studies of Organic Molecules. *J. Chem. Phys.* **1972**, *56*, 2257–2261.
- (182) Hariharan, P. C.; Pople, J. A. The Influence of Polarization Functions on Molecular Orbital Hydrogenation Energies. *Theor. Chim. Acta* **1973**, *28*, 213–222.
- (183) Hariharan, P. C.; Pople, J. A. Accuracy of AH_n equilibrium geometries by single determinant molecular orbital theory. *Mol. Phys.* **1974**, *27*, 209–214.
- (184) Gordon, M. S. The isomers of silacyclopropane. *Chem. Phys. Lett.* **1980**, *76*, 163–168.
- (185) Francl, M. M.; Pietro, W. J.; Hehre, W. J.; Binkley, J. S.; DeFrees, D. J.; Pople, J. A.; Gordon, M. S. Self-consistent molecular orbital methods. XXIII. A polarization-type basis set for second-row elements. *J. Chem. Phys.* **1982**, *77*, 3654–3665.

- (186) Binning, R. C., Jr.; Curtiss, L. A. Compact contracted basis sets for third-row atoms: Ga–Kr. *J. Comp. Chem.* **1990**, *11*, 1206–1216.
- (187) Blaudeau, J.-P.; McGrath, M. P.; Curtiss, L. A.; Radom, L. Extension of Gaussian-2 (G2) theory to molecules containing third-row atoms K and Ca. *J. Chem. Phys.* **1997**, *107*, 5016–5021.
- (188) Rassolov, V. A.; Pople, J. A.; Ratner, M. A.; Windus, T. L. 6-31G* basis set for atoms K through Zn. *J. Chem. Phys.* **1998**, *109*, 1223–1229.
- (189) Rassolov, V. A.; Ratner, M. A.; Pople, J. A.; Redfern, P. C.; Curtiss, L. A. 6-31G* basis set for third-row atoms. *J. Comp. Chem.* **2001**, *22*, 976–984.
- (190) Frisch, M. J.; Pople, J. A.; Binkley, J. S. Self-consistent molecular orbital methods 25. Supplementary functions for Gaussian basis sets. *J. Chem. Phys.* **1984**, *80*, 3265–3269.
- (191) McLean, A. D.; Chandler, G. S. Contracted Gaussian basis sets for molecular calculations. I. Second row atoms, $Z=11-18$. *J. Chem. Phys.* **1980**, *72*, 5639–5648.
- (192) Raghavachari, K.; Binkley, J. S.; Seeger, R.; Pople, J. A. Self-consistent molecular orbital methods. XX. A basis set for correlated wave functions. *J. Chem. Phys.* **1980**, *72*, 650–654.
- (193) Wachters, A. J. H. Gaussian Basis Set for Molecular Wavefunctions Containing Third-Row Atoms. *J. Chem. Phys.* **1970**, *52*, 1033–1036.
- (194) Hay, P. J. Gaussian basis sets for molecular calculations – representation of 3D orbitals in transition-metal atoms. *J. Chem. Phys.* **1977**, *66*, 4377–4384.
- (195) Raghavachari, K.; Trucks, G. W. Highly correlated systems: Excitation energies of first row transition metals Sc–Cu. *J. Chem. Phys.* **1989**, *91*, 1062–1065.
- (196) Schäfer, A.; Horn, H.; Ahlrichs, R. Fully optimized contracted Gaussian basis sets for atoms Li to Kr. *J. Chem. Phys.* **1992**, *97*, 2571–2577.
- (197) Schäfer, A.; Huber, C.; Ahlrichs, R. Fully optimized contracted Gaussian basis sets of triple zeta valence quality for atoms Li to Kr. *J. Chem. Phys.* **1994**, *100*, 5829–5835.
- (198) Weigend, F.; Ahlrichs, R. Balanced basis sets of split valence, triple zeta valence and quadruple zeta valence quality for H to Rn: Design and assessment of accuracy. *Phys. Chem. Chem. Phys.* **2005**, *7*, 3297–3305.
- (199) Jensen, F. Polarization consistent basis sets: Principles. *J. Chem. Phys.* **2001**, *115*, 9113–9125; Correction: *J. Chem. Phys.* **2002**, *116*, 3502.
- (200) Jensen, F. Polarization consistent basis sets. II. Estimating the Kohn–Sham basis set limit. *J. Chem. Phys.* **2002**, *116*, 7372–7379.
- (201) Jensen, F.; Helgaker, T. Polarization consistent basis sets. V. The elements Si–Cl. *J. Chem. Phys.* **2004**, *121*, 3463–3470.
- (202) Boese, A. D.; Martin, J. M. L. Anharmonic force fields of perchloric acid, HClO₄, and perchloric anhydride, Cl₂O₇. An extreme case of inner polarization. *J. Mol. Struct.* **2006**, *780–781*, 310–316.
- (203) Yoshida, H.; Takeda, K.; Okamura, J.; Ehara, A.; Matsuura, H. A New Approach to Vibrational Analysis of Large Molecules by Density Functional Theory: Wavenumber-Linear Scaling Method. *J. Phys. Chem. A* **2002**, *106*, 3580–3586.
- (204) Roos, B. O.; Taylor, P. R.; Siegbahn, P. E. M. A complete active space SCF method (CASSCF) using a density matrix formulated super-CI approach. *Chem. Phys.* **1980**, *48*, 157–173.
- (205) Siegbahn, P. E. M.; Almlöf, J.; Heiberg, A.; Roos, B. O. The Complete Active Space SCF (CASSCF) Method in a Newton-Raphson Formulation with Application to the HNO molecule. *J. Chem. Phys.* **1981**, *74*, 2384–2396.
- (206) Andersson, K.; Malmqvist, P.-Å.; Roos, B. O.; Sadlej, A. J.; Wolinski, K. Second-order perturbation theory with a CASSCF reference function. *J. Phys. Chem.* **1990**, *94*, 5483–5488.
- (207) Andersson, K.; Malmqvist, P.-Å.; Roos, B. O. Second-order perturbation theory with a complete active space self-consistent field reference function. *J. Chem. Phys.* **1992**, *96*, 1218–1226.

- (208) Andersson, K. Different forms of the zeroth-order Hamiltonian in second-order perturbation theory with a complete active space self-consistent field reference function. *Theor. Chim. Acta* **1995**, *91*, 31–46.
- (209) Finley, J.; Malmqvist, P.-Å.; Roos, B. O.; Serrano-Andrés, L. The multi-state CASPT2 method. *Chem. Phys. Lett.* **1998**, *288*, 299–306.
- (210) Aquilante, F.; Pedersen, T. B.; Lindh, R.; Roos, B. O.; Sánchez de Merás, A.; Koch, H. Accurate *ab initio* density fitting for multiconfigurational self-consistent field methods. *J. Chem. Phys.* **2008**, *129*, 024113.
- (211) Douglas, M.; Kroll, N. M. Quantum electrodynamical corrections to the fine structure of helium. *Ann. Phys. (N.Y.)* **1974**, *82*, 89–155.
- (212) Hess, B. A. Relativistic electronic-structure calculations employing a two-component no-pair formalism with external-field projection operators. *Phys. Rev. A* **1986**, *33*, 3742–3748.
- (213) Jansen, G.; Hess, B. A. Revision of the Douglas-Kroll transformation. *Phys. Rev. A* **1989**, *39*, 6016–6017.
- (214) Roos, B. O.; Andersson, K. Multiconfigurational perturbation theory with level shift — the Cr₂ potential revisited. *Chem. Phys. Lett.* **1995**, *245*, 215–243.
- (215) Forsberg, N.; Malmqvist, P.-Å. Multiconfiguration perturbation theory with imaginary level shift. *Chem. Phys. Lett.* **1997**, *274*, 196–204.
- (216) Seo, M. S.; In, J.-H.; Kim, S. O.; Oh, N. Y.; Hong, J.; Kim, J.; Que, L., Jr.; Nam, W. Direct Evidence for Oxygen-Atom Exchange between Nonheme Oxoiron(IV) Complexes and Isotopically Labeled Water. *Angew. Chem. Int. Ed.* **2004**, *43*, 2417–2420.
- (217) Puri, M.; Company, A.; Sabenya, G.; Costas, M.; Que, L., Jr. Oxygen Atom Exchange between H₂O and Non-Heme Oxoiron(IV) Complexes: Ligand Dependence and Mechanism. *Inorg. Chem.* **2016**, *55*, 5818–5827.
- (218) Škríba, A.; Jašík, J.; Andris, E.; Roithová, J. Interaction of Ruthenium(II) with Terminal Alkynes: Benchmarking DFT Methods with Spectroscopic Data. *Organometallics* **2016**, *35*, 990–994.
- (219) Fridgen, T. D. Infrared consequence spectroscopy of gaseous protonated and metal ion cationized complexes. *Mass Spectrom. Rev.* **2009**, *28*, 586–607.
- (220) Nosenko, Y.; Menges, F.; Riehn, C.; Niedner-Schatteburg, G. Investigation by two-color IR dissociation spectroscopy of Hoogsteen-type binding in a metalated nucleobase pair mimic. *Phys. Chem. Chem. Phys.* **2013**, *15*, 8171–8178.
- (221) Ingram, J.; Wolk, A. B.; Flender, C.; Zhang, J.; Johnson, C. J.; Hintermair, U.; Crabtree, R. H.; Johnson, M. A.; Zare, R. N. Modes of activation of organometallic iridium complexes for catalytic water and C–H oxidation. *Inorg. Chem.* **2014**, *53*, 423–433.
- (222) Jašíková, L.; Hanikýřová, E.; Schröder, D.; Roithová, J. Aromatic C–H bond activation revealed by infrared multiphoton dissociation spectroscopy. *J. Mass Spectrom.* **2012**, *47*, 460–465.
- (223) Jašíková, L.; Hanikýřová, E.; Škríba, A.; Jašík, J.; Roithová, J. Metal-assisted Lossen Rearrangement. *J. Org. Chem.* **2012**, *77*, 2829–2936.
- (224) Roithová, J.; Milko, P. Naphthol Coupling Monitored by Infrared Spectroscopy in the Gas Phase. *J. Am. Chem. Soc.* **2010**, *132*, 281–288.
- (225) Chiavarino, B.; Crestoni, M. E.; Fornarini, S.; Lanucara, F.; Lemaire, J.; Maitre, P. Meisenheimer Complexes Positively Characterized as Stable Intermediates in the Gas Phase. *Angew. Chem. Int. Ed.* **2007**, *46*, 1995–1998.
- (226) Nielsen, A.; Larsen, F. B.; Bond, A. D.; McKenzie, C. J. Regiospecific Ligand Oxygenation in Iron Complexes of a Carboxylate-Containing Ligand Mediated by a Proposed Fe^V-Oxo Species. *Angew. Chem. Int. Ed.* **2006**, *45*, 1602–1606.
- (227) Reed, A. E.; Weinstock, R. B.; Weinhold, F. Natural population analysis. *J. Chem. Phys.* **1985**, *83*, 735–746.

- (228) Hong, S.; Lee, Y.-M.; Cho, K.-B.; Sundaravel, K.; Cho, J.; Kim, M. J.; Shin, W.; Nam, W. Ligand Topology Effect on the Reactivity of a Mononuclear Nonheme Iron(IV)-Oxo Complex in Oxygenation Reactions. *J. Am. Chem. Soc.* **2011**, *133*, 11876–11879.
- (229) Roithová, J.; Schröder, D. Bimolecular reactions of molecular dications: reactivity paradigms and bond-forming processes. *Phys. Chem. Chem. Phys.* **2007**, *9*, 2341–2349.
- (230) Wang, D.; Ray, K.; Collins, M. J.; Farquhar, E. R.; Frisch, J. R.; Gomez, L.; Jackson, T.; Kerscher, M.; Waleska, A.; Comba, P.; Costas, M.; Que, L., Jr. Nonheme oxoiron(IV) complexes of pentadentate N5 ligands: spectroscopy, electrochemistry, and oxidative reactivity. *Chem. Sci.* **2013**, *4*, 282–291.
- (231) de Visser, S. P.; Rohde, J.-U.; Lee, Y.-M.; Cho, J.; Nam, W. Intrinsic properties and reactivities of mononuclear nonheme iron–oxygen complexes bearing the tetramethylcyclam ligand. *Coord. Chem. Rev.* **2013**, *257*, 381–393.
- (232) Armentrout, P. B. Kinetic energy dependence of ion–molecule reactions: guided ion beams and threshold measurements. *Int. J. Mass Spectrom.* **2000**, *200*, 219–241.
- (233) Prakash, J.; Rohde, G. T.; Meier, K. K.; Münck, E.; Que, L., Jr. Upside Down! Crystallographic and Spectroscopic Characterization of an $[\text{Fe}^{\text{IV}}(\text{O}_{\text{syn}})(\text{TMC})]^{2+}$ Complex. *Inorg. Chem.* **2015**, *54*, 11055–11057.
- (234) McDonald, A. R.; Bukowski, M. R.; Farquhar, E. R.; Jackson, T. A.; Koehntop, K. D.; Seo, M. S.; De Hont, R. F.; Stubna, A.; Halfen, J. A.; Münck, E. Sulfur versus Iron Oxidation in an Iron–Thiolate Model Complex. *J. Am. Chem. Soc.* **2010**, *132*, 17118–17129.
- (235) Fiedler, A. T.; Halfen, H. L.; Halfen, J. A.; Brunold, T. C. Synthesis, Structure Determination, and Spectroscopic/Computational Characterization of a Series of Fe(II)–Thiolate Model Complexes: Implications for Fe–S Bonding in Superoxide Reductases. *J. Am. Chem. Soc.* **2005**, *127*, 1675–1689.
- (236) Cho, J.; Jeon, S.; Wilson, S. A.; Liu, L. V.; Kang, E. A.; Braymer, J. J.; Lim, M. H.; Hedman, B.; Hodgson, K. O.; Valentine, J. S.; Solomon, E. I.; Nam, W. Structure and reactivity of a mononuclear non-haem iron(III)-peroxo complex. *Nature* **2011**, *478*, 502–505.
- (237) Fukuzumi, S.; Morimoto, Y.; Kotani, H.; Naumov, P.; Lee, Y.-M.; Nam, W. Crystal structure of a metal ion-bound oxoiron(IV) complex and implications for biological electron transfer. *Nat. Chem.* **2010**, *2*, 756–759.
- (238) Prakash, J.; Rohde, G. T.; Meier, K. K.; Münck, E.; Que, L., Jr. Spectroscopic Identification of an Fe^{III} Center, not Fe^{IV} , in the Crystalline Sc–O–Fe Adduct Derived from $[\text{Fe}^{\text{IV}}(\text{O})(\text{TMC})]^{2+}$. *J. Am. Chem. Soc.* **2015**, *137*, 3478–3481.
- (239) Budria, J. G.; Raugei, S.; Cavallo, L. Structure and Bonding in Monomeric Iron(III) Complexes with Terminal Oxo and Hydroxo Ligands. *Inorg. Chem.* **2006**, *45*, 1732–1738.
- (240) Frisch, J. R. Spectroscopic and crystallographic characterization of peroxo- and oxoiron complexes. Ph.D. Dissertation, University of Minnesota, MN, 2010.
- (241) Lacy, D. C.; Gupta, R.; Stone, K. L.; Greaves, J.; Ziller, J. W.; Hendrich, M. P.; Borovik, A. S. Formation, Structure, and EPR Detection of a High Spin Fe^{IV} -Oxo Species Derived from Either an Fe^{III} -Oxo or Fe^{III} -OH Complex. *J. Am. Chem. Soc.* **2010**, *132*, 12188–12190.
- (242) Shin, J. W.; Hammer, N. I.; Diken, E. G.; Johnson, M. A.; Walters, R. S.; Jaeger, T. D.; Duncan, M. A.; Christie, R. A.; Jordan, K. D. Infrared signature of structures associated with the $\text{H}^+(\text{H}_2\text{O})_n$ ($n = 6$ to 27) clusters. *Science* **2004**, *304*, 1137–1140.
- (243) Duffy, E. M.; Marsh, B. M.; Garand, E. Probing the Hydrogen-Bonded Water Network at the Active Site of a Water Oxidation Catalyst: $[\text{Ru}(\text{bpy})(\text{tpy})(\text{H}_2\text{O})]^{2+} \cdot (\text{H}_2\text{O})_{0-4}$. *J. Phys. Chem. A* **2015**, *119*, 6326–6332.
- (244) Sahoo, D.; Quesne, M. G.; de Visser, S. P.; Rath, S. P. Hydrogen-Bonding Interactions Trigger a Spin-Flip in Iron(III) Porphyrin Complexes. *Angew. Chem. Int. Ed.* **2015**, *127*, 4878–4882.
- (245) Dey, A.; Hocking, R. K.; Larsen, P.; Borovik, A. S.; Hodgson, K. O.; Hedman, B.; Solomon, E. I. X-ray Absorption Spectroscopy and Density Functional Theory Studies of $[(\text{H}_3\text{buea})\text{Fe}^{\text{III}}\text{X}]^n$ ($\text{X} = \text{S}^{2-}, \text{O}^{2-}, \text{OH}^-$)

-): Comparison of Bonding and Hydrogen Bonding in Oxo and Sulfido Complexes. *J. Am. Chem. Soc.* **2006**, *128*, 9825–9833.
- (246) Shimanouchi, T. Molecular Vibrational Frequencies. In *NIST Chemistry WebBook, NIST Standard Reference Database Number 69*; Linstrom, P. J., Mallard, W. G., Eds.; National Institute of Standards and Technology: Gaithersburg, MD.
- (247) O'Brien, J. T.; Williams, E. R. Coordination Numbers of Hydrated Divalent Transition Metal Ions Investigated with IRPD Spectroscopy. *J. Phys. Chem. A* **2011**, *115*, 14612–14619.
- (248) Fukuzumi, S.; Kotani, H.; Lee, Y.-M.; Nam, W. Sequential Electron-Transfer and Proton-Transfer Pathways in Hydride-Transfer Reactions from Dihyronicotinamide Adenine Dinucleotide Analogues to Non-heme Oxoiron(IV) Complexes and *p*-Chloranil. Detection of Radical Cations of NADH Analogues in Acid-Promoted Hydride-Transfer Reactions. *J. Am. Chem. Soc.* **2008**, *130*, 15134–15142.
- (249) Tsang, W. Thermodynamic and kinetic properties of the cyclohexadienyl radical. *J. Phys. Chem.* **1986**, *90*, 1152–1155.
- (250) Trujillo, M.; Alvarez, B.; Radi, R. One- and two-electron oxidation of thiols: mechanisms, kinetics and biological fates. *Free Radical Res.* **2015**, *50*, 150–171.
- (251) Weinberg, D. R.; Gagliardi, C. J.; Hull, J. F.; Fecenko Murphy, C.; Kent, C. A.; Westlake, B. C.; Paul, A.; Ess, D. H.; Granville McCafferty, D.; Meyer, T. J. Proton-Coupled Electron Transfer. *Chem. Rev.* **2012**, *112*, 4016–4093.
- (252) Usharani, D.; Lacy, D. C.; Borovik, A. S.; Shaik, S. Dichotomous Hydrogen Atom Transfer vs Proton-Coupled Electron Transfer During Activation of X–H Bonds (X = C, N, O) by Nonheme Iron–Oxo Complexes of Variable Basicity. *J. Am. Chem. Soc.* **2013**, *135*, 17090–17104.
- (253) Usharani, D.; Janardanan, D.; Li, C.; Shaik, S. A Theory for Bioinorganic Chemical Reactivity of Oxometal Complexes and Analogous Oxidants: The Exchange and Orbital-Selection Rules. *Acc. Chem. Res.* **2013**, *46*, 471–482.
- (254) Janousek, B.K.; Reed, K.J.; Brauman, J.I. Electron Photodetachment from Mercaptyl Anions (RS⁻). Electron Affinities of Mercaptyl Radicals and the S–H Bond Strength in Mercaptans. *J. Am. Chem. Soc.* **1980**, *102*, 3125–3129.